X-ray Absorption Fine Structure Study of Magnetic Systems

by
Yolande R. Bonin
B.Sc. Laurentian University, 1987
M.Sc. Dalhousie University, 1989

THESIS SUBMITTED IN PARTIAL FULFILLMENT OF
THE REQUIREMENTS FOR THE DEGREE OF
DOCTOR OF PHILOSOPHY
in the Department
of
Physics

Simon Fraser University
Burnaby, B.C., Canada
December, 1993

APPROVAL

Name: Yolande Reina Bonin
Degree: Doctor of Philosophy
Title of Thesis: X-ray Absorption Fine Structure Study of Magnetic Systems

Examining Committee:

Chairman: Dr. M. Thewalt

Dr. E.D. Crozier
Senior Supervisor)

Dr. J.F. Cochran

Dr. B. Heinrich

Dr. R.F. Frindt
University Examiner

Dr. J. Boyce
External Examiner
Xerox Palo Alto Research Center

Date: *December 17th, 1993*

PARTIAL COPYRIGHT LICENSE

I hereby grant to Simon Fraser University the right to lend my thesis, project or extended essay (the title of which is shown below) to users of the Simon Fraser University Library, and to make partial or single copies only for such users or in response to a request from the library of any other university, or educational institution, on its own behalf or for one of its users. I further agree that permission for multiple copying of this work for scholarly purposes may be granted by me or the Dean of Graduate Studies. It is understood that copying or publication of this work for financial gain shall not be allowed without my written permission.

Title of thesis/Project/Extended Essay

X-Ray Absorption Fine Structure Study of Magnetic Systems

Author: _____

(signature)

Yolande R. Bonin

(name)

Dec 22nd 1993

(date)

Abstract

Major advances in magnetic applications have resulted from engineering materials with specific magnetic properties. It is important to determine the structure of these new materials. In this thesis the local structures of two magnetic systems, $Tb_{0.3}Dy_{0.7}Fe_2$ (Terfenol-D) and Fe/Cu/Fe trilayers have been determined using extended x-ray absorption fine structure (EXAFS) spectroscopy.

Magnetostriction refers to the change in length of a magnetic material when a magnetic field is applied. Giant magnetostrictive effects have been reported for the rare-earth alloys $Tb_{1-x}Dy_xFe_2$. In $Tb_{0.3}Dy_{0.7}Fe_2$ the saturation strain, λ_s, is 1.1×10^{-3}. In the present study structural changes due to an applied magnetic field and as a function of temperature were examined by a polarization-dependent EXAFS study. All EXAFS measurements were done at two temperatures above and below the spin reorientation temperature, $T_s = 283$K, at two applied magnetic fields, $B = 0$ and $B = 5.5$kG, and at two edges the Fe K edge and the Dy L_{III} edge. To within $\pm.003$Å, no internal distortion of the unit cell was observed.

Molecular beam epitaxy (MBE) is a crystal growing technique permitting layer-by-layer growth. This technique was used to grow crystals consisting of magnetic layers separated by a non-magnetic spacer. The thickness of the magnetic spacer can change the magnetic properties of the thin film. For Fe/Cu/Fe films the exchange coupling between the Fe layers is ferromagnetic when the Cu is less than 8 monolayers thick and antiferromagnetic when it exceeds 8 monolayers(ML). The structure of the Cu was determined by glancing incidence EXAFS. Three samples were grown by MBE, one with 8ML, one with 14ML and one with 20ML of Cu, all on 8ML of Fe. The Cu was covered with 5ML of Fe capped with 10ML of Au. EXAFS measurements were done with the electric field vector parallel and perpendicular to the surface of the substrate. When Cu is only 8ML thick the structure is bcc-like with a .8% increase in

the in-plane lattice spacing and .2% increase of the out-of-plane lattice spacing with respect to bcc Fe.. For the sample with 20ML of Cu the Cu is closer to an fcc structure, the bulk structure of Cu, but has a high degree of local disorder. The nearest neighbor distance differs by .7% from fcc Cu but the coordination numbers obtained are those for a bcc structure. The 14ML is a mixture of the two structures, bcc and fcc.

Acknowledgements

Many have made contributions that made this work possible. First, I want to thank my supervisor, Professor Daryl Crozier, who always showed enthusiasm for the work and was a constant source of encouragement.

Thanks are also due to the following people for sharing their expertise in their respective fields or for lending a helping hand: the staff in the work shop who have built some of the equipment, Vern Moen who shared some of his technical expertise and did some of the sputtering for Terfenol-D, Dr. M. Parameswaran for letting me use some of his sputtering equipment, Dr. Bretislav Heinrich for patiently sharing his expertise in the MBE work, Dr. Zbigniew Celinski for teaching me the technique to prepare the substrates, Ken Myrtle for keeping the MBE equipment running, Moyra McManus for helping with some of the polishing, the sputtering of the Terfenol-D and the data collection, the staff at SSRL for providing assistance at all hours of the day, Peter Boyd, from SSRL, for building the permanent magnet, Professor Robert Ingalls, Dr. Brian Houser and Fuming Wang for assistance in the early experiments.

I would also thank the supervising committee, Dr. E.D. Crozier, Dr. J.F. Cochran and Dr. B. Heinrich for the thorough reading of this thesis.

The research was supported by grants from the Natural Sciences and Engineering Research Council, awarded to E.D. Crozier. EXAFS experiments were performed at SSRL and NSLS which are supported by the Department of Energy, USA.

Contents

List of Tables

List of Figures

1 Introduction

Modern technology permits the synthesis of various materials whose properties are tailored for specific applications. Correlating the structure of the material with the properties of interest can provide important information on the understanding of the effects sought after for various types of devices. One example is an attempt to satisfy the transducer industry by exploiting the magnetostrictive effect. Magnetostriction refers to the change in length of a magnetic material when a magnetic field is applied. Before the sixties, the largest known magnetostrictive strain was of the order of 10^{-5}. In the next two decades research with the rare earth materials demonstrated a class of elements with interesting magnetic properties. The saturation magnetostrictive strains of polycrystalline Tb and Dy at 78K are 833×10^{-6}[1] and 934×10^{-6}[2] respectively but they are paramagnetic at room temperature[3]. By alloying the rare-earths with 3d elements, materials that are highly magnetostrictive at room temperature are produced. In 1972 Clark and Belson wrote "We wish to report the discovery of the largest room temperature magnetostriction ever observed"[4]. They discovered that the saturation magnetostriction was greater than 1200×10^6 in the cubic Laves phase $TbFe_2$. Compare this value with Ni, for instance, which has $\lambda_s = 35 \times 10^{-6}$[4],[5],[6]. Because of this large magnetostriction these alloys have significant technological importance as components of transducers, delay

lines, and active positioning devices[7].

For high power transducer applications in particular, high strain at low fields is necessary. Therefore a low anisotropy is important in order to maximize domain wall mobility and easy domain rotation at low fields. But usually magnetostriction is accompanied by large anisotropy. In $TbFe_2$ the cubic anisotropy constant is $K_1 = -7.6 \times 10^7 \text{ergs/cm}^3$, the largest negative room temperature anisotropy constant of any cubic crystal[8]. $DyFe_2$ also shows large magnetostrictive effects at room temperature, $\lambda_s = 433 \times 10^{-6}$[9] and its cubic anisotropy constant $K_1 = 2.1 \times 10^7 \text{ergs/cm}^3$ is the largest known positive K_1[9]. In an attempt to generate an alloy with low anisotropy and high strain, the Tb in $TbFe_2$ was replaced by Dy atoms. A minimum in anisotropy, $K_1 \sim 0$ (at $\sim 8^{\circ}$C)[10] was obtained for the $Tb_{0.27}Dy_{0.73}Fe_2$ stoichiometry. It's room temperature saturation magnetostriction λ_s is 1068×10^{-6}[9]. The ternary alloy is known as Terfenol-D (Ter (Terbium) + Fe (iron) + nol (Naval Ordinance Laboratory) + D (Dysprosium)). The large magnetostriction and small anisotropy are an ideal combination for high power transducer applications because it allows easy magnetization rotation and a minimum hysteresis. Another distinctive feature of these alloys is that λ_{111}, the magnetostrictive strain in the [111] direction is much larger than λ_{100} the magnetostrictive strain measured in the [100] direction, ($\lambda_{111} >> \lambda_{100}$) a property unknown in other

cubic systems[11].

These record breaking properties can not all be explained by existing theories of magnetostriction for cubic materials. To explain $\lambda_{111} >> \lambda_{100}$ the double tetrahedron model was proposed[11],[12],[13]. It shows that coupling of the crystalline electrostatic fields with the total angular momentum of the 4f electrons gives rise to an internal distortion which in turn couples to the external strain. The model suggests that the Fe atoms do not contribute to this distortion. Structural evidence of a distorted lattice was obtained by x-ray diffraction experiments[11],[14],[15].

Ultrathin magnetic films form another class of technologically important magnetic materials because magnetic properties of the surfaces, the interfaces and also the new metastable phases grown possess magnetic properties not normally found in the bulk, such as strong perpendicular anisotropies, coercivity, and magneto-optic effects important for magneto-optic storage devices[16]. They are grown by molecular beam epitaxy (MBE), a technique permitting deposition of atoms in an almost layer-by-layer fashion. Lattice matching the epitaxial layer to the substrate template permits the creation of atomic structures with very sharp interfaces. The magnetic properties in the interface are often very different from those normally found in the bulk. Stabilized structures that do not exist in nature can be formed by varying the growth con-

ditions. In ultrathin films the energies associated with a change in magnetic structure and a change in lattice structure are comparable. Therefore this leads to materials whose magnetic properties can be controlled by controlling the growth conditions. Some novel magnetic properties discovered in these thin films are antiferromagnetic coupling between two ferromagnetic layers separated by a non-magnetic spacer[17] (referred to as trilayers), giant magnetic anisotropies[18],[19] and giant magnetoresistance in antiferromagnetically coupled Fe layers[20].

Ultrathin films of interest in this thesis are Fe/Cu/Fe trilayers grown on Ag(001) single crystals by molecular beam epitaxy. These trilayers typically 20Å to 35Å in total thickness are either antiferromagnetic or ferromagnetic depending on the thickness of the non-magnetic spacer, Cu[21]. This is also the first system for which a long wavelength oscillation of the exchange coupling with spacer layer thickness was established for a simple metal[22],[23].

The growth of these ultrathin structures depends on how well the lattice is matched with the underlying layer. In several similar systems a new phase has been generated where the overlayers were forced to take on the structure of the template onto which they were being deposited[24],[25]. The lattice mismatch between Fe and Ag is small and Fe atoms stack themselves in their usual bulk bcc structure. There exists a large mismatch between the unit cells of Fe and

of Cu. Layer-by-layer growth of Cu on Fe still proceeds with the Cu following the bcc stacking dictated by the Fe template for several layers before gradually transforming to a fcc structure. It will be shown in this thesis that even at a thicknesses of 20ML the Cu has not achieved the bulk fcc structure of Cu.

In both Terfenol-D and the MBE films, the materials were engineered to have specific magnetic properties. The arrangement of the atoms in the final product has important consequences on the properties of interest. Hence structural information becomes important. To solve structural problems many techniques exists, such as x-ray diffraction (XRD), reflection high energy electron diffraction (RHEED), low energy electron diffraction (LEED), to name a few. RHEED is used during the growth of thin films to monitor the film thickness[26], in-plane lattice constants and symmetry[27]. However it can not obtain the lattice spacing perpendicular to the surface, nor can it determine the arrangements of different atomic species in the surface unit cell. LEED is a more established technique that requires a thorough consideration of electron multiple scattering. It has been applied to some metastable metallic films[28], [29]. XRD can be interpreted by relatively simple kinematic theories. In the glancing-incidence geometry it has a surface sensitivity comparable to other techniques[30] and has been shown to be a powerful tool for determining the structure of reconstructed surfaces[31],[32],[33],[34],[35] provided the noninteger

indices of the surface Bragg rods can be easily separated from the bulk signal.

In this work, the primary concern is to determine the local structure of Terfenol-D and Fe/Cu/Fe trilayers using x-ray absorption fine structure spectroscopy (XAFS). From XAFS data, interatomic distances, number and identity of coordinating atoms, the correlated motion of atoms (local lattice dynamics), bond angles and the valence state of the absorbing atom can be obtained. XAFS is a short range order probe with element specific sensitivity which treats crystalline and non-crystalline solids on the same basis. XAFS can be taken in transmission, fluorescence, reflectivity or electron yield modes[36]. With such a wide array of detection modes constraints placed on the preparation of samples is lifted, permitting the application of XAFS to a diverse range of materials. Even very low concentration species ($\sim$ppm) are acceptable because this is an absorption technique. Since it is a short range probe it can not provide long range order information like diffraction techniques but it can complement them.

Since XAFS is element specific an XAFS study of Terfenol-D should reveal any displacement of the Fe and/or the rare-earth atoms to verify the validity of the double tetrahedron model. XAFS in electron yield mode was used for this purpose because the sample thickness ($\approx$1mm) disallowed a transmission experiment. Furthermore since the sample was placed in a magnetic field the geometrical constraints did not allow the measurement of fluorescence.

X-rays impinging on the Fe/Cu/Fe trilayers at glancing incidence angle are confined to the surface region by total reflection permitting XAFS of specific interfaces to be studied. Again the element specific characteristic of XAFS permits one to probe buried interfaces. In this thesis XAFS for varying Cu thicknesses in the Fe/Cu/Fe trilayers will be measured to determine the local structure of the Cu.

The thesis consists of 7 chapters. Chapter 2 deals with XAFS. It outlines the factors that contribute to the XAFS signal and techniques of data analysis which will be used to extract structural parameters. Terfenol-D is introduced in Chapter 3. The general theory of magnetostriction is developed in this chapter and the double tetrahedron model to explain the source of large anisotropy in the magnetostriction of Terfenol-D is also discussed. Chapter 4 is devoted to the XAFS experiment on Terfenol-D. Chapter 5 describes the molecular beam epitaxy growth of the Fe/Cu/Fe trilayers and the structural results obtained from RHEED measurements made during the growth. The glancing-incidence XAFS experiment of Cu in the trilayers and the results are presented in Chapter 6. Finally chapter 7 summarizes the results of XAFS on these two magnetic systems.

2 X-Ray Absorption Fine Structure

2.1 Introduction

The dominant absorption mechanism for low energy x-rays is the photoelectric effect. As soon as a photon has enough energy to free a bound electron in the absorbing atom a sudden decrease in the transmitted intensity occurs, indicating an absorption edge. Edges are labelled according to which electron is missing in the excited state. For example the K edge is the absorption edge when a 1s electron has been freed. The L_I edge occurs when an electron has been removed from the 2s level and the L_{II} and L_{III} edges involve $2p_{1/2}$, $2p_{3/2}$ levels respectively. If the atom is isolated, the absorption will decrease monotonically beyond the edge as $\frac{1}{E^3}$, indicating an increase in transparency with increasing energy. On the other hand, if the atom is in a condensed state, a more rapidly oscillating signal is superimposed on the smoothly decreasing background. This signal is the XAFS, x-ray absorption fine structure. It is usually separated into two regions, the first ~30eV above the edge which is called the x-ray absorption near edge structure, XANES, and the higher energy region called the extended x-ray absorption fine structure EXAFS. EXAFS yields information about the interatomic distances, near neighbor coordination numbers, and correlated motion of the atoms. XANES gives information about the valence state of the absorbing atom and structural information about the stereogeometry of the lo-

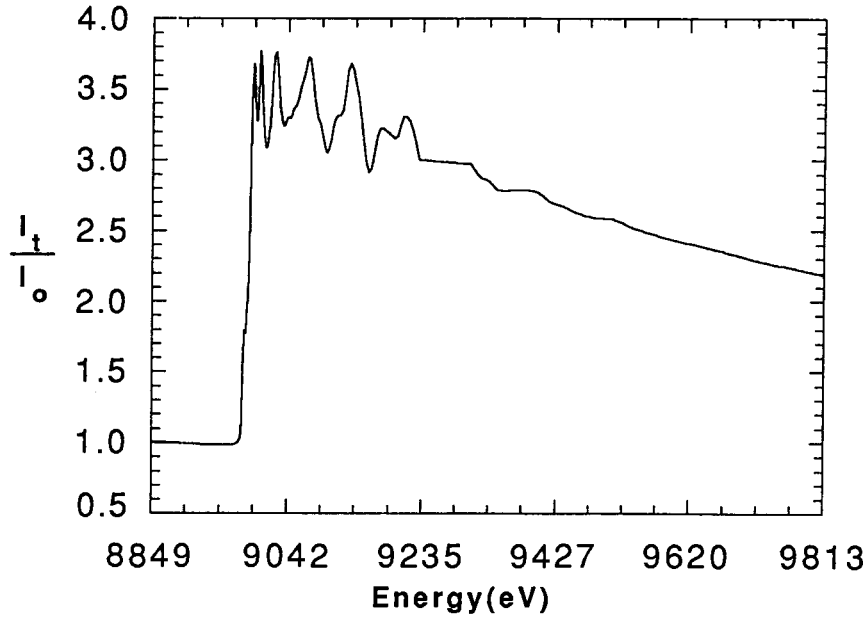

Figure 1: Absorption of the Cu K edge.

cal arrangement of atoms. A typical absorption spectra is shown in figure 1.

The simplest way of visualizing this phenomenon is to realize that the outgoing photoelectron can be represented by a wave. In a condensed state this wave will encounter other atoms in the neighbourhood of the absorbing atom which will scatter the outgoing wave. Hence, the final state is a superposition of the outgoing wave and the scattered waves. This is depicted in figure 2.

Quantum mechanically the transition probability and hence the absorption coefficient μ, can be calculated by the Golden rule of first order perturbation theory with the initial state $|i>$ being dipole coupled to the final state $|f>$

$$\mu \propto |<i|\hat{\epsilon}\cdot\vec{p}|f>|^2\rho(E). \tag{1}$$

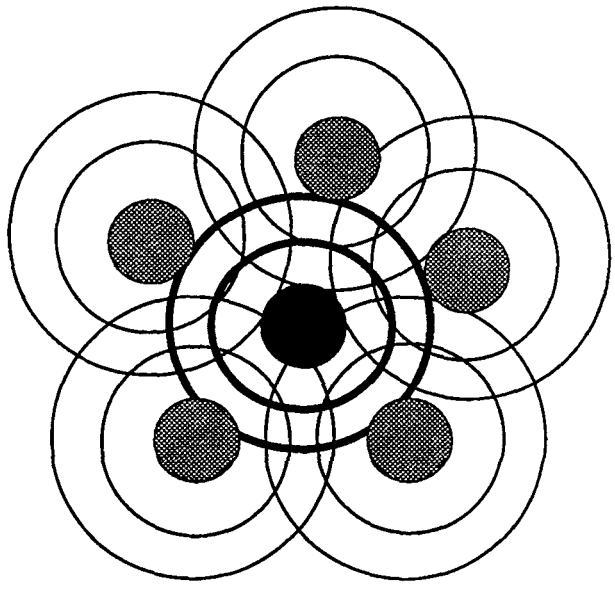

Figure 2: Simple physical picture of absorption process in condensed matter. Thick line is the outgoing wave, the thin lines are the scattered waves and the absorbing atom is at the center.

The dipole selection rule is $\Delta l = \pm 1$. When the initial state is a K or L_I state the final unoccupied state must have p symmetry. When the initial state is a L_{II} or L_{III} p state the final state must have either d or s symmetry. In practice the p to d transitions dominate.

$\rho(E)$ is the density of states per unit energy at the energy of the final state, $\vec{p}$ is the momentum operator of the photoelectron and $\hat{\epsilon}$ is the electric field vector of the incident x-ray. The experiments reported here were done with the synchrotron radiation produced by the wiggler on Beamline IV-1, Stanford Synchrotron Radiation Laboratory. The radiation is linearly polarized in the horizontal plane of the wiggler which is also the plane of the storage ring.

At the absorbing atom the backscattered wave will add or subtract from the outgoing wave depending on their relative phase. It is in fact an interference effect. The scattered wave depends on the charge density of the atoms that surround the absorbing atom. Therefore, the final interference effect is highly dependent upon the type of neighbouring atoms and their distance to the absorbing atom. This is the basis of EXAFS's utility as a structural tool.

The simplest expression for the oscillatory part of the absorption spectrum in condensed matter is based on the plane wave approximation. In this approximation the complex scattering amplitude is calculated assuming it is a plane wave. If all neighboring atoms around the absorber are held rigidly at R_j and the environment around the absorbers is identical then,

$$\chi(k) = \sum_j \frac{(-1)^l F_j(\pi, k)}{kR_j^2} \sin(2kR_j + \phi_j(\pi, k) + 2\delta_l) \cdot \qquad (2)$$

The wavevector is denoted by k. The angular momentum of the electron after absorption of a photon, is given by l. It is 1 for K and L_I shells and 2 for L_{II} and L_{III}. F is the amplitude of an electron scattered through an angle π by the atom at site j and ϕ is its phase change.

The origin of the terms in the total phase can be understood from a simple picture. The photoelectron leaves the origin and has a radial function phase shift δ_l by passing out of the absorber atom potential. It travels towards an atom at R_j changing phase by kR_j. It is scattered back with the phase change

$\phi_j(\pi, k)$. The return to the origin causes yet another phase change of $kR_j + \delta_l$. Therefore, the total phase is $2kR_j + \phi_j(\pi, k) + 2\delta_l$.

In the amplitude term, there are 2 factors of $1/R_j$. They arise because of the return trip in going from the origin to site R_j. This $1/R^2$ is partly responsible for suppressing the contributions from distant neighbors. Another more important factor which cuts down the effects of distant neighbours is inelastic scattering (which will be included in equation 8). Note that $\chi(k)$ as described above is only the first term of a perturbative expansion. The next term would involve an electron going out from the absorber being scattered through an angle θ by the atom at site i towards an atom at site j and finally being scattered back to its origin. This is the double scattering term. Of course $\chi(k)$ can be expanded to even higher terms. The double scattering terms and the higher terms are referred to as the multiple scattering terms.

Returning to the single scattering expression there are additions that need to be made. Firstly, there may be several atoms in a spherical shell of mean radius R_j. The polarization of the incoming x-rays indicated by equation 1 must be taken into account. When this is done the number of atoms at distance R_j for the K and L_I shells is written as[37],

$$N_j^* = 3\sum_{i=1}^{N_j} \cos^2 \alpha_i \tag{3}$$

where N_j is the total number of atoms in the j^{th} shell and α_i is the angle

between the electric vector $\hat{\epsilon}$ and the radial vector from the x-ray absorbing atom to the scatterer of the photoelectron. For inherently anisotropic systems this polarization dependence of the EXAFS signal provides a powerful tool to sort out neighbor atoms directions from the central atom. For polycrystalline samples a random average over α_j in three dimensions yields,

$$N_j^* = \sum_{i=1}^{N_j} \langle 3\cos^2 \alpha_i \rangle = N_j. \tag{4}$$

Secondly, it was assumed that the neighboring atoms were stationary at R_j. In actual fact they are always in motion and site j is simply the average position of the atom. Let's suppose that the motion of the absorber and the scatterers is such that the distribution of the relative displacement due to thermal vibrations and static disorder can be described by a Gaussian[38],

$$P(r_j) = \frac{1}{(2\pi\sigma_j^2)^{\frac{1}{2}}} e^{-(r_j - R_j)^2/2\sigma_j^2} \tag{5}$$

where $\sigma_j^2 = \langle (r_j - R_j)^2 \rangle$ is the mean square variation in bond length. Including the coordination number and the motion of the atoms $\chi(k)$ is written as

$$\chi(k) = \sum_j (-1)^l F_j(\pi, k) N_j \int \frac{P(r_j)}{k r_j^2} \sin(2kr_j + \phi_j(\pi, k) + 2\delta_l) dr_j \tag{6}$$

which reduces to

$$\chi(k) = \sum_j \frac{(-1)^l N_j e^{-2\sigma_j^2 k^2}}{k R_j^2} F_j(\pi, k) \sin(2kR_j + \phi_j(\pi, k) + 2\delta_l) \tag{7}$$

where the summation is over the j^{th} shell of radius R_j. The exponential term is the EXAFS Debye-Waller factor.

Other factors that have not been included are the effect of the other electrons and inelastic scattering. Since the absorption process leaves behind an ionized atom the potential seen by the other electrons has changed. The shielding of the positive nucleus by the core electron is removed as the atom is excited by removing that core electron. This increases the attraction of the nucleus for the other passive electrons and relaxes them to a lower energy. This introduces a many-body amplitude decreasing factor usually labelled as S_0^2 which takes into account the overlap between the initial and final passive electron states. This factor is typically about 0.7 to 1.0[39].

Inelastic scattering, where the electron excites other electrons and loses some energy in the process as well as its phase correlation with the incoming photon, occurs. The probability of such an event increases as the number of electrons the outgoing electron meets, or as the total path length increases. This is included in the EXAFS formula by a phenomenological amplitude reduction factor $\exp^{-2R_j/\lambda}$. Therefore, the final form of the single-scattering EXAFS formula is,

$$\chi(k) = \sum_j S_0^2 \frac{(-1)^l N_j e^{-2\sigma_j^2 k^2} e^{-R_j/\lambda}}{kR_j^2} F_j(\pi, k) \sin(2kR_j + \phi_j(\pi, k) + 2\delta_l). \quad (8)$$

In reality, calculating the complex scattering amplitude in the plane wave approximation is valid only at the asymptotic limit. In condensed matter the atoms are close and the scattering will occur before this limit is reached. Rehr[40] has taken into account the spherical wave nature of the photoelectron,

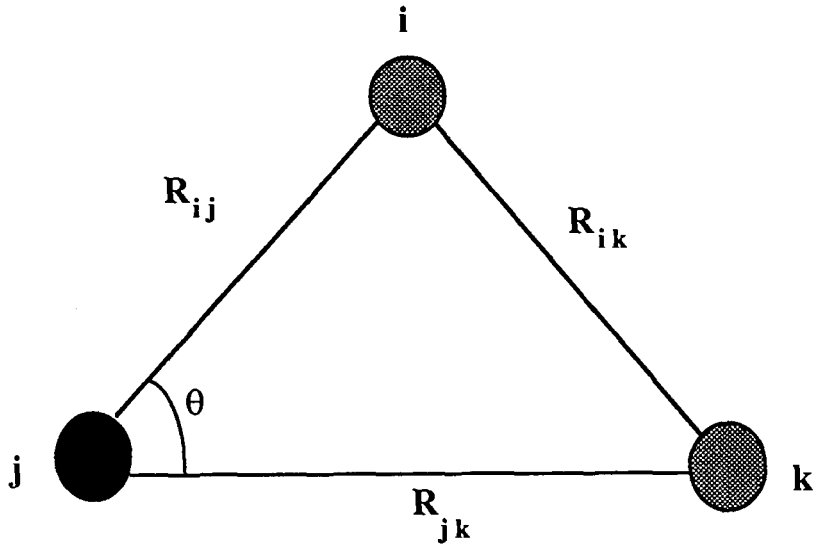

Figure 3: Multiple scattering event.

but retained the simplicity of the plane wave result. The EXAFS equation keeps the same form except $F_j(\pi, k)$ and $\phi_j(\pi, k)$ are replaced by $F_j(\theta, kR_{ij}, kR_{jk})$ and $\phi_j(\theta, kR_{ij}, kR_{jk})$, where θ is the scattering angle, R_{ij} is the distance from the previous scatterer and R_{jk} is the distance to the future scatterer (figure 3). The EXAFS equation is then written,

$$\begin{aligned} \chi(k) = \quad & \Sigma_j \quad S_0^2 \frac{(-1)^l N_j e^{-2\sigma^2 k^2} e^{-R_j/\lambda}}{kR_j^2} F_j(\theta, kR_{ij}, kR_{jk}) \\ & \times \quad \sin(2kR_j + \phi_j(\theta, kR_{ij}, kR_{jk}) + 2\delta_l). \end{aligned} \tag{9}$$

This equation is a valid approximation when a high degree of local order is preserved. Cases where the degree of disorder is larger are encountered frequently and the use of an effective distribution $P(R_j)e^{-2R_j/\lambda}/R^2$ neglects errors relative to the real distribution of order $(\sigma^2/\bar{R}^2)(1 + \bar{R}/\lambda)$[41].

The previous description is simply to give a better physical picture of the process involved in EXAFS. A formal derivation of the EXAFS equation, in the plane wave approximation, can be found in reference [42] for example.

2.2 Data analysis

There are three common modes of collecting EXAFS data; from a transmission experiment, from a fluorescence experiment and from a total electron yield experiment. In a transmission experiment the incident intensity and the transmitted intensity are measured as a function of energy and these are related to the absorption coefficient $\mu(E)$ by

$$I_t = I_0 e^{-\mu(E)x} \tag{10}$$

where the thickness of the sample is x. Fluorescence XAFS involves the measurement of the photons generated when the inner shell vacancy is filled by an outer shell electron. For fluorescence of thick samples this is written as[36]

$$\frac{I_f}{I_0} \sim \int_\phi \frac{\mu(E)\sin\theta d\phi}{\mu_T(E)/\sin\theta + \mu_T(E_f)/\sin\phi}. \tag{11}$$

The total absorption coefficient at energy E is denoted by $\mu_T(E)$, the fluorescence energy is E_f, θ is the entrance angle of the incident x-rays and ϕ is the exit angle of the fluorescent x-rays. The integration is over all angles subtended by the detector. In the case of dilute samples the total absorption coefficient is nearly a constant and the correction to the measured signal to obtain $\mu(E)$

is small so that $I_f \sim \mu(E)I_0$. Figure 4 shows a typical spectrum taken in fluorescent mode.

The total electron yield mode measures the initial inner core electron, all the Auger electrons and the secondary electrons. The ratio of the intensity of detected electron to the incident intensity is[37]

$$\frac{I_e}{I_0} = \epsilon_B g \omega \langle \frac{\mu_B L}{1 + \mu_B L} \rangle \tag{12}$$

where ϵ_B is the electron detection efficiency, g is a smoothly varying function of photon energy to describe the inelastic scattering process, μ_B is the bulk absorption coefficient, ω is the solid angle of detection and L is the effective sampling depth. At photon energies used in EXAFS the x-ray penetration depth $1/\mu_B$ will always be larger than the electron escape depth. Therefore the total electron yield signal becomes proportional to the absorption coefficient. All the data in this thesis is taken in either the fluorescent mode or total electron yield mode.

As described earlier, the EXAFS interference function $\chi(k)$ is the oscillatory part of the spectrum present above the edge. Extracting it requires taking the difference of $\mu(E) - \mu_0(E)$ where $\mu_0(E)$ is the smooth background. The result is normalized to a per atom basis by dividing by $\mu_0(E)$:

$$\chi(E) = \frac{\mu(E) - \mu_0(E)}{\mu_0(E)} . \tag{13}$$

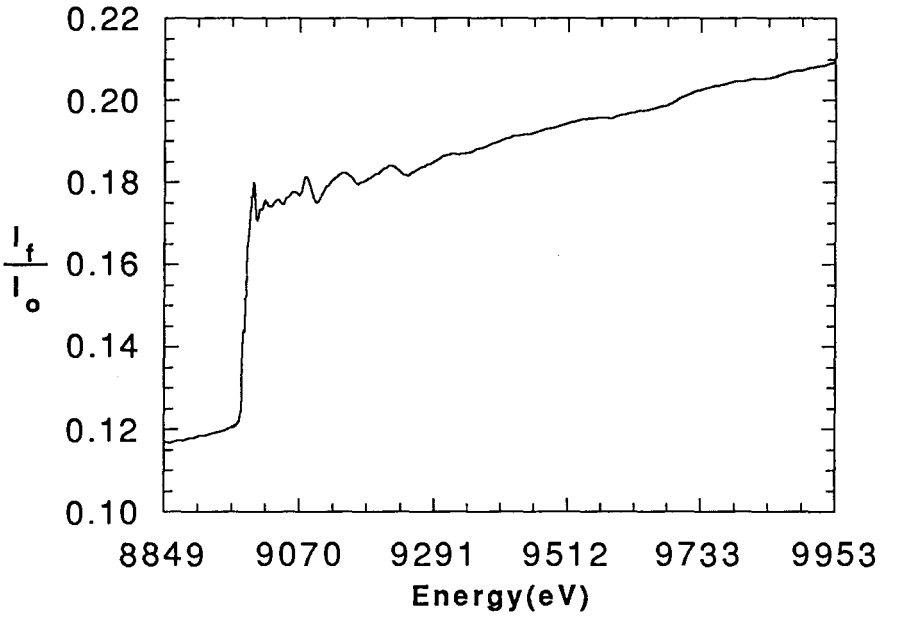

Figure 4: Fluorescent XAFS spectrum of 8ML of copper in 10ML Au/5ML Fe/8ML Cu/8ML Fe grown by MBE on Ag(001). The spectrum was taken with x-rays impinging on the sample at glancing incidence.

The first step is to determine the origin for the k-space scale. The first approximation for this is the threshold for absorption identified by the first inflection point E_0. This point is best obtained from the derivative of the data. Since $\mu_0(E)$ is unknown, equation 13 can be approximated by

$$\chi(E) = \frac{\mu(E) - \mu_b(E)}{\Delta\mu(E_0)}. \tag{14}$$

where μ_b is the background of the measured data for energies greater than E_0. $\Delta\mu(E_0)$ is the change in the absorption background at the edge energy E_0.

$\Delta\mu(E_0)$ is a constant and is equivalent to taking the height of the jump. To determine the onset of the jump in a consistent fashion a linear least squares fit was applied to the first 100eV (~30 points) of the data in the regime before the

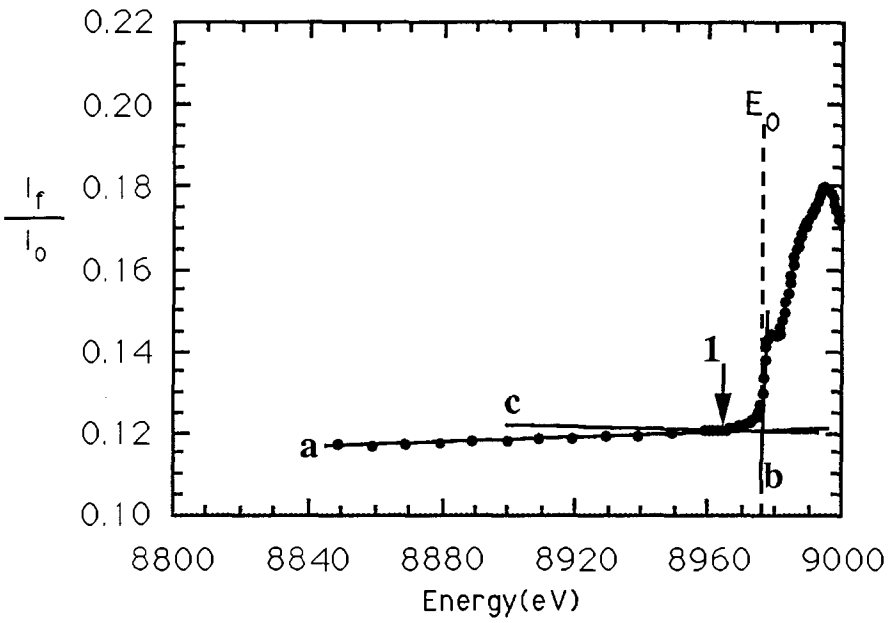

Figure 5: Procedure to obtain $\Delta\mu(E_0)$.

edge, and another fit to the 5 to 8 points around the edge energy (see figure 5). These lines are labelled **a** and **b** respectively. A horizontal line (line **c**) passing through the intersection point of these two lines intersects the data at point 1. This point defines the onset of the jump. A least squares linear fit is then applied to the data between 25eV to 200eV above the edge, extrapolated to the edge energy and the jump height obtained (see figure 5). The data for energies greater than E_0 is converted from the x-ray energy scale to the k-space of the photoelectron according to the relation

$$k = \sqrt{\frac{2m(E - E_0)}{\hbar^2}}. \tag{15}$$

The next step is the removal of the smooth low frequency component of the background, $\mu_b(E)$. This is done by removing a polynomial of n^{th} order from

the data above the edge. The signal that remains is the EXAFS interference function. Since $\chi(k)$ is a sum of sinusoidal functions of different frequencies Fourier analysing $\chi(k)$ separates the radial contributions to the radial distribution function[43]. Before doing the Fourier transform, the data is interpolated such that it is on an evenly spaced k-space grid. The range of the data is limited to the region between k_{min} and k_{max}, therefore application of a Fourier transform is equivalent to taking the Fourier transform of a convolution of a square window with the data. The result of processing data sets finite in k-space is spectral leakage. The sharp discontinuity at the boundaries (k_{min} and k_{max}) produce sidelobes in the Fourier transform. One method of reducing the size of these sidelobes is by applying a window function that tapers to zero at the boundaries. Several windows achieve this to varying degrees[44]. The two window functions used in this work are the Hamming window defined as,

$$w_H(k) = .54 + .46\cos\left(\pi\frac{2(k - k_{mid})}{\Delta k}\right) \tag{16}$$

and the 10% Gaussian window defined as,

$$w_G(k) = \exp\left[\left(\frac{2(k - k_{mid})}{\Delta k}\right)^2 \times \ln(.1)\right] \tag{17}$$

where $\Delta k = k_{max} - k_{min}$ and k_{mid} is the midpoint of the data. Figure 6 is the graphical representation of the two windows.

The Fourier transform taken is the discrete equivalent of the analytical trans-

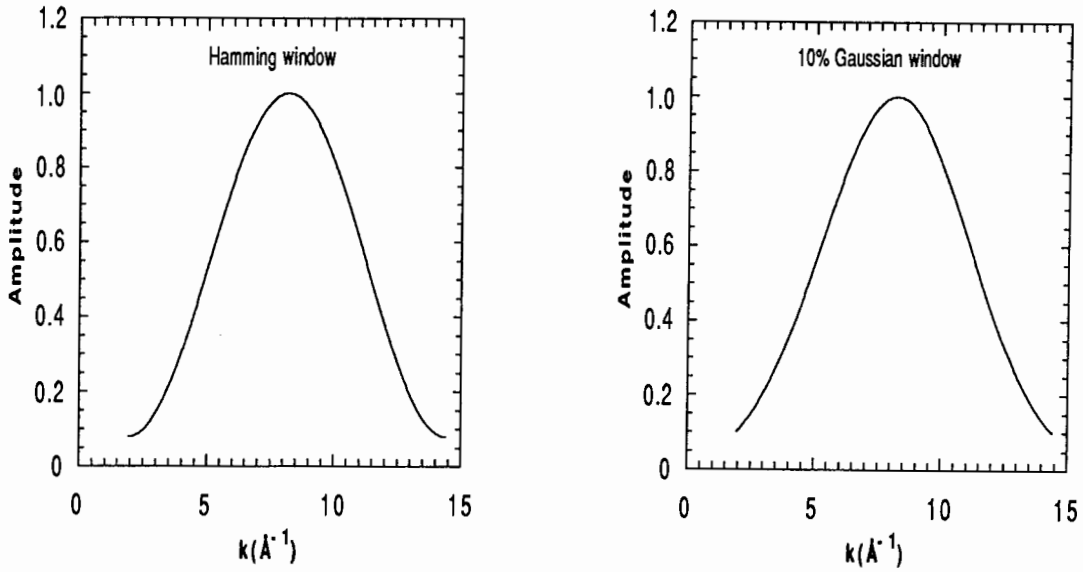

Figure 6: Hamming window and 10% Gaussian window functions.

form

$$\frac{1}{\sqrt{\pi}} \int_{-\infty}^{\infty} \frac{-1}{2i} w(k) k^p \chi(k) e^{2ikR_j} dk \tag{18}$$

where $w(k)$ is the window function and k^p is used to weight the data at higher k. A peak in the Fourier transform (figure 7), which may contain one or more shells, is isolated and inverse Fourier transformed. This process is referred to as Fourier filtering. The resultant can be separated into amplitude and phase terms. At this point several methods can be applied to extract information from the data.

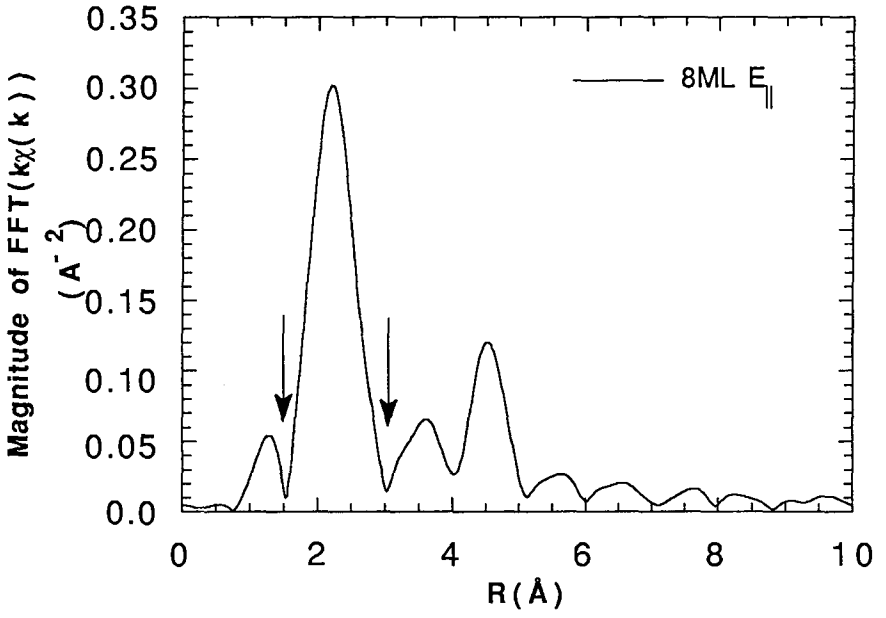

Figure 7: Fourier transform of $\chi(k)$ for 8ML Cu grown by MBE. The peak between the two arrows is the data that will be inverse Fourier transformed.

2.2.1 The Log-Ratio Method

The log-ratio method is only applicable to a peak that is known to contain one single shell only. It involves the comparison of the amplitude to a reference compound. The reference compound is analysed in the same way as the data for the unknown. Taking the natural logarithm of the ratio of the amplitude of the unknown and the reference as a function of k^2 will give a straight line, whose slope is

$$slope = -2(\sigma_u^2 - \sigma_r^2) \tag{19}$$

and its intercept is

$$intercept = \ln \frac{S_{0u}^2 N_u F_u(k) R_r^2}{S_{0r}^2 N_r F_r(k) R_u^2} \tag{20}$$

which follows from equation 8. The subscript u indicates the unknown while the subscript r refers to the reference compound. If the backscattering elements are the same in the reference and the unknown the F_n will cancel. If the absorbing atoms are the same and the local environments are similar, the S_0^2 also cancel.

2.2.2 Phase Difference Method

The phase difference method is closely related to the log-ratio method in that the unknown signal is compared with a reference after Fourier filtering. Again it is only applicable to a peak that is known to contain one single shell only. Let the total phase for the unknown for a single shell be,

$$\Phi^u = 2kR^u + \phi^u(\pi, k) + 2\delta_l^u \tag{21}$$

and the total phase for a single shell of the reference compound be,

$$\Phi^r = 2kR^r + \phi^r(\pi, k) + 2\delta_l^r \tag{22}$$

where the superscript u and r denote the unknown and the reference compound respectively. Assuming that the EXAFS phase shift, $\phi(\pi, k) + 2\delta_l$ is transferable from the reference to the unknown, then the difference of these two expressions yields,

$$\Phi^u - \Phi^r = 2k(R^u - R^r) \tag{23}$$

Hence, if the distance of the reference is known, it is a simple matter to fit this equation and extract the distance of the unknown.

2.2.3 The Beating Method

In many systems the Fourier transform is unable to resolve two closely spaced shells and the two shells appear as a single peak. In practice it has been observed that the separation ΔR for which two shells are clearly separated in the magnitude of the Fourier transform is 0.3-0.4Å when only $\approx 10\text{Å}^{-1}$ of data is available[45]. To verify the presence or the absence of a second shell in the vicinity of the first, beating analysis can be done. After Fourier filtering, if there are two closely spaced shells, kinks will be present in the phase and also in the amplitude. After Fourier filtering the first peak in the Fourier transform, the $\chi(k)$ for the two closely spaced shells is given by[45],

$$\chi(k) = \frac{\tilde{A}(k)}{k} \sin(2k\bar{R} + \tilde{\phi}(k)) \tag{24}$$

where

$$\frac{\tilde{A}(k)}{k} = \frac{A_1(k)}{k}\left[1 + C^2(k) + 2C(k)\cos(2k\Delta R)\right]^{\frac{1}{2}} \tag{25}$$

$$\tilde{\phi}(k) = \phi_1(k) + \arctan\left(\left[\frac{-(1-C(k))}{1+C(k)}\right]\tan(k\Delta R)\right) \tag{26}$$

$$C(k) = \frac{A_2(k)}{A_1(k)} \tag{27}$$

$$\bar{R} = \frac{R_1 + R_2}{2} \tag{28}$$

$$\Delta R = R_2 - R_1. \tag{29}$$

Changes in slope (or kinks) in the phase and the amplitude will occur at approximately,

$$k_n \simeq \frac{n\pi}{2\Delta R} \tag{30}$$

where n is an odd integer. To extract a value of ΔR the derivatives should be taken since a kink will then become a dip or a peak, which is easier to identify. An example of the beating of two shells occurs in Fe metal. Fe has a body centre cubic structure with $R_1 = 2.485$Å, $R_2 = 2.87$Å[46] and $\Delta R = .385$Å. The derivative of the phase is shown in figure 8. All curves are the derivative of the phase but each has a different window applied during the Fourier transform. The type of window used should have no effect on the location of beats. The use of different windows can be used to distinguish between a true beat and transform artifacts. Note that the large peak at ≈ 16Å^{-1} is due to transform artifacts, a consequence of Fourier filtering, and is not a beat.

2.2.4 The Curve-Fitting Method

A multi-shell curve fitting program, based on Marquardt's algorithm[47] is used in this thesis. The program fits to the following expression[48]:

$$\chi(k) = \sum_j \frac{N_j}{k_j R_j^2} \; e^{-(2R_j+s_j)^2\tau^2/8\gamma^2 k_j^2} e^{-2R_j/\lambda} e^{(2/3)C_{4j}k_j^4} A_j(k_j) e^{-2\sigma_j^2 k_j^2} \times \sin(2k_j R_j + \delta_j(k_j) + a_j - (4/3)C_{3j}k_j^3). \tag{31}$$

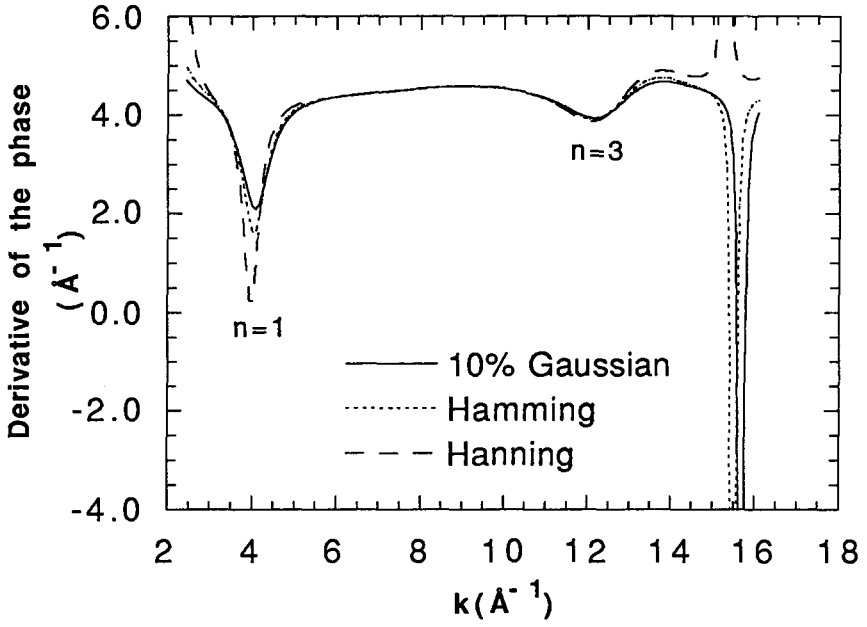

Figure 8: Derivative of the phase for Fe K shell. The Fourier transform of $k\chi(k)$ was taken over the range 2.40Å^{-1} to 16.13Å^{-1}. The Fourier filtering range was 1.31Å to 2.97Å.

The sum is over all coordination shells. The magnitude of the wave vector of the electron is given by k, and k_j is related to k according to

$$k_j = \sqrt{k^2 - \frac{\Delta E_j}{\gamma}} \tag{32}$$

where $\gamma \equiv \frac{\hbar^2}{8\pi^2 m_e} \simeq 3.81\text{eV Å}^2$. ΔE_j is a correction of the inner potential. R_j is the radius of the shell with coordination number N_j and σ_j^2 is the mean square relative displacement describing thermal and static disorder. a_j is a k independent phase correction to the total phase to allow for errors in the reference phase. C_{3j} and C_{4j} are cumulants of the distribution function which become important when there are deviations from a Gaussian distribution function due to asymmetry, and s_j and τ describe the effect of the monochromator resolution[49].

λ is the mean free path. The fits can be done in k-space or in R-space. The k-space fit can be done to the full $\chi(k)$ but it is normally done to Fourier filtered data, thus limiting the fits to one or two shells. The data and the model are treated the same way, so, in principle, transform artifacts are present in both equally.

A measure of the deviations of the fit is calculated to aid in determining the goodness of the fit. This measure is called χ^2. For a k-space fit it is defined as

$$\chi^2 = \left(\frac{n_{free}}{n_{free} - n}\right) \frac{1}{M_k} \sum_{i=1}^{M_k} [(y_i - \chi(k_i))k_i^p]^2 w_k(k_i) \tag{33}$$

and for a R-space fit this becomes

$$\chi^2 = \left(\frac{n_{free}}{n_{free} - n}\right) \frac{1}{2M_R} \sum_{i=1}^{M_R} ([\Re(\mathsf{FT}(k^p y)) - \Re(\mathsf{FT}(k^p \chi(k)))]_i^2 + [\Im(\mathsf{FT}(k^p y)) - \Im(\mathsf{FT}(k^p \chi(k)))]_i^2) w_R(R_i) \tag{34}$$

where FT is a Fourier transform and k_i^p is a k space weighting used in taking the Fourier transform. In k-space there are M_K points while in R-space there are M_R points. The data are given by y and for a k-space fit, if Fourier filtering has been used, this is the filtered data. A weighting function, $w_k(k)$ and $w_R(R)$ for k and R space respectively, removes the effect of the total amplitude of the data. In k-space it is the reciprocal of the square of the envelope of $k^p y$ and in R-space it is the square of the magnitude of the Fourier transform. n is the number of variable parameters and $n_{free} = \frac{2}{n_{FFT}}(M_R - 1)(M_k - 1) + 1$ is the maximum number of variable parameters and is always $\geq n$[48].

The amplitude and phase can be extracted from a reference compound of similar nature to the unknown or taken from tables generated by some theoretical model. One such model is the FEFF code[50], which implements equation 10 including multiple scattering paths.

In this work amplitude and phase will either be extracted from a suitable reference material or computed using FEFF 5.04. If reference amplitude and phase are used the mean free path term is inherently included and it is not an adjustable parameter during the curve fitting. Similarly when the FEFF amplitude and phase are used, the mean free path term calculated by this code was deemed to be a good estimate. This reduces the number of adjustable parameters. Asymmetry to a first approximation was assumed to be negligible, therefore C_{3j} and C_{4j} are assumed to be 0.

3 Terfenol-D system:

3.1 Introduction

Terfenol-D was synthesized by substitution of Tb atoms for Dy atoms in the cubic Laves structure of $TbFe_2$[9]. Tb and Dy are nearly indistinguishable, therefore Terfenol-D is also a cubic Laves phase structure of the $MgCu_2$ type, or the C15 structure (figure 9). The Laves structure can be thought of as

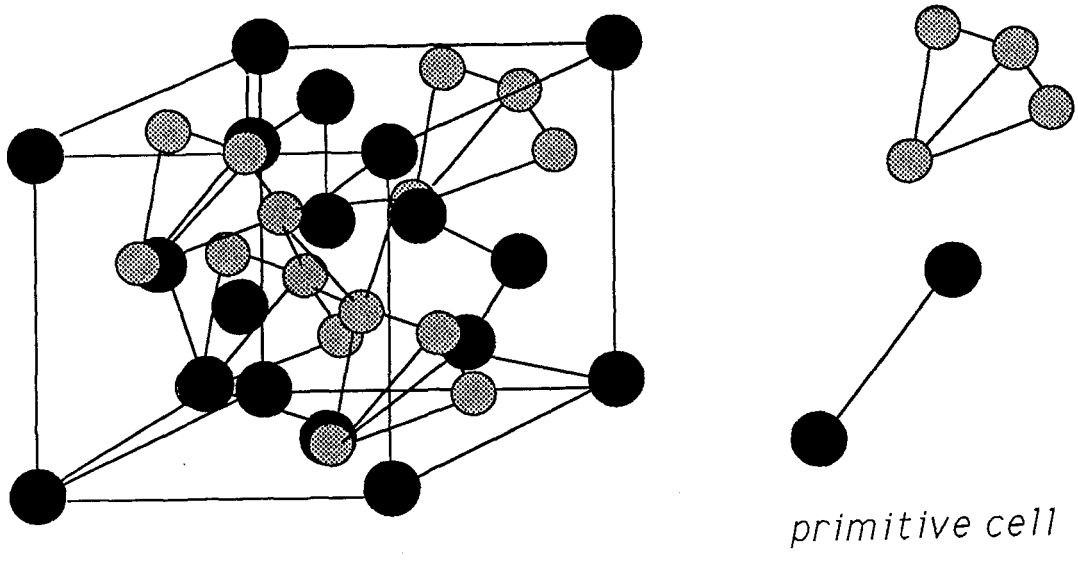

Figure 9: The cubic Laves phase structure. The rare earth atoms are represented by the large black spheres and the Fe atoms are represented by the smaller gray spheres.

consisting of two interpenetrating structures: a cubic framework, the diamond structure, for the rare-earth atoms and a framework of Fe tetrahedra joined at the apexes and occupying the open cavities of the rare-earth lattice. There are 2 rare-earth atoms and 4 iron atoms in the unit cell.

This material was the result of experiments on magnetic material properties. The binary alloys $TbFe_2$ and $DyFe_2$ both exhibited a giant magnetostrictive effect. Saturation magnetostriction for $TbFe_2$ was found to be 1753×10^{-6} and for $DyFe_2$, 433×10^{-6} was found[5],[9]. The measured anisotropy constants of these two binary alloys are the largest room temperature values for a cubic system. Anisotropy energy acts in such a way that the magnetization tends to be directed along certain definite crystallographic axes which are called the directions of easy magnetization. The directions along which it is most difficult to magnetize the sample are called the hard directions. The excess energy required to magnetize a crystal in a hard direction referred to the energy required to magnetize to saturation in the easy direction is defined as the anisotropy energy. The first order anisotropy constants are $K_1 = -7.6\times10^7 \text{ergs/cm}^3$[8] and $K_1 = 2.1 \times 10^7 \text{ergs/cm}^3$[9] respectively for $TbFe_2$ and $DyFe_2$. By substituting some of the Tb atoms for the Dy atoms the anisotropy constant K_1 was reduced to zero near room temperature[51],[6] for this ternary alloy.

The saturation magnetostriction was found to have remained quite high ($\lambda_s = 1068 \times 10^{-6}$)[9]. The magnetostriction as a function of field is plotted in figure 10.

X-ray diffraction[15], and neutron diffraction[52] studies on $TbFe_2$ demonstrated a rhombohedral distortion of the Laves phase at room temperature.

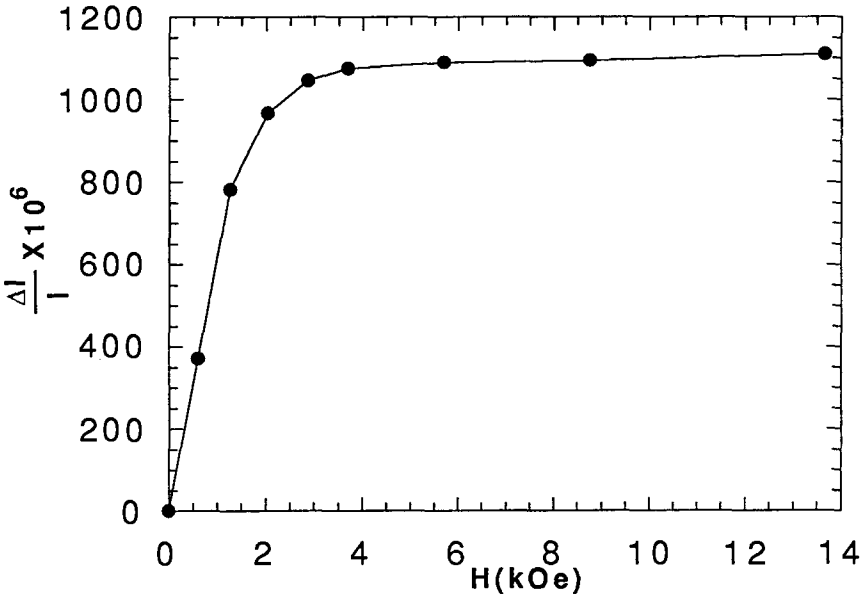

Figure 10: Magnetostriction as a function of field for $Tb_{.28}Dy_{.72}Fe_2$. (Data extracted from Savage et al.(1975) figure 5).

On Terfenol-D, x-ray diffraction[11],[14] studies also observe this rhombohedral distortion above the spin reorientation temperature. The spin reorientation temperature, T_s, is the temperature above which $\langle 111 \rangle$ is the direction of easy magnetization and below which $\langle 100 \rangle$ becomes easy for Terfenol-D. For this material it was found that $T_s = 10^0$C[14], [53]. Denoting the magnetostrictive strain measured in the $\langle 111 \rangle$ direction and the $\langle 100 \rangle$ direction by λ_{111} and λ_{100} respectively, then $\lambda_{111}/\lambda_{100} \sim 50$ at zero temperature[12]. It is unusual for λ_{111} to be greater than λ_{100} in cubic materials. The spontaneous distortion along the $\langle 111 \rangle$ direction is believed to be responsible for the large magnetostrictive effect and the fact that $\lambda_{111} > \lambda_{100}$.

3.2 Magnetostriction

In a crystalline solid, the magnetic moments interact not only with an external field and with each other but also with the crystal lattice. If this interaction varies with lattice strain the magnetic moments will effectively exert a force on the lattice and this is called magnetoelastic coupling. Magnetoelastic coupling is responsible for dynamic effects associated with the collective excitations of the coupled magnetic and crystal lattice. This is the means whereby a spin system in an excited state can transfer its excess energy to the lattice and so determines the spin damping which is responsible for the intrinsic line width of ferromagnetic resonance. The strength of the spin-phonon coupling studied by absorption of microwave phonons or by low temperature thermal conductivity is another dynamic effect. But magnetoelastic coupling also encompasses static effects which are usually referred to as magnetostriction. There are two principal effects that fall under the term magnetostriction. One is a uniform lattice distortion with respect to the paramagnetic phase, which coincides with the onset of magnetic order. The distortion can be separated in two parts: the isotropic part and the anisotropic part. The isotropic part depends only on the degree of magnetic order. It preserves the symmetry of the paramagnetic phase. The anisotropic part depends both on the magnetic order and on its direction within the lattice. The second effect that contributes to the magnetostriction

is a stress dependent term added to the magnetic free energy.

In the following, the conventional theory is developed in one dimension, and then it is extended to the more realistic case of three dimensions. The development presented here follows the one given by Lee[54]. Reservations about the conventional theory are outlined by Brown[55].

Magnetostriction occurs when there exists a contribution of magnetic origin to the free energy of a system. This contribution is linear in strain. Details such as anisotropy in the magnetization will be ignored. For an isolated crystal the Helmholtz free energy is

$$F = F_m + F_e \tag{35}$$

where F_m and F_e are the magnetic and elastic parts of the free energy respectively. It is assumed that the magnetic part, F_m, can be expanded as a Taylor series in the strain, e. This is written as

$$F_m = F_0 + V_0 B e + \frac{1}{2} V_0 B' e^2 + \cdots \tag{36}$$

where V_0 is the unstrained volume. The elastic part of the free energy is given by

$$F_e = \frac{1}{2} V_0 C' e^2. \tag{37}$$

The B term is a stress and is called the magnetoelastic constant. The B' term is a magnetic contribution to the elastic stiffness constant and C' is the lattice stiffness constant. The magnetic part of the stiffness constant is normally much

smaller than the lattice stiffness constant. These two terms can be combined into a total elastic stiffness constant, which will be denoted by C. The Helmholtz free energy is then,

$$F = F_0 + V_0 B e + \frac{1}{2} V_0 C e^2. \tag{38}$$

If the magnetic crystal is subjected to a system of externally applied stresses then the appropriate free energy is the Gibbs free energy. Gibbs free energy is given by

$$G = F - V_0 \sigma e \tag{39}$$

where σ is the external stress. Exactly as before, the free energy can be separated into a magnetic and an elastic term. The expression can be expanded by a Taylor expansion with σ as the variable. This yields

$$G = G_0 + V_0 (A - e)\sigma + \frac{1}{2} V_0 S \sigma^2. \tag{40}$$

A is a strain of magnetic origin, S is the sum of the lattice elastic modulus and a magnetic contribution to the elastic modulus.

Consider first the case when the external stress is zero. In this situation the free energy of the system is described by equation 38. The Gibbs free energy is simply a constant $G = G_0$. The equilibrium conditions are found by setting $\partial F / \partial e = 0$. Thus the spontaneous strains are given by,

$$e_s = -\frac{B}{C} = -BS \tag{41}$$

where $S = 1/C$. Therefore the equilibrium value of F is

$$F^{eq} = F_0 - \frac{1}{2}V_0 C e_s^2. \tag{42}$$

This demonstrates that when a spontaneous strain is allowed to occur the free energy of the system is reduced.

Now, consider a system with an external stress present. In this case equation 40 must be evaluated. Setting the condition $\partial G/\partial \sigma = 0$ will yield the equilibrium equation,

$$e = A + S\sigma. \tag{43}$$

This is simply a statement that the total strain is the sum of a magnetic term independent of stress and an elastic strain due to the external stress. Suppose $\sigma = 0$ then $e = A = -BS$. From this, the Gibbs free energy, when an external stress is applied, is given by

$$G = G_0 + V_0(-BS - e)\sigma + \frac{1}{2}V_0 S\sigma^2. \tag{44}$$

The zeroth terms, F_0 and G_0, are the free energy at zero lattice strain and the free energy at zero external stress. To obtain F_0 the total strain can be set to zero, i.e. $e = 0$. By equation 43 $A = -S\sigma_s$ where σ_s is the spontaneous stress. Then, equation 44 becomes

$$G = G_0 - \frac{1}{2}V_0 S\sigma_s^2. \tag{45}$$

In this situation, by equation 38 and 39, $G = F = F_0$. Using 45 gives

$$F_0 = G_0 + \frac{1}{2}V_0AB. \tag{46}$$

Therefore, to calculate all magnetoelastic effects to this order only the knowledge of S and C, the compliance and stiffness constants respectively, A, the magnetic strain, and B, the magnetoelastic constant, are required.

In three dimensions the derivation is more complicated because the stresses, the strains, the compliance and the stiffness are tensors. The anisotropy energy in an unstrained crystal is

$$F_0 = K_0 + K_1(\alpha_1^2\alpha_2^2 + \alpha_2^2\alpha_3^2 + \alpha_3^2\alpha_1^2) + K_2\alpha_1^2\alpha_2^2\alpha_3^2 + ... \tag{47}$$

where K_1 and K_2 are the anisotropy constants at zero strain. The α's are the direction cosine of the magnetization with respect to the crystal axis. When the crystal is in a strained state, the anisotropy energy will depend on the strain. As was done in the one dimensional case, the anisotropy energy is expanded in a Taylor series. A summary is given in appendix I. It is found that if the elongation is observed in the [100] direction then,

$$e(100,100) = \lambda_{100} = -\frac{2}{3}\frac{b_1}{(c_{11} - c_{12})}. \tag{48}$$

Similarly for the [111] direction,

$$e(111,111) = \lambda_{111} = -\frac{1}{3}\frac{b_2}{c_{44}} \tag{49}$$

where b_i are magnetoelastic coupling constants and c_{ij} are the stiffness constants. For polycrystalline materials the magnetostriction is calculated by averaging equation A22 over different crystal orientations by assuming $\alpha_i = \beta_i \quad (i = 1, 2, 3)$. This then gives

$$\lambda = \frac{2}{5}\lambda_{100} + \frac{3}{5}\lambda_{111}. \tag{50}$$

Since $\lambda_{111} > 50\lambda_{100}$, then λ shown in figure 10 is determined mainly by λ_{111}.

3.3 Double-Tetrahedron Model

The rare earth compounds with iron form in the Cubic Laves phase. They are strongly magnetic at room temperature, exhibiting large magnetostriction and magnetic anisotropy. The magnetostriction is also very anisotropic[8]. For example, $TbFe_2$ has an easy magnetization direction parallel to [111] and develops zero temperature strains of 4×10^{-3}, while $DyFe_2$ whose easy magnetization direction is [100] has strains of 6×10^{-5} at 4.2^0K[53]. The two environments are identical thus it is taken as a fact that $\lambda_{111} > \lambda_{100}$. For cubic crystals this is quite unusual. The elastic constants show negligible anisotropy[12], yet if the magnetoelastic coupling energies were the same the ratio of the strain for $TbFe_2$ and $DyFe_2$ would be 1. To explain these results a theory for the spontaneous distortions of the atoms in the Laves phase lattice due to coupling of the crystalline electrostatic fields with the total angular momentum of the 4f electron was proposed[11]. This coupling gives rise to an internal distortion of the rare-

earth sublattice which in turn is coupled to an extraordinary contribution to the external strain. A model Hamiltonian was developed to incorporate the energy of this mode and its interaction with acoustic vibrations and magnetization fluctuations[13].

For this Cubic Laves phase structure there are 18 normal modes of motion. The first mode, a triply degenerate mode, is the translation of the lattice as a whole, or the acoustic mode. The next mode consists of two-rare earth atoms in the unit cell moving in opposite directions, while the iron atoms remain stationary. This mode is triply degenerate. The next six modes are a pair of triply degenerate solutions where the rare-earth center of mass moves relative to the four iron atoms while iron atoms undergo rhombohedral distortions. The last six modes involve only the iron atoms. One is a rotation of the iron about each axis and this is triply degenerate. The next is doubly degenerate and consists of a tetrahedral distortion of the iron atoms. The final one is a breathing mode of the iron tetrahedra. Table 1 summarizes the lattice modes. The order in the table reflects the relative magnitude of the motion.

Using a point charge crystal field calculation[12] it has been shown that the rare-earth optic mode couples to the lattice acoustic mode. All the other modes involve the displacements of the Fe atoms. However the equilibrium positions of the Fe are centers of inversion for the diamond structure. Therefore

Description	Degeneracy
lattice acoustic	3
rare-earth optic	3
rare-earth opposing Fe, mixed with Fe rhombohedral distortions	3
Fe rotational shear	3
Fe tetrahedral shear	2
Fe rhombohedral distortions, mixed with rare-earth opposing Fe	3
Fe breathing	1

Table 1: Lattice modes for the Cubic Laves phase structure RE-Fe_2.

these displacements change sign under inversion. The nonzero matrix elements connecting the 4f electron orbits must have even powers of the angular momentum operators. Thus the product of angular momentum and any of these modes changes sign under inversion and there is no coupling. In fact it is shown that the internal mode couples only to the off-diagonal elements of the external strain. This is a property of the Cubic Laves phase. The authors also gave an estimate for the frequency of this internal optic mode that would explain the experimental ratio of λ_{111} and λ_{100}.

In reference[13] harmonic lattice phonon calculations for wave vector q=0 and small q permit the mode couplings and energies to be written in terms of the force constants. These results confirm that the only mode coupling with the length change produced by the external magnetic field is the rare-earth optic mode.

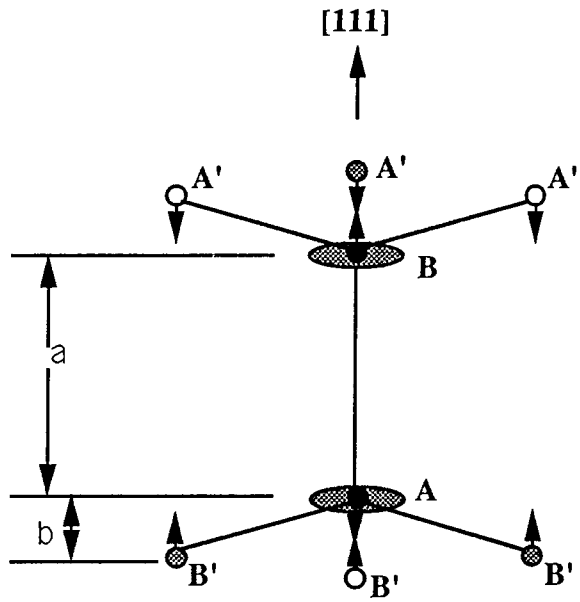

Figure 11: Distortion along the [111] in $Tb_{.28}Dy_{.72}Fe_2$.

Physically, the way a spontaneous distortion occurs is as follows. Consider the case where the magnetic moment is parallel to the [111] direction. The shape of the charge density for 4f electrons takes on various shapes due to strong spin-orbit coupling. For Tb, for example, this is oblate (looks like a pancake) lying perpendicular to the [111] direction. This is shown in figure 11 for the atoms labelled **A** and **B**. Only the rare-earth atoms are displayed. The open circles indicate atoms above the plane of the paper, gray circles are atoms below the plane and black circles are in the plane of the paper.

The charge cloud of atom **A** comes closer to the three atoms **B′** than to the neighbor at **B**. The net Coulomb attraction between **A** and the positive cores of the **B′** atoms causes the **A** atom to move towards **B′** atoms. A similar scenario

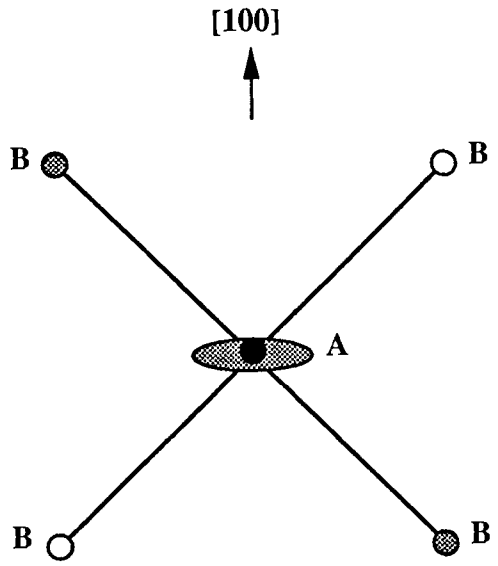

Figure 12: Zero distortion in the [100] direction in $Tb_{.28}Dy_{.72}Fe_2$.

occurs for the **B** atom. The net effect is that the **A** and **B** atom move away from each other. Therefore the a length increases. The change in length a is twice the change in length b.

In the [100] direction, the charge cloud of **A** is equidistant from all its neighbors. Therefore there is no internal distortion due to point charge electrostatic interactions. The **A**-**B** bonds are all equivalent and the potentially large λ_{100} does not appear. This is depicted in figure 12.

The presence of the internal distortions has not been verified. EXAFS seems to be suited to verify directly the validity of such a model. RE-RE, RE-Fe and Fe-Fe bond lengths in principle can be extracted from EXAFS data.

4 EXAFS of Terfenol-D

4.1 Experimental Aspects

4.1.1 Sample Preparation

A rod of Terfenol-D, 6mm diameter and 25mm long was obtained from Edge Technologies. The growth direction was $\langle 112 \rangle$ which is along the rod axis. The crystal was not a pure single crystal but was a series of twinned dendrites, the length of the dendrites being along the growth direction. The width of each dendrite was approximately 1mm. The twinning plane of the dendrites was in the (111) plane[56]. The dendrites could be seen by direct observation. It has been reported that an excess of rare-earth is found between the dendrites[56]. Three rectangular samples were cut from this rod using a spark cutter. Laue diffraction was used to orient the $\langle 111 \rangle$ direction and the $\langle 110 \rangle$ direction both of which are perpendicular to the $\langle 112 \rangle$. Two samples with these orientations where cut. For the third sample the $\langle 110 \rangle$ and $\langle 100 \rangle$ directions were oriented and cut along those planes. The orientation, the sizes of the three crystals and the direction the magnetic field B was applied are shown in figure 13. Alignment in each direction was better than 2.5^0. In order that the sample could be mounted in the gap of the magnet, the samples' widths were never in excess of 6.5mm. The samples were polished with 600 grit silicon carbide paper, then with 6μm and 1μm oil based diamond paste on Rodel polishing pads.

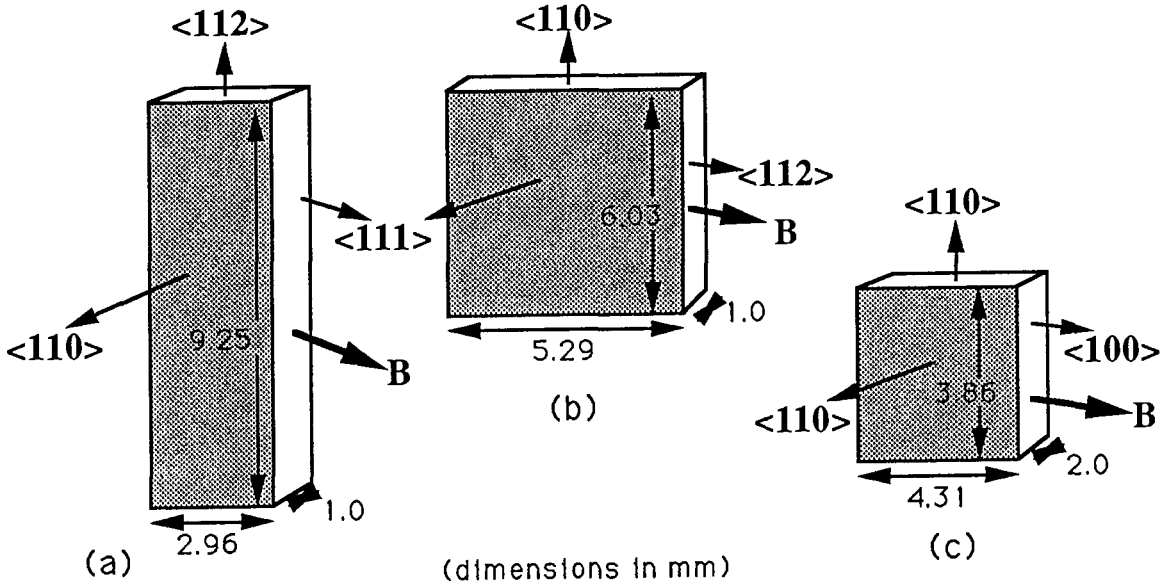

Figure 13: (a) sample#1; (b) sample#2; (c) sample#3.

Afterwards the samples were polished for 30 minutes with Rodel's Colloidal silica on Rodel's Politex pads. To remove any residue after the colloidal silica, they were polished for 10 minutes with distilled water on Politex pads and finally dried with nitrogen. Immediately after the polishing the samples were mounted and loaded in a Surface Auger Microprobe. Auger scans were done to check the cleanliness of the surface. It was found that the surface was contaminated with carbon and oxygen. The contaminants were removed by sputtering at low angle of incidence until they could not be detected by Auger spectroscopy. The samples were then moved to a sputtering system[1] where approximately 200Å of Si_3N_4 were sputtered on the surface to protect the Terfenol-D from oxidizing.

[1]The sputtering system, a Corona Vacuum Coaters model was graciously lent by Dr. M. Parameswaran, Engineering Department, Simon Fraser University

4.1.2 The Detector

The method of detection used in these experiments was total electron yield. The detector and the sample were housed in a plexiglass box 87mm×82mm×8.5mm. The width was constrained to this value or smaller to fit in the gap between the pole pieces of the magnet. The entire outer surface of the box was sputtered with aluminium to a thickness of several microns. The central interior of the box had a circular cross section. Wall thickness in this area was 1mm or less. At either end of the cavity a rectangular opening 6.5mm^2 covered with a Kapton window provided the entrance for the synchrotron radiation. The back window was used as an exit window during initial alignment with the sample removed.

The chamber also had two holes that served as the inlet and outlet of the helium gas. Since the electron scattering cross-section of helium is small, provided the distance between the sample surface and the collector anode is less than 1cm, the electrons emitted by the sample can be collected if they traverse helium gas rather than vacuum [57],[58],[59]. The two holes were positioned in such a way as to minimize turbulent flow in the detecting area, that is between the sample and the detector. The circular cross section inside the chamber also aided in maintaining a smooth flow. The method used to determine the best positions of the inlets and outlets involved passing dry ice vapor through the chamber with a given combination of inlet and outlet and to photograph the pat-

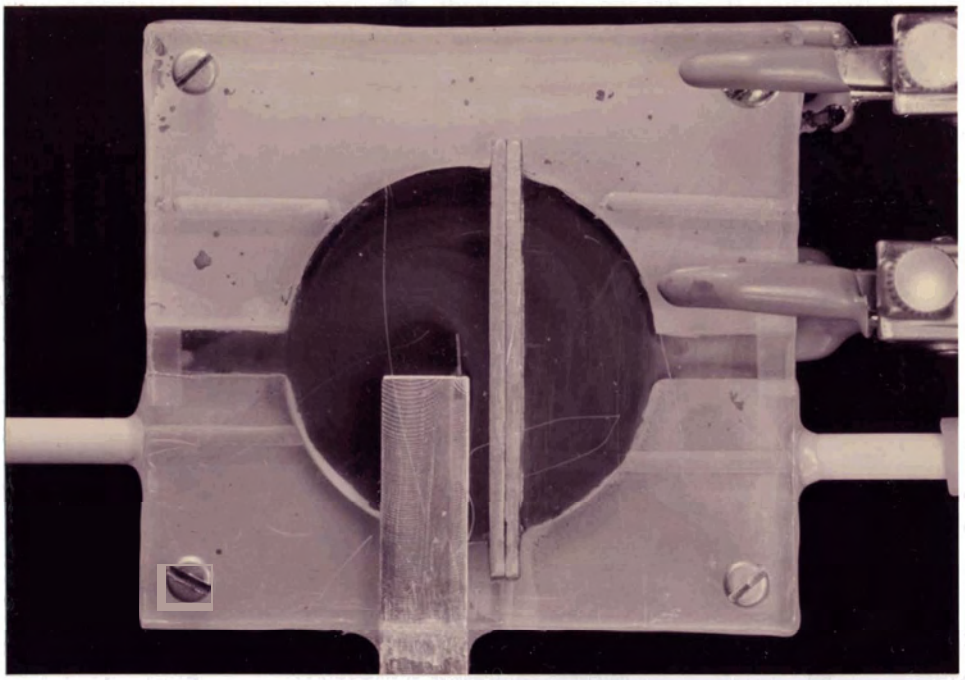

Figure 14: Flow pattern from dry ice vapor observed inside the electron yield chamber.

tern observed (see figure 14). Another hole at the top of the chamber permitted the installation of a thermocouple near the sample to monitor the temperature. A cut away view of the electron yield chamber is shown in figure 15.

The sample holder, a rectangular rod of phenolic plastic, could be inserted from the bottom of the chamber. The sample itself was side mounted with epoxy to a plate attached on the side of the rod. Electrical wires were passed through a small diameter hole drilled along the central axis of the rod. The contact to the sample was mechanically achieved with the aid of a screw, but some electrodag was used as well. A bias of -98V was applied to the sample.

The collector was a piece of aluminized Mylar sandwiched between two pieces of aluminium. The Mylar side was epoxied to one piece of the aluminium frame

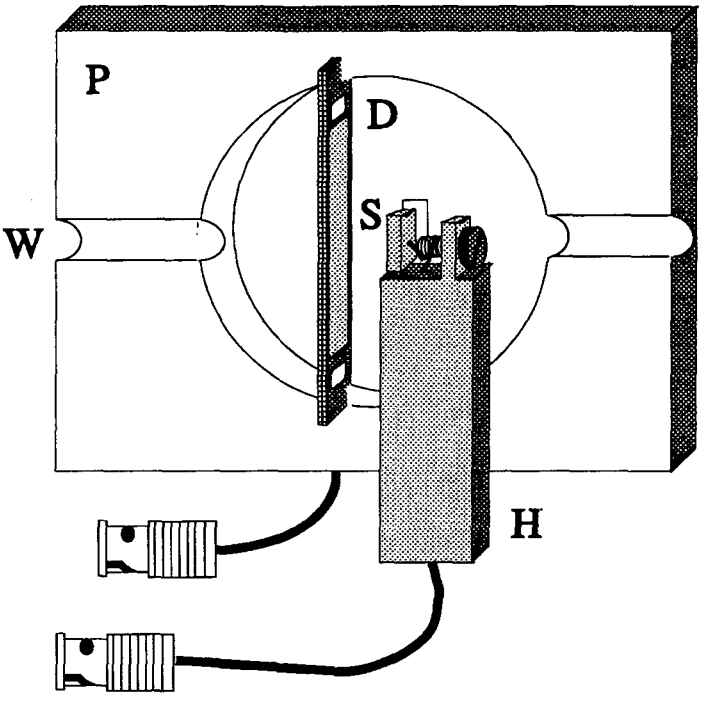

Figure 15: Cut-away-view of the electron yield chamber. P - plexiglass chamber, S - sample, W - Kapton window, D - aluminized Mylar collector, H - sample holder. The inlet and outlet for the Helium flow as well as the thermocouple have been omitted from the figure for clarity.

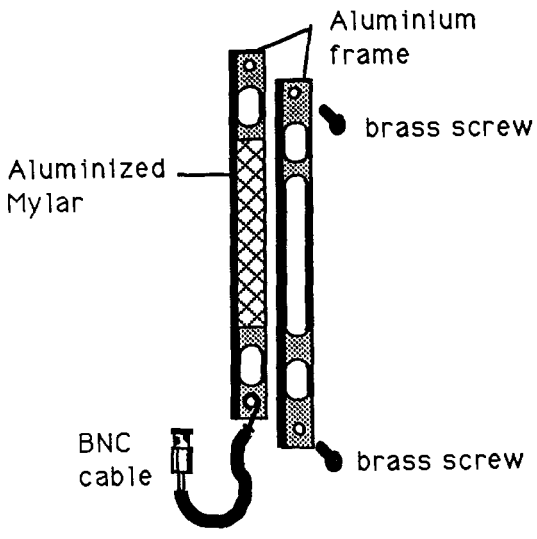

Figure 16: Electron yield collector.

and the aluminium side of the aluminized Mylar made electrical contact with the top piece of the aluminium frame. The frame's main purpose was to provide structural stability hence minimizing the vibrational noise sources. Being a metal it was also part of the detecting surface. Figure 16 shows the details of the collector. The solid angle was limited in one direction because of the constraint of the gap width. In the other direction this was not a problem. As shown the detecting surface is 36.7×6.4mm. There are two holes at either end of the aluminium frame that are left open. The holes in the aluminium frame of the detector simply permitted the helium to flow behind the detector as well as in the front. Note that the distance between the sample and the electron yield detector is less than 5mm.

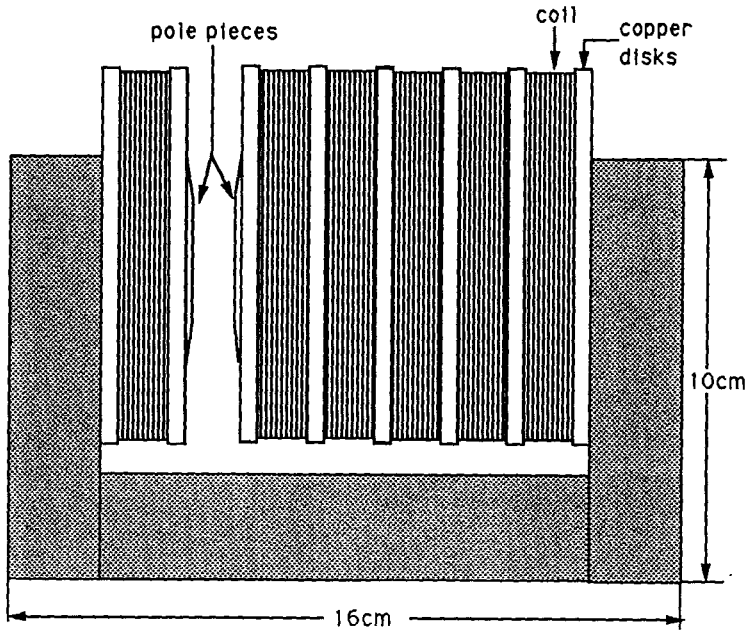

Figure 17: Electromagnet.

4.1.3 The Magnets

To generate the external magnetic field a magnet was built such that it would fit on a side station beamline. The beamline used (beamline IV-1 at SSRL) allowed only 48mm between the wall and the edge of the beam when the sample was approximately centered along the length of the experimental hutch. Two magnets were built and used for these experiments. The first is an electromagnet and is illustrated in figure 17. The yoke, core and pole piece are made of steel. The pole pieces have a 79^0 taper angle. The coils are wound on thin plexiglass bobbins which slip onto the core. Each coil has approximately 1200 turns of 28 AWG copper wire. Each coil is separated by a copper disk 4mm thick whose outer diameter is grooved. A copper tube $\frac{1}{8}''$ OD is soldered into the groove.

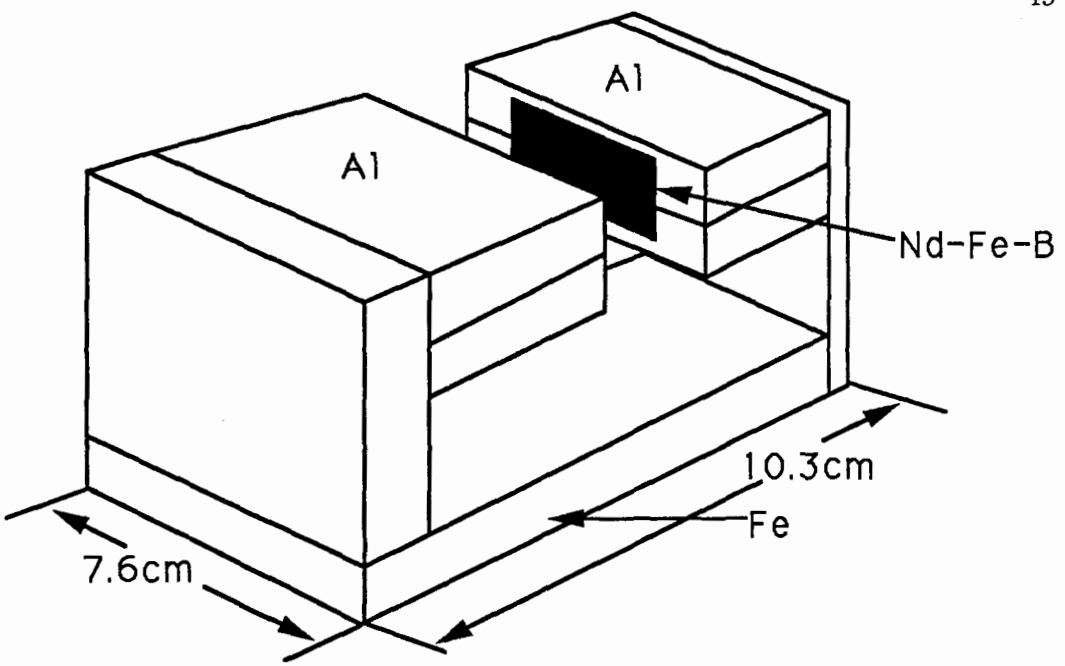

Figure 18: Permanent magnet.

These copper disks provide the cooling mechanism for the magnet to dissipate the Joule heat generated when passing large currents through the copper coils. The magnet was calibrated with a Bell Gaussmeter model number 620. The cooling water was at 11^0C during calibration. To obtain 5kG a current of .56A is required. This was provided by a Xantrex XKW 300-3.5 DC Power Supply.

The second magnet is made with two rectangular pieces of Nd-Fe-B alloy. These pieces are permanent magnets. The two pieces were press fitted in a frame of aluminium and a yoke of steel completed the magnetic path. The whole assembly[2] is shown in figure 18. The gap size could be varied to obtain different magnetic fields. The gap size set at 13.5mm provided 5.8kG at the

[2]The Nd-Fe-B magnets were provided by Peter Boyd (SSRL) who also constructed the magnet.

sample position. The uniformity of the field is not as constant in this magnet as compared with the electromagnet, but over the sample size both magnets provide a uniform field.

4.1.4 EXAFS Experimental Setup

The EXAFS experiments were done at the Stanford Synchrotron Radiation Laboratory (SSRL). During the course of these experiments the energy in the storage ring SPEAR was 3.0GeV. The electron beam was delivered with a current of 100mA and reinjected at about 50mA, or once every 24 hours. The beamline used, beamline IV-1, is a wiggler side station with a double crystal monochromator. For these measurements, the monochromator had Si(111) crystals providing x-ray energies between 3 and 17keV. After the monochromator the beam passed through a Huber slit set at 1mm×3mm. A standard SSRL ionization chamber 152mm long and 58.7mm wide with Kapton windows was used to monitor the incident beam, I_0. The signals of both the electron yield detector and the ionization chamber were detected with Keithley current preamplifiers which in turn were connected to a voltage-to-frequency converter and to a computer. The gain for the ionization chamber was typically 10^7 and for the electron yield detector 10^{10} was the norm. Monochromators operating on the principle governed by Bragg's Law not only diffract x-rays for the desired set of *hkl* planes of the crystal in use but also by all other parallel planes pro-

vided the structure factor is not zero. For Si, a diamond structure, the allowed reflections are governed by the two selection rules: $h + k + l = 4n$ where all indices are even or else all indices are odd. This gives rise to harmonics and consequently the beam is not perfectly monochromatic. To minimize harmonic content and crystal glitches, it was found that the best spectra were obtained when the monochromator was detuned by 25% at 7300eV for the Fe K edge scans, by 50% at 7700eV for the Tb L_{III} edge scans and 50% at 7990eV for the Dy L_{III} edge scans.

Since the crystals are oriented a polarization study could be performed. The coordination number is dependent on the direction of the electric field vector of the radiation with respect to a given crystallographic orientation. For the zero field experiments, the electron yield chamber was mounted on an aluminium block secured to a sample positioner with horizontal and vertical motion for aligning the sample into the beam. The same setup was used when a magnetic field was applied except that the aluminium block was replaced by the magnet. The experimental configuration is illustrated in figure 19. By turning the magnet (or the aluminium block, for zero field) by 90^0 the perpendicular orientation could be probed. Table 2 is a list of the various orientations of the electric field vector and the applied magnetic field for the measurements taken. As well as having two directions for the polarization and two magnetic states

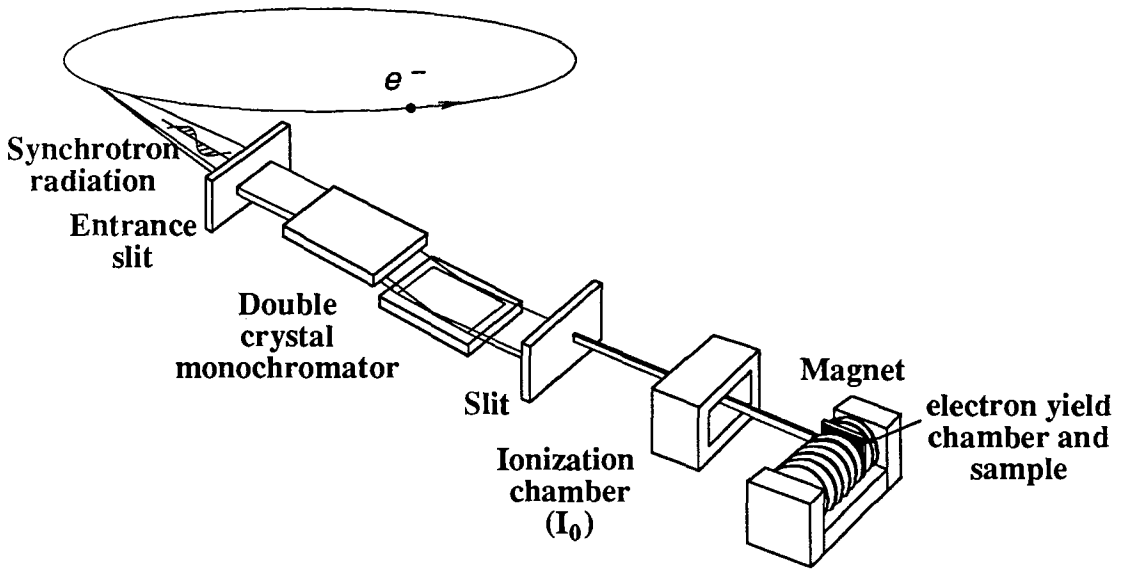

Figure 19: Experimental setup for the measurement of EXAFS by electron-yield detection with an applied magnetic field. The sketch is not to scale. I_0 is an ionization chamber through which nitrogen gas flows.

crystal	$\vec{E}$	$\vec{B}$	
1	[111]	[111]	$\vec{E}_{\parallel}$
	[11$\bar{2}$]	[111]	$\vec{E}_{\perp}$
2	[11$\bar{2}$]	[11$\bar{2}$]	$\vec{E}_{\parallel}$
	[1$\bar{1}$0]	[11$\bar{2}$]	$\vec{E}_{\perp}$
3	[001]	[001]	$\vec{E}_{\parallel}$
	[110]	[001]	$\vec{E}_{\perp}$

Table 2: Orientations investigated for each sample. The crystallographic orientations of the crystals are shown in figure 13.

the temperature of the sample could also be varied above and below the spin reorientation temperature. This was accomplished via the cooling mechanism of the magnet. The magnet was water cooled using a recirculating water cooler. The temperature could be varied between 0^0C and about 50^0C. The temperature inside the chamber was monitored with a chromel-alumel thermocouple referenced to the melting point of ice. In the case of the permanent magnet where no cooling is necessary, two cooling plates similar in design to the cooling disks of the electromagnet were attached to the sample chamber. This assembly could then be placed in the gap of the magnet and have the same control over sample temperature as when the electromagnet was used. The two temperatures the measurements were made at were 15 ± 1^0C and 5 ± 1^0C for each case listed in table 2. For each sample EXAFS data were taken at the Fe K edge at 7112eV, the Tb L_{III} edge at 7515eV and the Dy L_{III} edge at 7990eV.

4.2 Data Analysis and Results

4.2.1 Fe K edge results

Typically five scans (I_e/I_0) were averaged together for each set of conditions. The background removal procedure was done as described previously in section 2.2. The edge energy was defined as the first inflection point. The background polynomial used was of 6^{th} order except for sample#1 where it was a 7^{th} order. The range of the data was 1.875 to 9.90Å^{-1}. The EXAFS interference function

for the three samples at the Fe K edge are shown in figure 20, 21, 22. Each plot has two curves, one taken at $B = 0$ and the other at B_{max}.

The range is limited by the onset of the Tb L_{III} edge at 7515eV. The Fourier transforms corresponding to the data shown above, taken at the Fe K edge for each sample, are shown in figures 23, 24 and 25. Differences in radial distances R are very small. The first two shells are between .96Å and 3.3Å, which include the main peak and the smaller peak on the right shoulder. FEFF 5.04 was used to simulate the expected spectrum for Terfenol-D. The Fourier transform of $k\chi(k)$ is shown in figure 26. In increasing distance the peaks in the FEFF simulations correspond to a Fe-Fe distance, a Fe-Dy distance, a Fe-Fe distance and a Fe-Dy distance. The Debye-Waller factor calculated by FEFF are .00508 and .00432 for the first and second shell respectively. For the first shell, Fe-Fe, σ_1^2 is the same as calculated for bulk Fe[60].

Since this is a two shell problem with the backscattering atoms differing from the absorbing atom, curve fitting is the most appropriate method of extracting physical parameters. In this problem the differences of parameters between two states is of primary interest. To fit the data while minimizing the correlation between parameters, a reference state was chosen: the sample temperature is below the spin reorientation temperature $T_s = 10^0$C, no magnetic field is applied and the electric field vector is parallel to one of the crystallographic directions

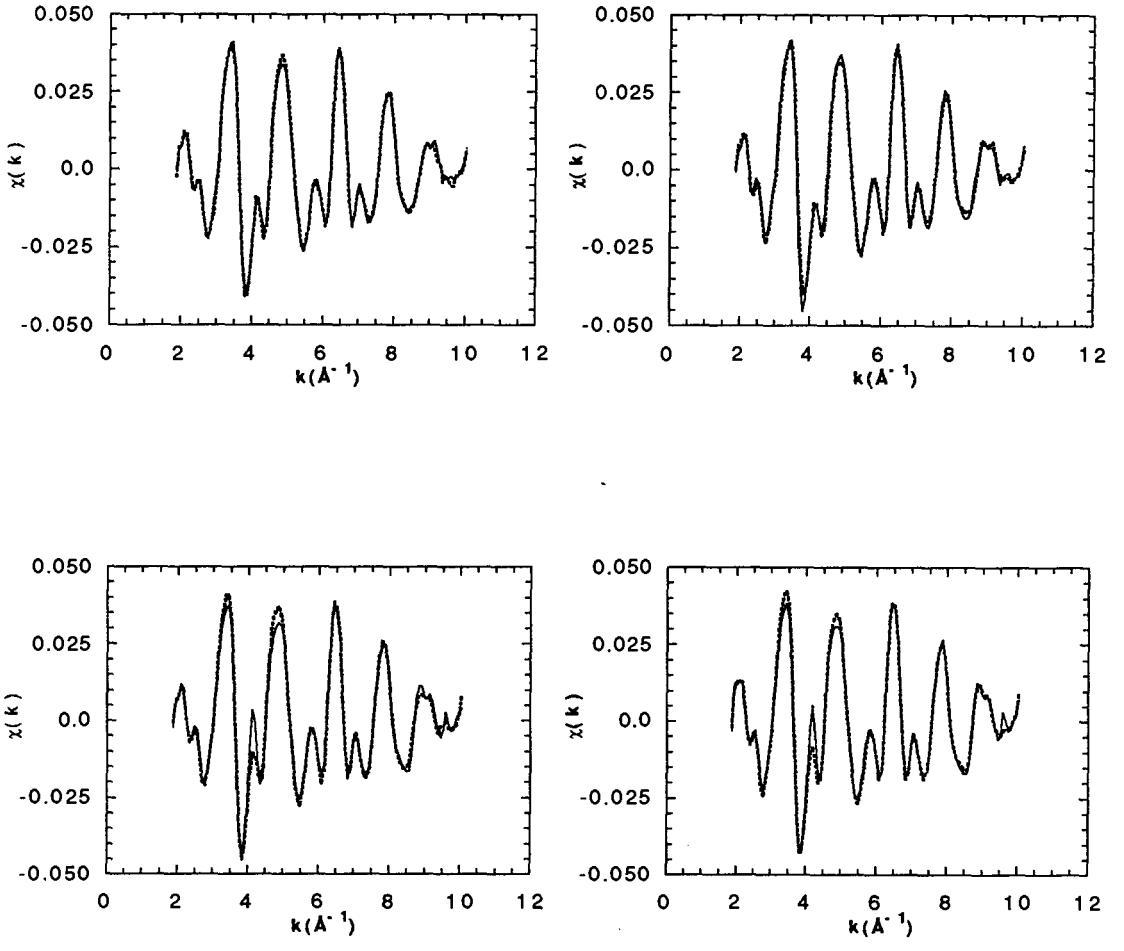

Figure 20: XAFS $\chi(k)$ of the Fe K edge in Terfenol-D. Range of the data: 1.875–9.90Å^{-1}. The solid line is for $B = 0$ and the dashed line is for $B = 5$kG applied along the $\langle 111 \rangle$ (sample#1). Top left: $\mathbf{E}\langle 111 \rangle$, $T > 10^0$C; Top right: $\mathbf{E}\langle 111 \rangle$, $T < 10^0$C; Bottom left: $\mathbf{E}\langle 112 \rangle$, $T > 10^0$C; Bottom right: $\mathbf{E}\langle 112 \rangle$, $T < 10^0$C

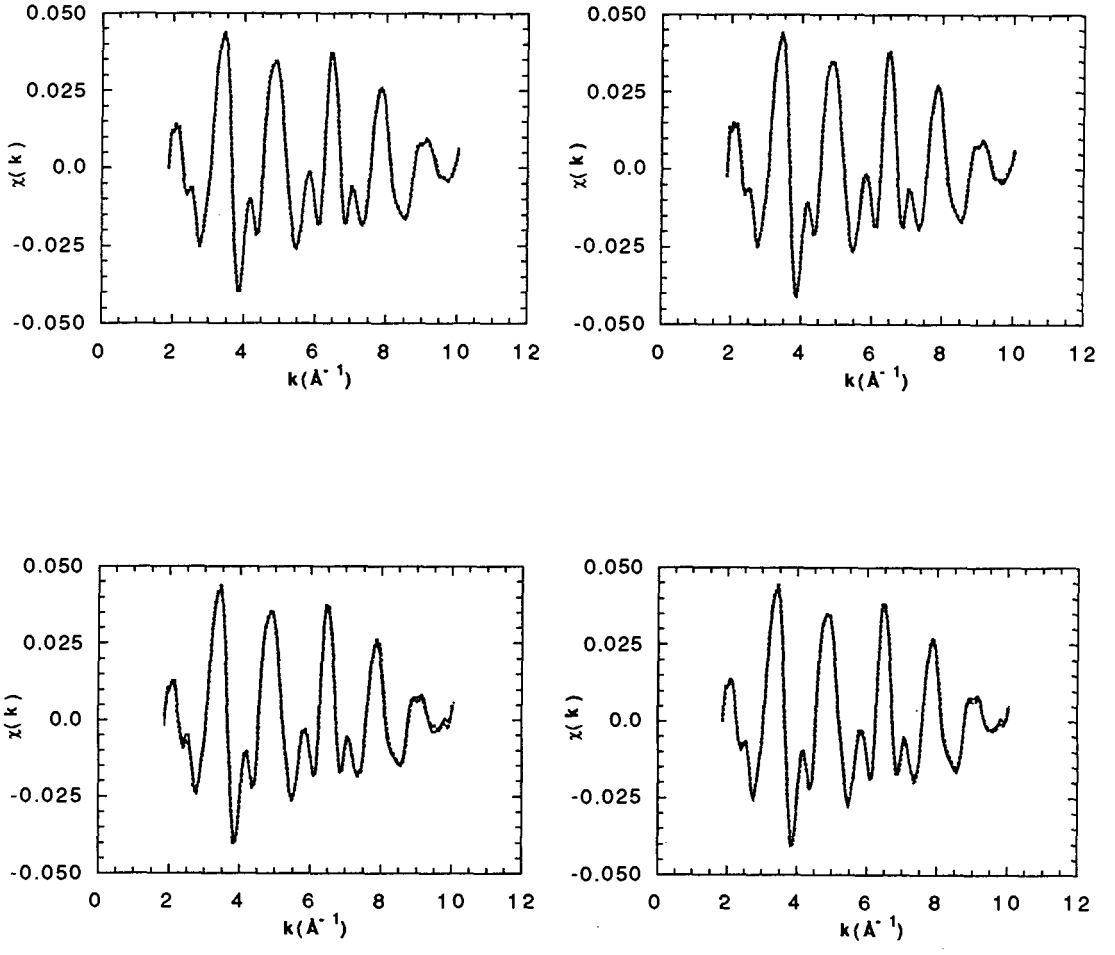

Figure 21: XAFS $\chi(k)$ of the Fe K edge in Terfenol-D. Range of the data: 1.875–9.90Å^{-1}. The solid line is for $B = 0$ and the dashed line is for $B = 5$kG applied along the $\langle 112 \rangle$ (sample#2). Top left: $\mathbf{E}\langle 112 \rangle$, $T > 10^0$C; Top right: $\mathbf{E}\langle 112 \rangle$, $T < 10^0$C; Bottom left: $\mathbf{E}\langle 110 \rangle$, $T > 10^0$C; Bottom right: $\mathbf{E}\langle 110 \rangle$, $T < 10^0$C.

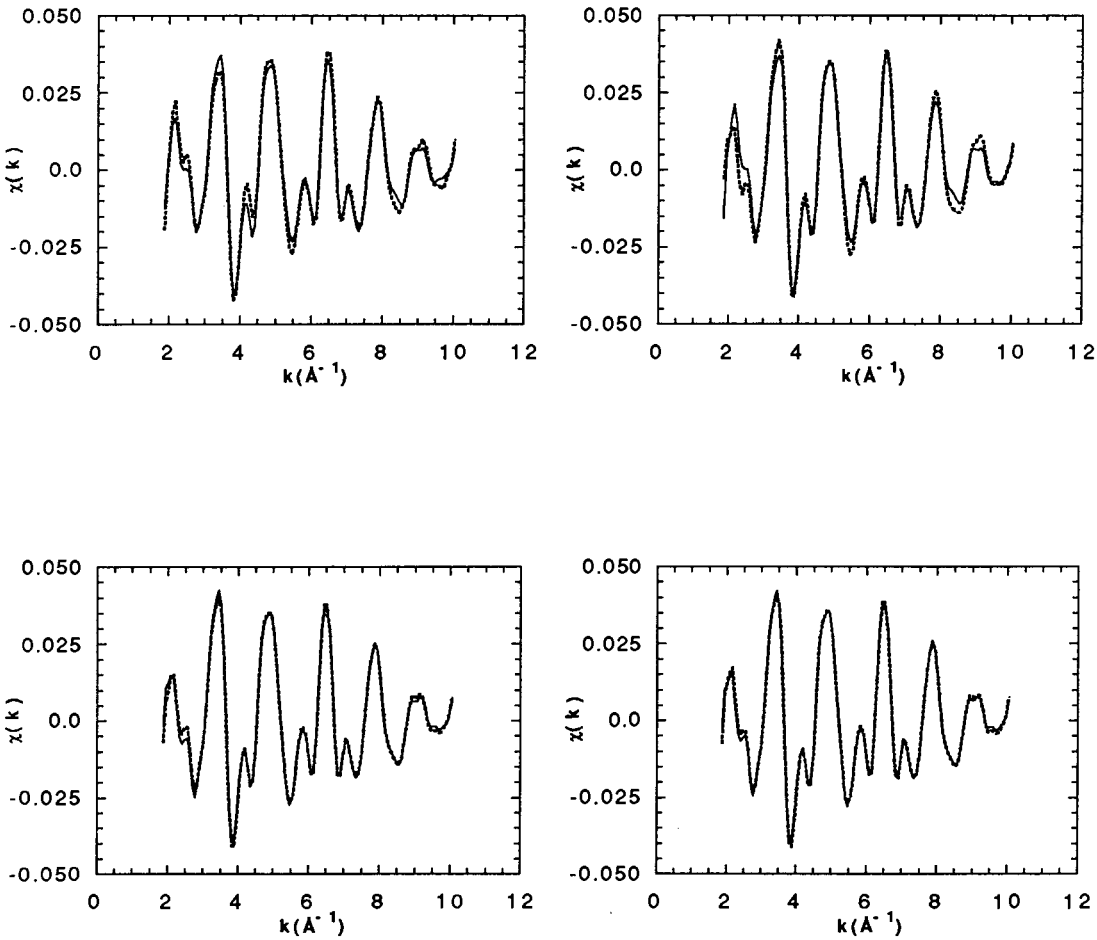

Figure 22: XAFS $\chi(k)$ of the Fe K edge in Terfenol-D. Range of the data: 1.875–9.90Å^{-1}. The solid line is for $B = 0$ and the dashed line is for $B = 5.8$kG applied along the $\langle 100 \rangle$ (sample#3). Top left: $\mathbf{E}\langle 110 \rangle$, $T > 10^0$C; Top right: $\mathbf{E}\langle 110 \rangle$, $T < 10^0$C; Bottom left: $\mathbf{E}\langle 100 \rangle$, $T > 10^0$C; Bottom right: $\mathbf{E}\langle 100 \rangle$, $T < 10^0$C.

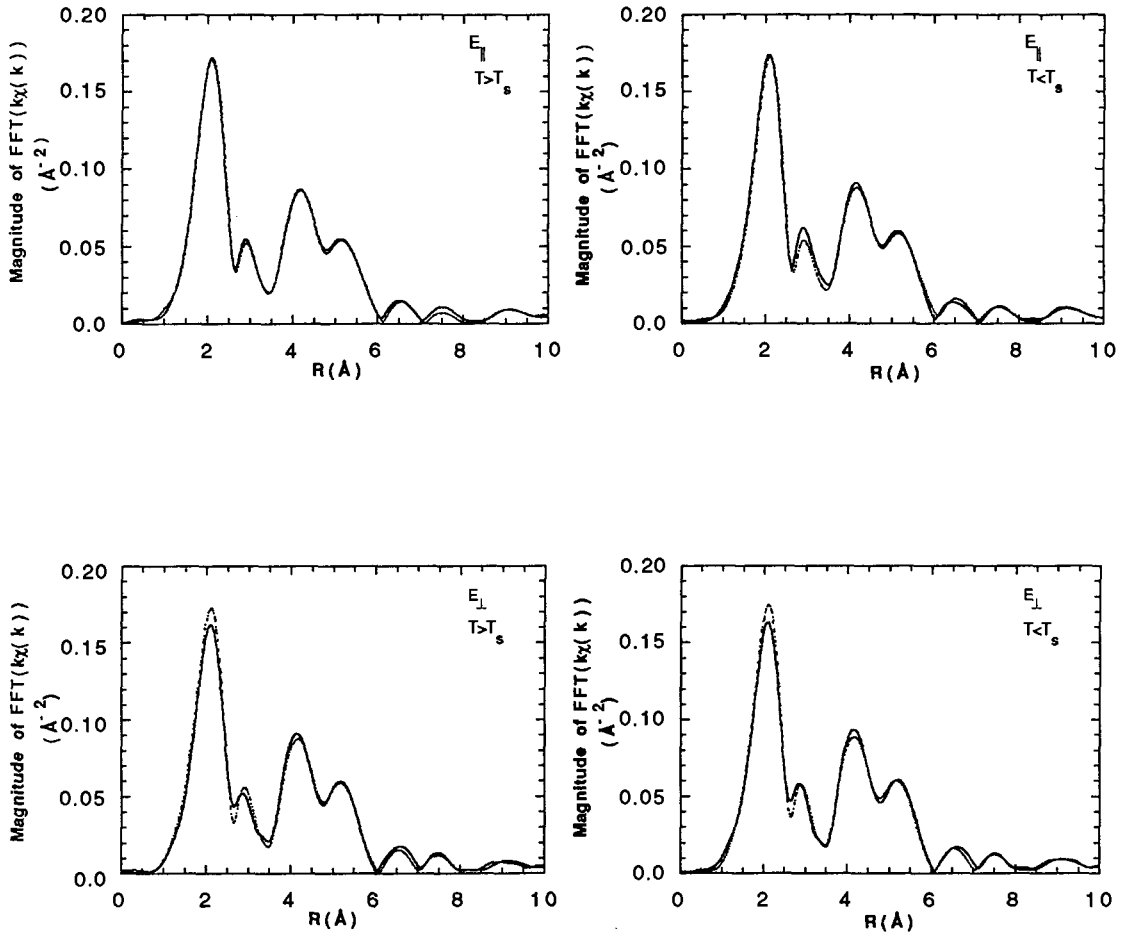

Figure 23: Fourier transform of XAFS $k\chi(k)$ of the Fe K edge in Terfenol-D. Range used for $k\chi(k)$ transform is 1.88Å^{-1} to 9.88Å^{-1} with a 10% Gaussian window. The solid line is for $B = 0$ and the dashed line is for $B = 5$kG applied along the $\langle 111 \rangle$ (sample#1). Top left: $\mathbf{E}\langle 111 \rangle$, $T > 10^0$C; Top right: $\mathbf{E}\langle 111 \rangle$, $T < 10^0$C; Bottom left: $\mathbf{E}\langle 112 \rangle$, $T > 10^0$C; Bottom right: $\mathbf{E}\langle 112 \rangle$, $T < 10^0$C.

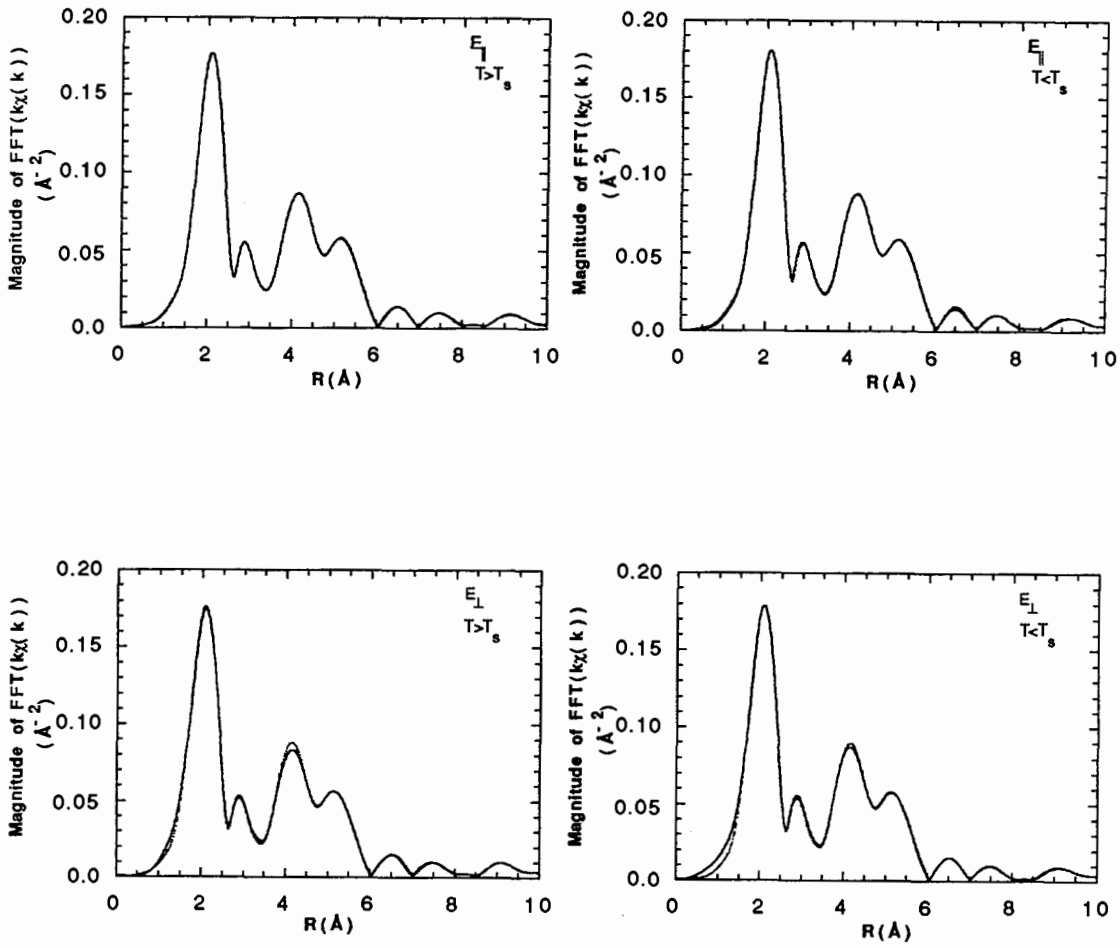

Figure 24: Fourier transform of XAFS $k\chi(k)$ of the Fe K edge in Terfenol-D. Range used for $k\chi(k)$ transform is 1.88Å^{-1} to 9.90Å^{-1} with a 10% Gaussian window. The solid line is for $B = 0$ and the dashed line is for $B = 5$kG applied along the $\langle 112 \rangle$ (sample#2). Top left: $\mathbf{E}\langle 112 \rangle$, $T > 10^0$C; Top right: $\mathbf{E}\langle 112 \rangle$, $T < 10^0$C; Bottom left: $\mathbf{E}\langle 110 \rangle$, $T > 10^0$C; Bottom right: $\mathbf{E}\langle 110 \rangle$, $T < 10^0$C.

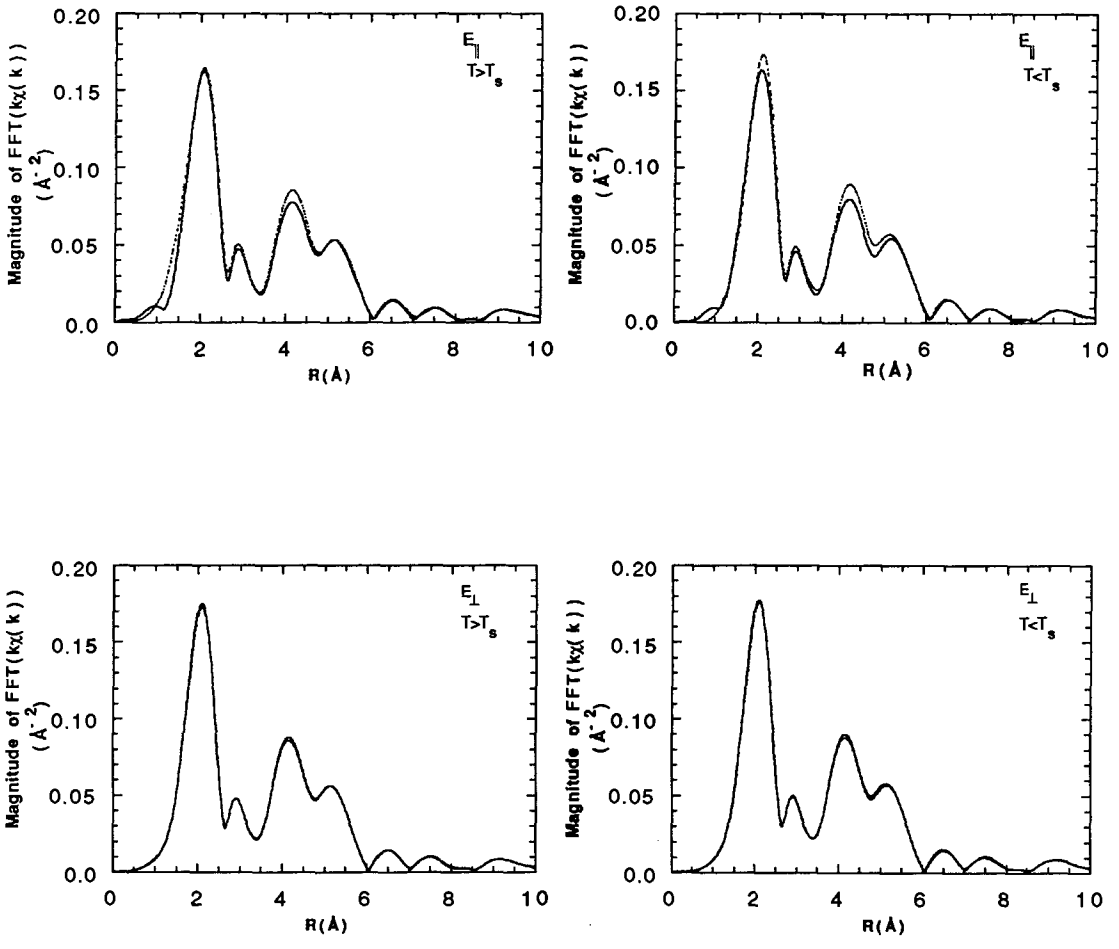

Figure 25: Fourier transform of XAFS $k\chi(k)$ of the Fe K edge in Terfenol-D. Range used for $k\chi(k)$ transform is 1.95Å^{-1} to 9.90Å^{-1} with a 10% Gaussian window. The solid line is for $B = 0$ and the dashed line is for $B = 5.8$kG applied along the $\langle 100 \rangle$ (sample#3). Top left: $\mathbf{E}\langle 110 \rangle$, $T > 10^0$C; Top right: $\mathbf{E}\langle 110 \rangle$, $T < 10^0$C; Bottom left: $\mathbf{E}\langle 100 \rangle$, $T > 10^0$C; Bottom right: $\mathbf{E}\langle 100 \rangle$, $T < 10^0$C.

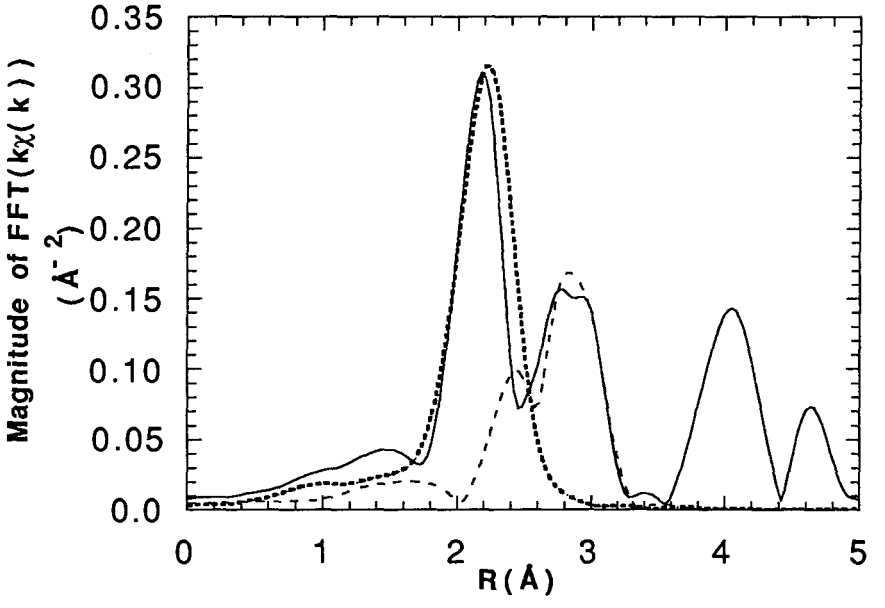

Figure 26: Fourier transform of XAFS $k\chi(k)$ of the Fe K edge in Terfenol-D generated with FEFF 5.04. Range used for $k\chi(k)$ transform is .05Å^{-1} to 20Å^{-1}. The solid line is for the sum of the first 4 shells, the short dashes are the first shell only and the long dashes are the second shell only.

of the sample. Reference in this case means that the structure is assumed to be perfectly cubic, therefore the distances for first and second shells are fixed to calculated values based on the lattice parameter given by x-ray diffraction measurements[14]. The lattice constant, as determined by x-ray diffraction is 7.32Å. The nearest neighbor, Fe atoms, are at 2.588Å and the second nearest neighbors, rare-earth atoms, are at 3.035Å. The coordination numbers are also fixed taking into account the orientation of the electric field vector with respect to the crystallographic orientation of the crystal. The effective coordination number is given by equation 3,

$$N_{eff} = 3\sum_{i=1}^{N} \cos^2 \theta_i \tag{51}$$

where θ is the angle between $\vec{\mathbf{E}}$ and $\vec{R}_i$. Note that there is some error in the coordination number because of misalignment occurring during the polishing and also from the sample mount itself. The misalignment could be 2 to 4 degrees which, depending on the sample, could change N_{eff} by as much as 20%. But the data were acquired in such a way that the misalignment was constant for a given sample. The distortion of the unit cell is expected to be small with the effect on the coordination number being negligible therefore the N's can be considered as constants in this problem. Fixing the coordination number this way, avoids the problem of the correlation between N's and σ^2's. These assumptions permit a 2 shell fit with 3 fitting parameters per shell, E_{0_j}, σ_j^2 and a_j for the reference

case. For all subsequent cases it was assumed that the E_{0_j}, a_j and the N_j would remain constant. The fits to the unknowns then involve 2 variables per shell, the radial distance R_j and the Debye-Waller factor, σ_j^2. The amplitude and phase used in the fits were generated using FEFF 5.04[50](see figure 27). The Debye-Waller factors are not included in the amplitude term, therefore the values found from curve fitting are absolute values. The mean free path term could have been considered as another variable in the fitting procedure, but the calculated values by FEFF were deemed to be a good estimate and it was included in the amplitude term. The S_0^2 term was set at .74.

Results of the curve fitting are tabulated in the tables that follow. The first row is always the reference. It has the crystallographic values for R_1 and R_2. The goodness of fit χ^2 is calculated according to equation 35. An example of the quality of the fits obtained is shown in figure 28. The error bars quoted in the tables are calculated from $2\chi^2_{min}$ for the parameter of interest with the remaining parameters fixed at the best fit value. Tables 3, 4 and 5 are the results for data taken at the Fe K edge for sample #1, #2 and #3 respectively.

Note that when the calculated coordination numbers for the $\langle 110 \rangle$ direction were used, one of the σ^2 was always negative, an unrealistic value. For this orientation, the polycrystalline coordination numbers were used. It is not understood why this was required since Laue diffraction clearly shows a single

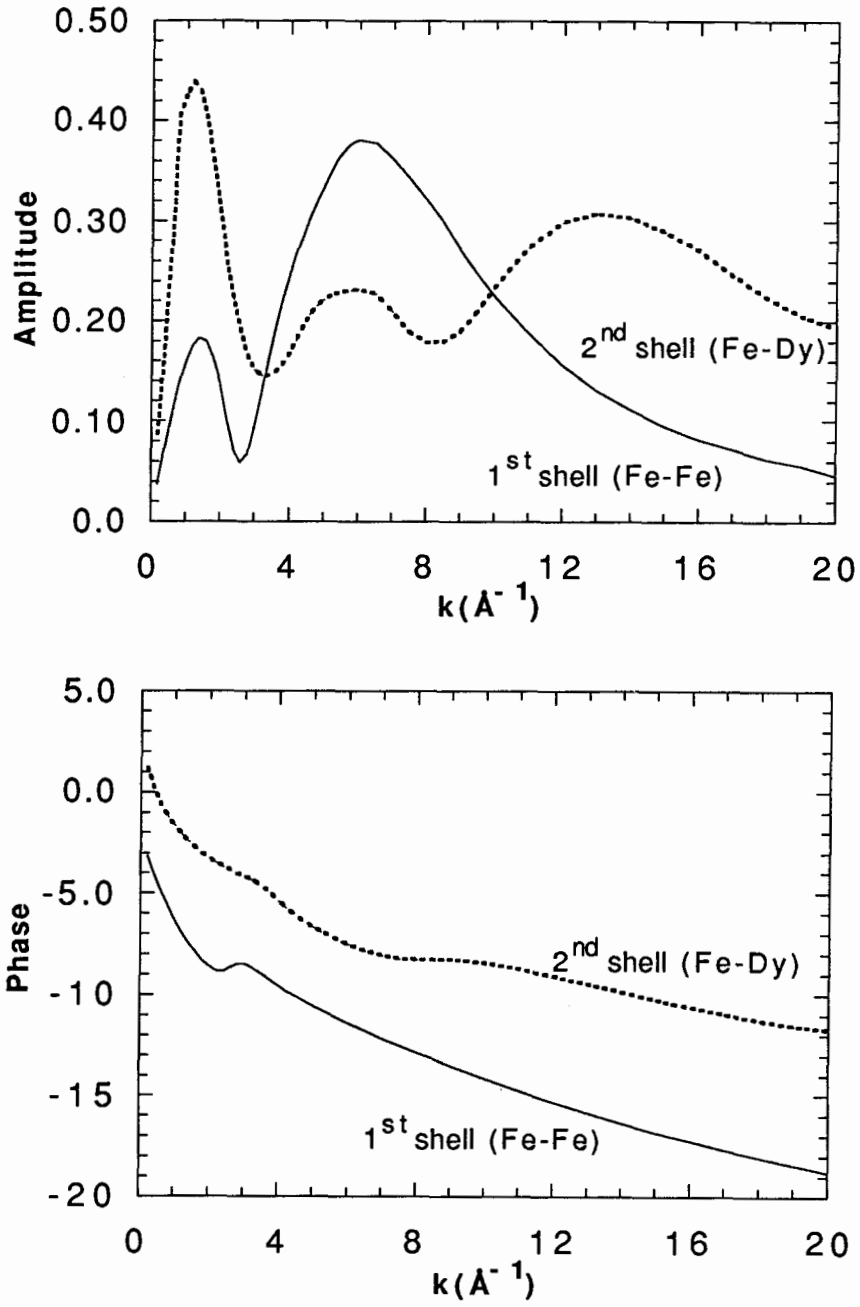

Figure 27: Amplitude and phase for Terfenol-D generated by FEFF 5.04. Top: amplitude. Bottom: phase.

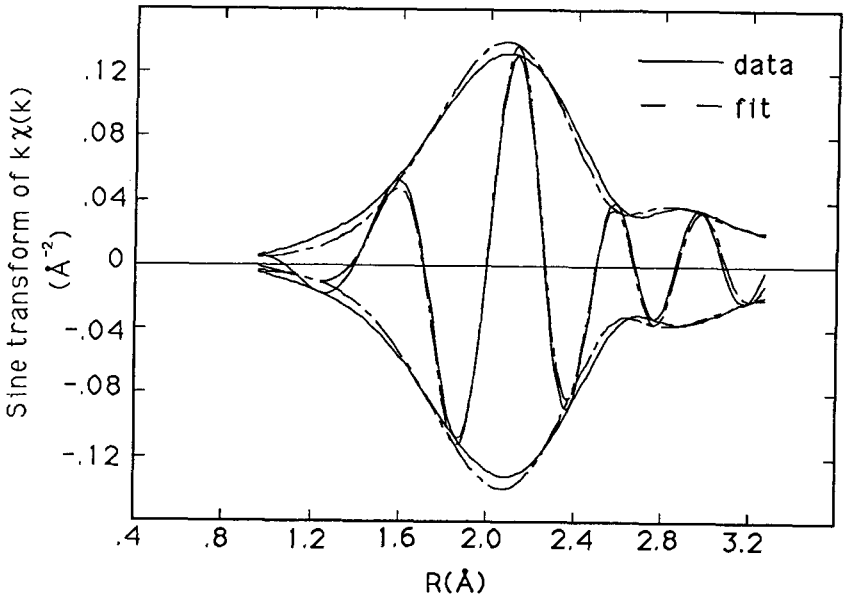

Figure 28: Curve fitting results for Fe K edge data for Terfenol-D. Fourier transform of $k\chi(k)$ with a Hamming window applied over the range 1.88Å^{-1} to 9.90Å^{-1}; Fit range .96Å to 3.27Å. The sine transform is enveloped by the magnitude of the complex transform. The data is represented by the solid lines and the fits by the dashed lines.

Sample#1 Fe K edge		R_1(Å)	R_2(Å)	σ_1^2 $\times 10^{-3}$	σ_2^2 $\times 10^{-3}$	χ^2 $\times 10^{-4}$
$\mathbf{E}_{\parallel}$	$\mathbf{E}\langle 111\rangle$ $T < 10^0$C,$B = 0$	2.588	3.034	2.59	12.90	.97
	$\mathbf{E}\langle 111\rangle$ $T < 10^0$C,5kG	2.589 $\pm.009$	3.036 $\pm.025$	2.92 $^{+1.54}_{-1.36}$	14.64 $^{+5.32}_{-3.83}$	.68
	$\mathbf{E}\langle 111\rangle$ $T > 10^0$C,$B = 0$	2.588 $\pm.008$	3.039 $\pm.021$	2.95 $^{+1.28}_{-1.15}$	14.24 $^{+4.18}_{-3.20}$	.47
	$\mathbf{E}\langle 111\rangle$ $T > 10^0$C,5kG	2.588 $\pm.008$	3.036 $\pm.022$	3.02 $^{+1.27}_{-1.14}$	15.22 $^{+4.45}_{-3.36}$	.46
$\mathbf{E}_{\perp}$	$\mathbf{E}\langle 112\rangle$ $T < 10^0$C,$B = 0$	2.592 $\pm.007$	3.063 $\pm.016$	5.84 $^{+1.19}_{-1.08}$	9.80 $^{+3.07}_{-2.48}$	.39
	$\mathbf{E}\langle 112\rangle$ $T < 10^0$C,5kG	2.591 $\pm.006$	3.051 $\pm.016$	5.33 $^{+1.06}_{-0.98}$	10.31 $^{+2.96}_{-2.40}$	.34
	$\mathbf{E}\langle 112\rangle$ $T > 10^0$C,$B = 0$	2.597 $\pm.007$	3.065 $\pm.016$	6.06 $^{+1.12}_{-1.02}$	10.56 $^{+3.00}_{-2.43}$	.33
	$\mathbf{E}\langle 112\rangle$ $T > 10^0$C,5kG	2.589 $\pm.007$	3.046 $\pm.017$	5.52 $^{+1.15}_{-1.05}$	10.57 $^{+3.23}_{-2.58}$	.39

Table 3: Fit results of Fe K edge data of sample#1. The range of the data for a $k\chi(k)$ Fourier transform was 1.88 to 9.90Å^{-1} with a Hamming window. The range for the R-space fits was .96-3.27Å. Fixed parameters $N_1\langle 111\rangle = 3.99$, $N_2\langle 111\rangle = 7.83$, $N_1\langle 112\rangle = 4.998$, $N_2\langle 112\rangle = 6.9$ $\Delta E_1 = -.445$eV, $\Delta E_2 = -2.839$eV, $a_1 = -1.048$, $a_2 = -1.108$.

Sample#2 Fe K edge		R_1(Å)	R_2(Å)	σ_1^2 $\times 10^{-3}$	σ_2^2 $\times 10^{-3}$	χ^2 $\times 10^{-4}$
$\mathbf{E}_\parallel$	$\mathbf{E}\langle 112\rangle$ $T < 10^0$C,$B = 0$	2.588	3.034	4.77	7.99	.11
	$\mathbf{E}\langle 112\rangle$ $T < 10^0$C,5kG	2.588 $\pm.004$	3.034 $\pm.008$	4.83 $^{+0.62}_{-0.59}$	8.22 $^{+1.43}_{-1.28}$	.13
	$\mathbf{E}\langle 112\rangle$ $T > 10^0$C,$B = 0$	2.589 $\pm.003$	3.036 $\pm.007$	5.04 $^{+0.56}_{-0.53}$	8.24 $^{+1.27}_{-1.16}$	.10
	$\mathbf{E}\langle 112\rangle$ $T > 10^0$C,5kG	2.590 $\pm.003$	3.037 $\pm.007$	5.08 $^{+0.54}_{-0.52}$	8.29 $^{+1.25}_{-1.13}$	.10
$\mathbf{E}_\perp$	$\mathbf{E}\langle 110\rangle$ $T < 10^0$C,$B = 0$	2.594 $\pm.006$	3.046 $\pm.012$	7.17 $^{+1.05}_{-0.96}$	5.07 $^{+2.18}_{-1.85}$	.35
	$\mathbf{E}\langle 110\rangle$ $T < 10^0$C,5kG	2.592 $\pm.004$	3.044 $\pm.009$	7.30 $^{+0.76}_{-0.71}$	5.28 $^{+1.57}_{-1.39}$	.19
	$\mathbf{E}\langle 110\rangle$ $T > 10^0$C,$B = 0$	2.593 $\pm.005$	3.047 $\pm.010$	7.52 $^{+0.79}_{-0.74}$	5.80 $^{+1.68}_{-1.48}$	.19
	$\mathbf{E}\langle 110\rangle$ $T > 10^0$C,5kG	2.583 $\pm.005$	3.045 $\pm.010$	7.43 $^{+0.83}_{-0.78}$	5.50 $^{+1.73}_{-1.52}$	.21

Table 4: Fit results for Fe K edge data of sample#2. The range of the data for a $k\chi(k)$ Fourier transform is 1.88 to 9.90Å^{-1} with a Hamming window. The range for the R-space fits was .96-3.27Å. Fixed parameters $N_1\langle 112\rangle = 4.998$, $N_2\langle 112\rangle = 6.9$, $N_1\langle 110\rangle = 6.0$, $N_2\langle 110\rangle = 6.0$ $\Delta E_1 = 3.757$eV, $\Delta E_2 = -2.132$eV, $a_1 = -.688$, $a_2 = -.997$.

Sample#3 Fe K edge		R_1(Å)	R_2(Å)	σ_1^2 $\times 10^{-3}$	σ_2^2 $\times 10^{-3}$	χ^2 $\times 10^{-4}$
$\mathbf{E}_{\parallel}$	$\mathbf{E}\langle 100\rangle$ $T < 10^0$C,$B = 0$	2.588	3.034	7.89	7.45	.24
	$\mathbf{E}\langle 100\rangle$ $T < 10^0$C,5.8kG	2.592 $\pm.004$	3.035 $\pm.009$	7.18 $^{+0.67}_{-0.64}$	6.50 $^{+1.55}_{-1.37}$	.15
	$\mathbf{E}\langle 100\rangle$ $T > 10^0$C,$B = 0$	2.592 $\pm.005$	3.037 $\pm.010$	7.84 $^{+0.80}_{-0.75}$	6.66 $^{+1.79}_{-1.55}$	.19
	$\mathbf{E}\langle 100\rangle$ $T > 10^0$C,5.8kG	2.596 $\pm.008$	3.040 $\pm.017$	7.26 $^{+1.41}_{-1.26}$	5.79 $^{+3.15}_{-2.48}$	.61
$\mathbf{E}_{\perp}$	$\mathbf{E}\langle 110\rangle$ $T < 10^0$C,$B = 0$	2.591 $\pm.004$	3.035 $\pm.010$	6.98 $^{+0.72}_{-0.68}$	6.40 $^{+1.69}_{-1.48}$	.18
	$\mathbf{E}\langle 110\rangle$ $T < 10^0$C,5.8kG	2.591 $\pm.004$	3.035 $\pm.009$	7.04 $^{+0.66}_{-0.62}$	6.37 $^{+1.52}_{-1.35}$	.15
	$\mathbf{E}\langle 110\rangle$ $T > 10^0$C,$B = 0$	2.591 $\pm.005$	3.035 $\pm.010$	7.20 $^{+0.77}_{-0.75}$	6.65 $^{+1.82}_{-1.57}$	.20
	$\mathbf{E}\langle 110\rangle$ $T > 10^0$C,5.8kG	2.592 $\pm.004$	3.035 $\pm.008$	7.28 $^{+0.60}_{-0.57}$	6.65 $^{+1.4}_{-1.25}$	.12

Table 5: Fit results for Fe K edge data of sample#3. The range of the data for a $k\chi(k)$ Fourier transform was 1.88 to 9.90Å^{-1} with a Hamming window. The range for the R-space fits was .96-3.27Å. Fixed parameters $N_1\langle 110\rangle = 6.0$, $N_2\langle 110\rangle = 6.0$, $N_1\langle 100\rangle = 6.0$, $N_2\langle 100\rangle = 6.0$ $\Delta E_1 = -.960$eV, $\Delta E_2 = -9.601$eV, $a_1 = -1.117$, $a_2 = -1.721$.

crystal diffraction pattern.

The important quantities are differences in radial distances under various conditions. Consider sample#1. The magnetic field was applied in the $\langle 111 \rangle$ direction (figure 13). Regardless of the conditions applied there is no detectable change in the Fe-Fe or the Fe-rare-earth distances when the $\langle 111 \rangle$ direction is probed. The same conclusion is arrived at by probing the $\langle 112 \rangle$ direction. In some cases a very small effect seems discernible but the error bars have the same magnitude hence no detectable changes must be concluded. Sample#2 had the magnetic field applied in the $\langle 112 \rangle$ direction. In this case whether probing the $\langle 112 \rangle$ direction or the $\langle 110 \rangle$ direction there is no discernible change in the Fe-Fe distance or the Fe-rare-earth distance. Having said this, it is noticed that $R_1^{\perp} > R_1^{\parallel}$ and $R_2^{\perp} > R_2^{\parallel}$ for both samples#1 and #2. Also for these two samples $\sigma_{1\perp}^2 > \sigma_{1\parallel}^2$. Sample#3 is the sample with the magnetic field applied in the $\langle 100 \rangle$ direction. In this direction the effect of the magnetic field is expected to be extremely small (recall $\lambda_{111} > \lambda_{100}$) and not be detectable by EXAFS. This is what is observed.

4.2.2 Dy L_{III} edge results

The same data analysis procedure as used for the Fe K edge was employed for the Dy L_{III} edge data. The rare-earth atoms are surrounded by Fe atoms at 3.035Å and the second nearest neighbor is at 3.16Å. Note that Tb (atomic

number 65) and Dy (atomic number 66) are indistinguishable from an EXAFS viewpoint. For the remainder of this section any mention of Dy atoms should be interpretated as Dy or Tb atoms.

A one shell fit was performed rather than a 2 shell fit because the first two shells are so close together($\approx$.14Å) that any beating between the two shells would occur at a k value beyond the range of the data. Also, the number of atoms in the second shell is only $\frac{1}{3}$ the first shell number so the contribution is small. The derivative of the phase for the first peak of the Fourier transform shown in figure 29 supports the argument of a one shell fit. The large dip at low and high k's are the result of transform artifacts which are introduced during the Fourier filtering procedure.

For a L_{III} edge the polarization dependent coordination number is [37]

$$N_{eff} = \sum_{i=1}^{N} \frac{3\cos^2\theta_i + 1}{2}. \tag{52}$$

In the present case there is no polarization dependence because the rare-earth atoms occupy sites of cubic symmetry. The fits were done with $N_1 = 12$ as a fixed parameter. S_0^2 and the mean free path term were not adjusted. Tables 6, 7 and 8 are the results of curve fitting the data taken at the Dy L_{III} edge.

From the point of view of the Dy its nearest neighbors are Fe atoms. In all three samples the results do not show any deviations of the Dy-Fe distance under the various conditions.

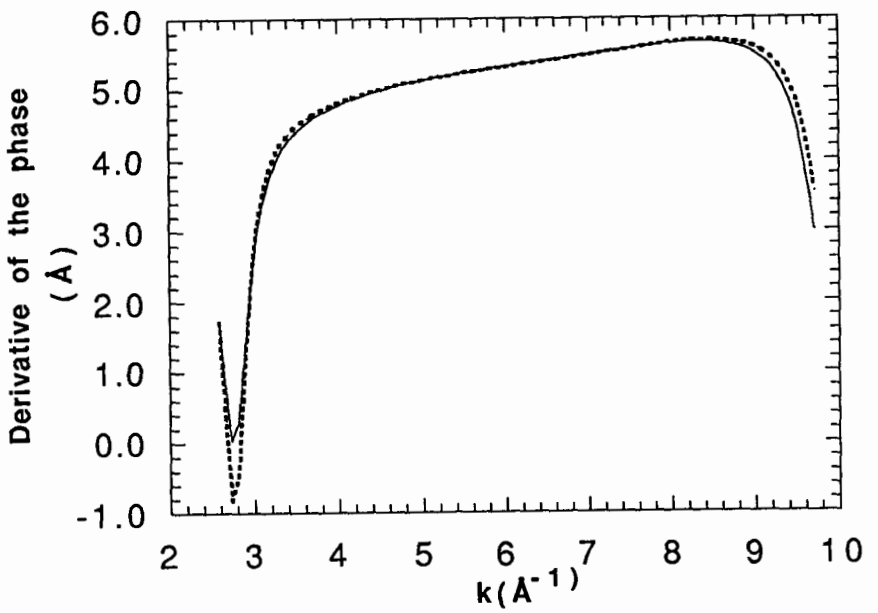

Figure 29: Derivative of the phase for Dy L_{III} edge data of Terfenol-D. Fourier transform range 2.40Å^{-1} to 9.75Å^{-1}. Fourier filtering range 1.64Å to 3.70Å. The solid line is the data taken with no applied field and the dashed line is the data with $B = 5$kG applied along the $\langle 111 \rangle$.

Sample #1 Dy L_{III}		R_1(Å)	σ_1^2 $\times 10^{-3}$	χ^2 $\times 10^{-4}$
$\mathbf{E}_{\parallel}$	$\mathbf{E}\langle 111\rangle$ $T < 10^0$C,$B = 0$	3.035	8.32	.29
	$\mathbf{E}\langle 111\rangle$ $T < 10^0$C,5kG	3.036 $\pm.014$	8.24 $^{+2.50}_{-2.07}$	.28
	$\mathbf{E}\langle 111\rangle$ $T > 10^0$C,$B = 0$	3.035 $\pm.013$	8.37 $^{+2.32}_{-1.94}$	.24
	$\mathbf{E}\langle 111\rangle$ $T > 10^0$C,5kG	3.037 $\pm.013$	8.79 $^{+2.40}_{-2.00}$	.24
$\mathbf{E}_{\perp}$	$\mathbf{E}\langle 112\rangle$ $T < 10^0$C,$B = 0$	3.037 $\pm.013$	7.94 $^{+2.33}_{-1.95}$	.26
	$\mathbf{E}\langle 112\rangle$ $T < 10^0$C,5kG	3.036 $\pm.013$	8.24 $^{+2.35}_{-1.97}$	.25
	$\mathbf{E}\langle 112\rangle$ $T > 10^0$C,$B = 0$	3.037 $\pm.012$	8.22 $^{+2.22}_{-1.88}$	.23
	$\mathbf{E}\langle 112\rangle$ $T > 10^0$C,5kG	3.036 $\pm.013$	8.28 $^{+2.40}_{-2.00}$	.26

Table 6: Fit results for Dy L_{III} edge data of sample#1. The range of the data for a $k\chi(k)$ Fourier transform was 2.40 to 9.75Å^{-1} with a Hamming window. The range for the R-space fits was 1.64Å - 3.70Å. Fixed parameters $N_1 = 12$, $\Delta E_1 = 4.606$, $a_1 = 1.147$.

Sample #2 Dy L_{III}		R_1(Å)	σ_1^2 $\times 10^{-3}$	χ^2 $\times 10^{-4}$
$\mathbf{E}_\parallel$	$\mathbf{E}\langle 112\rangle$ $T < 10^0$C,$B = 0$	3.037	7.92	.31
	$\mathbf{E}\langle 112\rangle$ $T < 10^0$C,5kG	3.034 $\pm .013$	7.72 $^{+2.39}_{-1.99}$	.28
	$\mathbf{E}\langle 112\rangle$ $T > 10^0$C,$B = 0$	3.035 $\pm .014$	8.20 $^{+2.51}_{-2.07}$	.28
	$\mathbf{E}\langle 112\rangle$ $T > 10^0$C,5kG	3.038 $\pm .014$	8.12 $^{+2.51}_{-2.07}$	.29
$\mathbf{E}_\perp$	$\mathbf{E}\langle 110\rangle$ $T < 10^0$C,$B = 0$	3.034 $\pm .016$	8.49 $^{+3.07}_{-2.44}$	.38
	$\mathbf{E}\langle 110\rangle$ $T < 10^0$C,5kG	3.036 $\pm .013$	8.15 $^{+2.41}_{-2.01}$	.26
	$\mathbf{E}\langle 110\rangle$ $T > 10^0$C,$B = 0$	3.038 $\pm .016$	8.46 $^{+3.01}_{-2.41}$	.37
	$\mathbf{E}\langle 110\rangle$ $T > 10^0$C,5kG	3.034 $\pm .013$	8.18 $^{+2.44}_{-2.03}$	.27

Table 7: Fit results for Dy L_{III} edge data of sample#2. The range of the data for a $k\chi(k)$ Fourier transform was 2.40 to 9.75Å^{-1} with a Hamming window. The range for the R-space fits was 1.64Å - 3.70Å. Fixed parameters $N_1 = 12$, $\Delta E_1 = 3.152$, $a_1 = .921$.

Sample #3 Dy L_{III}		R_1(Å)	σ_1^2 $\times 10^{-3}$	χ^2 $\times 10^{-4}$
$\mathbf{E}_\parallel$	$\mathbf{E}\langle 100\rangle$ $T < 10^0$C,$B = 0$	3.035	9.27	.30
	$\mathbf{E}\langle 100\rangle$ $T < 10^0$C,5.8kG	3.036 $\pm.014$	8.24 $^{+2.50}_{-2.06}$	.23
	$\mathbf{E}\langle 100\rangle$ $T > 10^0$C,$B = 0$	3.035 $\pm.015$	8.37 $^{+2.65}_{-2.17}$	.26
	$\mathbf{E}\langle 100\rangle$ $T > 10^0$C,5.8kG	3.037 $\pm.014$	8.79 $^{+2.53}_{-2.08}$	.22
$\mathbf{E}_\perp$	$\mathbf{E}\langle 110\rangle$ $T < 10^0$C,$B = 0$	3.032 $\pm.013$	7.94 $^{+2.23}_{-1.87}$	.22
	$\mathbf{E}\langle 110\rangle$ $T < 10^0$C,5.8kG	3.033 $\pm.012$	8.24 $^{+2.22}_{-1.87}$	.21
	$\mathbf{E}\langle 110\rangle$ $T > 10^0$C,$B = 0$	3.032 $\pm.012$	8.22 $^{+2.22}_{-1.87}$	.21
	$\mathbf{E}\langle 110\rangle$ $T > 10^0$C,5.8kG	3.031 $\pm.013$	8.28 $^{+2.27}_{-1.90}$	.21

Table 8: Fit results for Dy L_{III} edge data of sample#3. The range of the data for a $k\chi(k)$ Fourier transform was 2.70 to 9.75Å^{-1} with a Hamming window. The range for the R-space fits was 1.64Å - 3.70Å. Fixed parameters $N_1 = 12$, $\Delta E_1 = 1.378$, $a_1 = .763$.

4.3 Conclusion

EXAFS analysis of Tb-Dy-Fe data taken with an applied magnetic field do not reveal any distortions. In the first two samples the nearest neighbor distance and the second nearest neighbor are larger when the data is taken with **E** perpendicular to the direction of the applied field then when it is applied parallel. The anticipated changes in R given that $\lambda_s = 1068 \times 10^{-6}$ are .003Å. This order of resolution has been obtained on changes in R with EXAFS, on simpler one shell systems where the phase difference method was applicable[61]. For this ternary alloy, the first two shells are not resolved by the Fourier transform and the backscattering and absorbing atoms are different species. Therefore the absolute values of R must first be obtained by curve fitting methods for all cases before differences can be calculated. This, as well as correlations between parameters during curve fitting causes larger uncertainties than extracting the change in R directly using the phase difference method. The use of EXAFS as the equivalent of a microscopic strain gauge to probe which atoms contribute to the observed macroscopic strains is beyond the resolution of this technique for this system.

5 Fe/Cu/Fe Trilayers

5.1 Introduction

One of the first systems for which a long wavelength oscillation of the exchange coupling as a function of spacer thickness was clearly established is that of Fe/Cu/Fe structures grown on Ag(001). The exchange coupling between two layers, A and B, is usually described by

$$E_{AB} = -J_{AB}\left(\frac{\vec{M}^A\vec{M}^B}{|M_s^A||M_s^B|}\right) = -J_{AB}\cos\theta \tag{53}$$

where J_{AB} is the interlayer exchange coupling and θ is the angle between the magnetic moments. The interlayer exchange interaction can be understood from a simple physical picture. The ferromagnetic layers partially polarize the non-ferromagnetic spacer electrons. The induced spin polarization in the non-ferromagnetic spacer results in an oscillatory exchange coupling between the two ferromagnetic layers. The periodic oscillation is determined by topological features of the Fermi surface.

For the Fe/Cu/Fe structures grown on Ag(001) the exchange coupling has a crossover from ferromagnetic coupling to antiferromagnetic coupling at a thickness of ≈8ML. Beyond the 8ML the coupling remains antiferromagnetic with a long wavelength oscillation having a period of ≈10ML[22],[23]. For wedged Fe/Cu/Fe whisker samples crossover to antiferromagnetic coupling occurs at a Cu thickness of 10ML[62]. The exchange coupling is lower than for the non-

wedged samples with improved interfaces, but beyond 10ML has oscillations with a short wavelength (≈2ML) which are more pronounced.

Structural characteristics seem to affect strongly the observed magnetic properties. The Ag(001) surfaces are rougher than Fe whiskers which have atomically flat surfaces. The RHEED (Reflection High Energy Electron Diffraction) patterns for the system grown on Ag(001) substrate indicate that the first Fe/Cu interface is rougher than the second Cu/Fe interface when all layers are grown at room temperature. The first interface can be improved to be as good as the second interface by growing the last 3 or 4 layers of Fe at elevated temperatures[63]. In these trilayers the RHEED pattern suggests the bcc stacking sequence is maintained until a critical thickness of ≈11ML. Additional superlattice streaks are observed at larger thicknesses. This is similar to the case of bcc Ni(001) which EXAFS confirmed had a gradual lattice transformation, from a bcc phase in the first few monolayers to an fcc phase at 37ML[64]. A similar lattice transformation is assumed for the Cu. In disagreement with this view the growth of Cu on a Fe whisker monitored simultaneously by RHEED and LEED (low electron energy diffraction) indicated that the Cu maintains a bcc structure up to at least 20ML[62]. RHEED is only sensitive to the in-plane structure. X-ray techniques are now being used to probe the structural behavior of the Cu grown on Fe.

One study, an EXAFS study[65], on sputtered Fe/Cu/Fe multilayers indicate substantial lattice modifications. For Cu thicknesses 6Å and 13Å the nearest neighbor distance in Cu was 1% larger than that found in bulk Fe where $R_1 =$ 2.485Åand the local structure was characteristic of bcc. For samples whose thicknesses were 24, 42 and 60Å the nearest neighbor shell was that of fcc Cu[65]. Another study of sputtered epitaxial Cu on Fe(001) by glancing-incidence x-ray scattering found that although the initially deposited Cu resembles a bcc structure, it is actually a tetragonally distorted fcc structure[66]. The authors did not observe the 1.2% increase in the in-plane Cu d spacing from the RHEED study of films grown by MBE[21]. Their data were described by strain relaxation of the Cu overlayer[66].

First principles calculations based on calculating the total energy difference between the states with antiparallel and parallel alignments of the magnetic moments of magnetic layers separated by non-magnetic interlayers have been computed for Fe/Cu/Fe assuming Cu has a body-centre cubic structure[67]. The model predicts a cross-over to antiferromagnetic coupling at 5.5ML which is less than that observed experimentally. The antiferromagnetic coupling strength should be oscillatory with a period of 2.4ML with maximum values near 6ML and 8ML and a slightly positive ferromagnetic coupling at 7ML. Experimentally the same trend was observed in the Fe/Cu/Fe trilayers with improved interfaces

for which 3ML of Fe are grown at 150^0C. Beyond the cross-over point of 8ML a short wavelength oscillation with a period of 2.2ML and maxima of antiferromagnetic coupling at even numbers of monolayers was observed[63]. Note that the model does not assume the presence of any surface roughness.

It seems that the deposition technique as well as surface preparation of the substrate are important parameters in the structural outcome of these thin films. The purpose of the present work is to use glancing-incidence x-ray absorption fine structure spectroscopy to determine the local structure for films prepared and grown by MBE under the same conditions as those used for the initial Fe/Cu/Fe studies[22],[23] with the Fe underlayer grown at elevated temperatures.

5.2 Principles of Molecular Beam Epitaxy

Molecular beam epitaxy (MBE) is a crystal growing technique involving the reaction of one or more thermal beams of atoms with a crystalline surface under ultrahigh vacuum conditions. The formation of thin films occurs by the nucleation and growth of many individual crystallites. As the deposition proceeds, the nuclei grow until there is a continuous film. The thickness at which the porosity disappears depends on deposition rate, temperature and the nature of the substrate. For two dimensional growth the nuclei must spread laterally more rapidly than they thicken. The temperature of the substrate during the growth

affects the critical size and the rate of formation of the nuclei, the mobility of the adsorbed atoms and the annealing of defects in the condensed films. At low temperatures the critical size of the nuclei is small and the mobility of adsorbed atoms is low. Only atoms that impinge near the nuclei will reach them. The rate of nucleation is large. At high temperatures, surface mobility increases, rate of nucleation decreases, therefore the films form from fewer nuclei. However if the temperature is too high three dimensional crystallites will grow[68].

There are three distinct growth modes[69]. The Frank-Van der Merwe growth is a layer-by-layer growth. The second layer does not start until the first layer is completed. The Volmer-Weber growth occurs when three dimensional crystallites form upon contact and the overlayers may not cover the exposed substrate completely until a large number of atoms have been deposited. The third growth mode (Stranski-Kastanov growth) is an intermediate mode. A few monolayers grow before three dimensional clusters begin to form. This classification is an over simplification since these models do not consider the details of the substrate's surface quality which plays an important role in the nucleation process.

Since MBE growths are done in an ultrahigh vacuum environment this permits the use of a host of surface analytical tools (RHEED (Reflection High Energy Electron Diffraction), AES (Auger Electron Spectroscopy), LEED (Low

Electron Energy Diffraction) etc.) which assist in monitoring the growth and optimizing the growth conditions. This advantage is one of the reasons of the major advances in this technology in recent years.

In this study RHEED was used to monitor the growth mode and characterize the quality of the grown layers. Glancing-incidence EXAFS used ex-situ was employed to determine structural parameters in buried epitaxial layers. The experimental conditions permit the determination of in-plane and out-of-plane structural parameters.

5.3 The MBE facility

The molecular beam epitaxy (MBE) system is a Physical Electronics Molecular Beam Epitaxy System, model Φ-400. It consists of two main chambers - the analysis chamber and the growth chamber. The analysis chamber is used for substrate preparation and diagnostics. It is equipped with an ion sputtering gun (Φ model 04-191), a double pass cylindrical mirror analyzer(CMA) (Φ model 15-110) and an electron gun. The ion sputtering gun permits sputtering to remove contaminants from the surface. The electron gun and the CMA are the components that permit Auger electron spectroscopy(AES) to be used as a diagnostic tool to verify the cleanliness of the surface.

The growth chamber has a Reflection High Energy Electron Diffraction(RHEED) system and a quartz crystal thickness monitor both of which are used to moni-

tor the growth. Of course the chamber has several furnaces for different growth materials. The RHEED system has an electron gun that generates a beam of electron whose energies can be between .5 to 5keV. The beam impinges on the surface of the substrate at a low angle of incidence (1 to 5^0). A phosphorescent screen located 30.5cm from the center of the sample, displays the diffraction pattern. The intensities and profiles of the diffracted spots can be measured with a photomultiplier tube fitted with a microscope objective lens and a 50μm diaphragm. The photomultiplier is connected to an x-y recorder. The thickness monitor (Mathis model TM-100) is located 1cm above the substrate. It consists of two piezoelectric quartz crystals connected to a 6MHz resonant circuit. The crystals and the electronics are water cooled and the temperature of the circulating water is stabilized by a thermostat (Haake model E3). The well calibrated thickness monitor is used to determine the overall thickness of the layers to within $\pm$0.2ML. The furnaces containing the Fe, Cu and Au used in this study are mounted at about 90^0 from the RHEED system. They are enclosed in a cryoshroud cooled by liquid nitrogen. The geometrical arrangement of the components of the growth chamber are shown in figure 30.

The sample is introduced into the system via an introductory chamber. It is mounted on a molybdenum holder which is screwed to the manipulator rod. The chamber is back-filled with dry nitrogen. A turbomolecular pump will

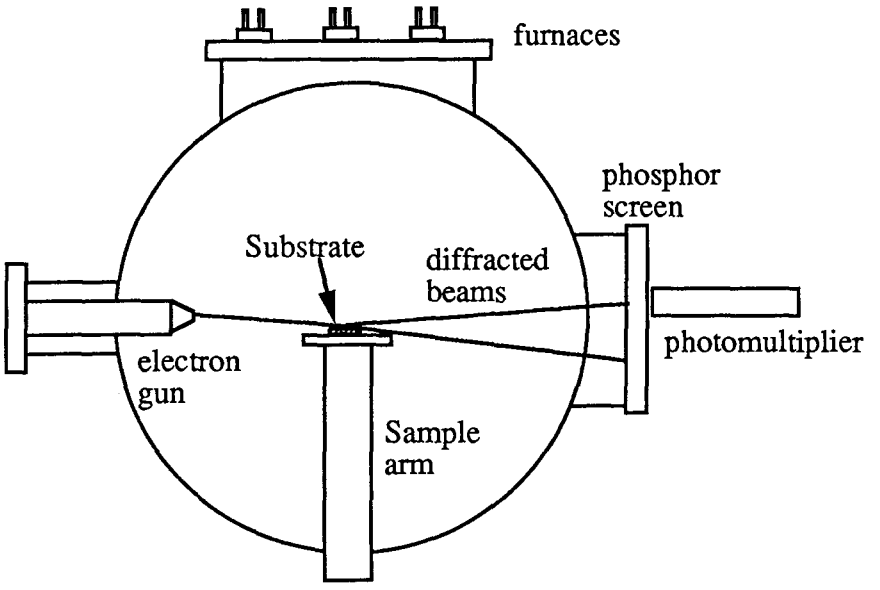

Figure 30: Schematic of the growth chamber of the MBE system.

pump until the pressure in the chamber reaches the low end of the 10^{-6} Torr scale. An electric motor then moves the sample through a pneumatic valve and into the analysis chamber. There is an ion pump connected to the analysis chamber and a cryopump connected to the growth chamber. The pressure of the system is usually of the order of 10^{-10} as monitored by several ionization gauges. Figure 31 is a cross-sectional view of the MBE system.

5.3.1 Auger Electron Spectroscopy (AES)

When a surface is bombarded with high energy electrons, 1 to 10keV, core electrons will be ejected. The ionized atom relaxes by filling the hole with electrons from higher levels, E_{L_I}. The energy balance, E_K-E_{L_I}, is available and

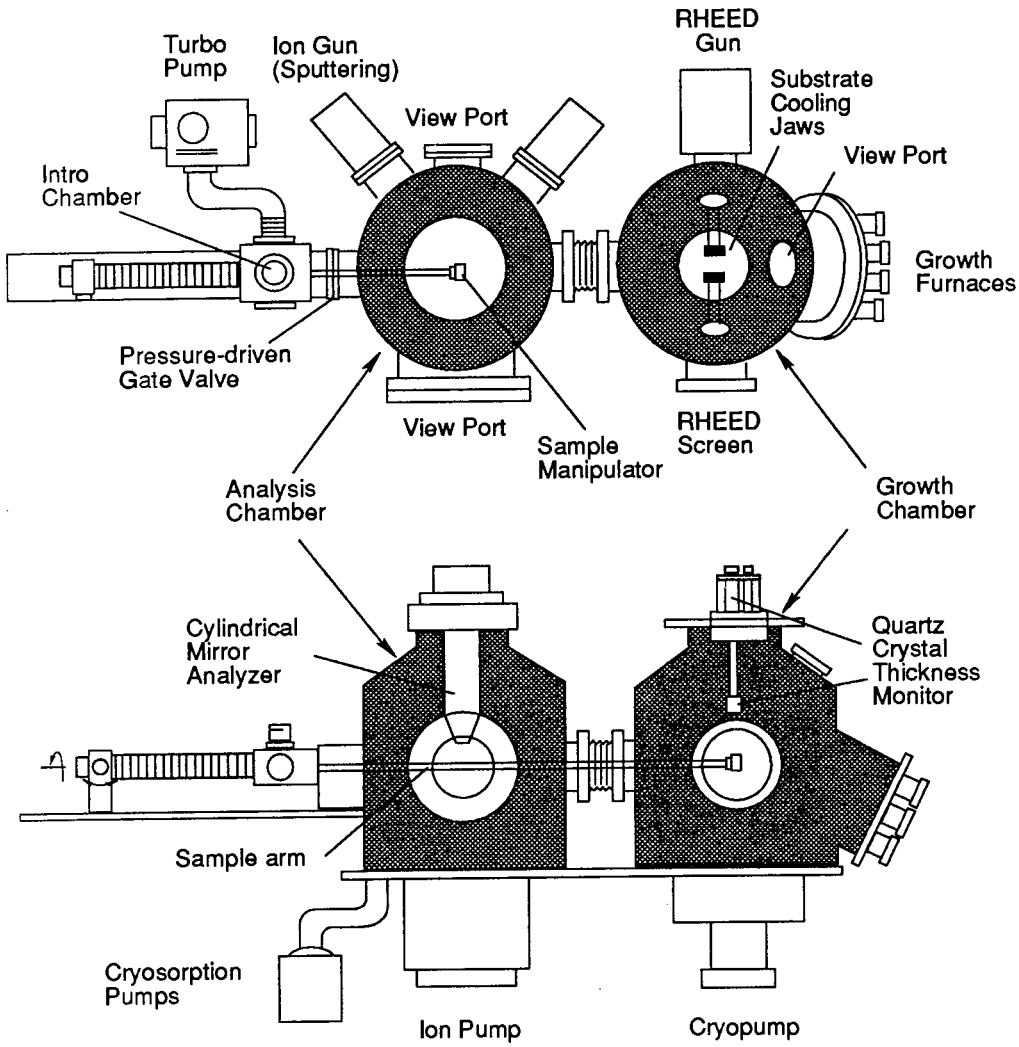

Figure 31: Cross-sectional view of the MBE system. The top figure is as viewed from above and the bottom figure is as viewed from the side.

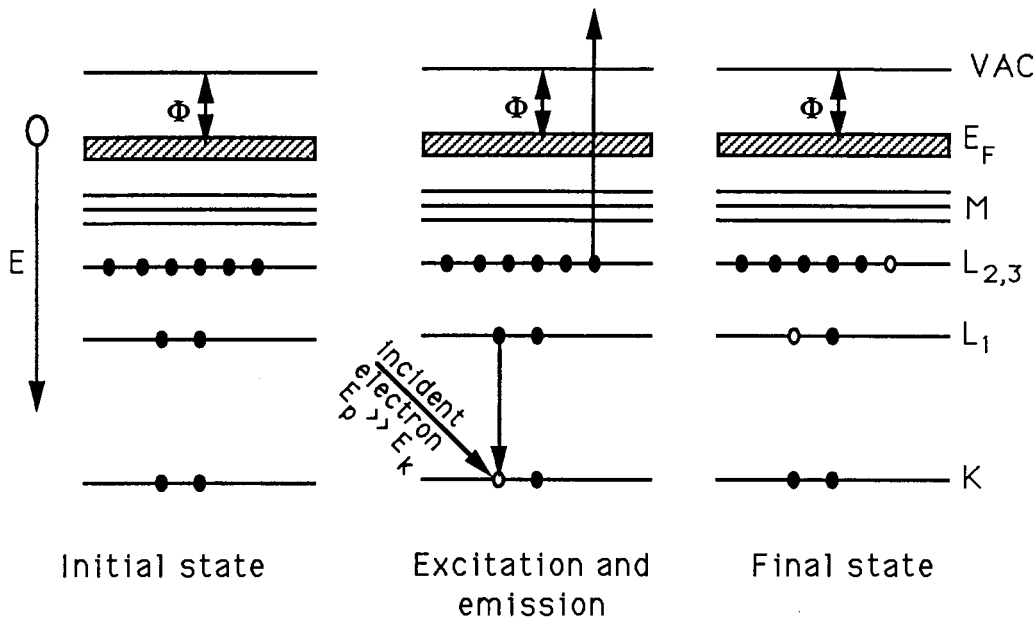

Figure 32: Auger process.

can be used by two different processes. One process is for an x-ray photon to be emitted (fluorescence) and the second is for an electron with energy $E_{L_{II,III}}$ to be ejected from the atom. This electron is the Auger electron. The second process is more probable than the fluorescence for lighter elements with atomic number less than 29. The process for the ejection of Auger electrons is schematically represented in figure 32. The energy of the Auger electron is given by,

$$E_{KL_IL_{II,III}} = E_K - E_{L_I} - E_{L_{II,III}} \tag{54}$$

where $E_{L_{II,III}}$ is the binding energy of the $L_{II,III}$ level with a hole in level L_I (see for example [70]). Therefore the energy of the Auger electron depends solely on the atomic energy levels of the atomic species being investigated. Put another way each atomic species has a specific set of available Auger energies.

Auger electron spectroscopy consists of measuring the energies of these Auger electrons. Identification of the elements involved can be readily obtained from comparison with a standard spectra[71]. Before escaping from the surface of the solid, the Auger electron can interact with the solid through inelastic scattering and lose the original well defined energy. The average distance the electron can travel within the solid before escaping from the surface without scattering is the inelastic mean free path, λ, which can be approximated by the formula developed by Seah and Dench[72],

$$\lambda(nm) = \frac{538}{n^{1/3}E_{KIN}^2} + \left(\frac{E_{KIN}}{n}\right)^{1/2} \tag{55}$$

where n (in atoms/nm^3) is the number density of the material through which the electron is travelling and E_{KIN} (in eV) is the kinetic energy of the ejected electron. The inelastic mean free path is usually in the range between 4-40Å. Therefore, AES is sensitive to atoms near the surface.

Monitoring the intensity of an Auger peak from the substrate for example, after the growth of overlayers can provide a means of measuring the thickness since the intensity will decrease exponentially with increasing overlayer thickness according to

$$I(d) = I_0 \exp\left(\frac{-d}{\lambda \cos\alpha}\right) \tag{56}$$

where α, the acceptance angle of the detector, is the angle of emission relative to the surface normal.

5.3.2 Reflection High Energy Electron Diffraction (RHEED)

Reflection high energy electron diffraction consists of striking a surface with a beam of electrons at a glancing angle, typically 1^0 and recording the diffraction pattern obtained. Since the electrons interact strongly with the solid this is a surface specific probe. The glancing-incidence mode ensures that only 1 or 2 monolayers are probed. The phenomenon can be explained qualitatively using a kinematic model[27],[73],[74] but a full quantitative analysis would required a more elaborate model that includes dynamical effects. A full dynamical model has yet to be developed.

The resultant RHEED pattern will display a straight through beam, which is that part of the beam that misses the sample, a specular spot and other diffraction spots. A typical example for Fe grown on Ag(001) substrate is shown schematically in figure 33. In this figure the central streak corresponds to the specular spot and the other two streaks are additional diffraction spots. The straight through beam does not appear in the figure. Inelastic scattering creates a bright background in the upper part of the figure and the presence of the sample produces a shadow hence the darker lower half in the figure. Based on the kinematic theory, some structural information can be extracted.

Consider a perfectly smooth single crystal surface in the x-y plane with a beam of electrons impinging on the surface at glancing incidence. The crystal

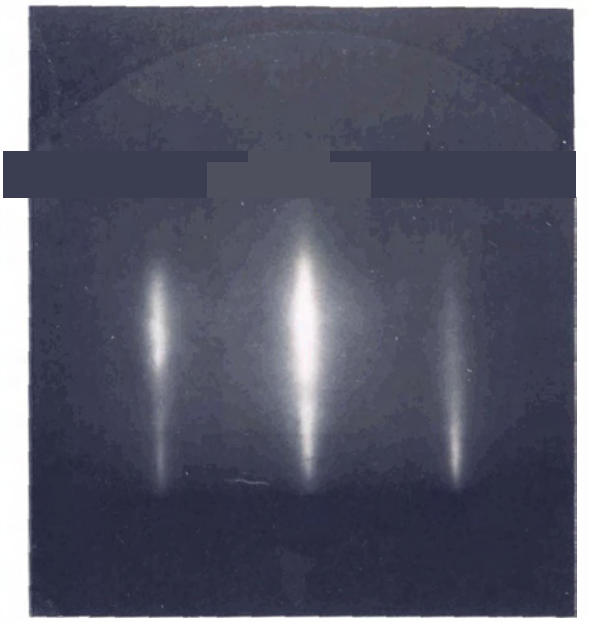

Figure 33: RHEED pattern obtained from the surface of Fe deposited by MBE on a silver substrate.

lattice is a two dimensional periodic array of scatterers whose positions can be described by $\vec{R} = n_1\vec{a}_1 + n_2\vec{a}_2$ with $n_1 = 0, 1, 2...N_1 - 1$, $n_2 = 0, 1, 2...N_2 - 1$ and N_1, N_2 are the number of atoms in the x,y directions respectively. For constructive interference to occur the phase difference between the reflected waves must be multiples of 2π,

$$\phi = \vec{R} \cdot (\vec{k}_i - \vec{k}_f) = 2\pi m \tag{57}$$

where $\vec{k}_i$ and $\vec{k}_f$ are the incident wavevector and the reflected wavevector respectively and m is an integer. In reciprocal space the lattice is periodic and discrete with basis,

$$\vec{k}_1 = \frac{2\pi\vec{a}_2 \times \hat{n}}{|\vec{a}_1 \times \vec{a}_2|} \qquad \vec{k}_2 = \frac{2\pi\hat{n} \times \vec{a}_1}{|\vec{a}_1 \times \vec{a}_2|} \tag{58}$$

where $\hat{n}$ is the normal unit vector[75]. Equation 57 will be satisfied if[27]

$$\Delta\vec{k} = \vec{k_i} - \vec{k_f} = m_1\vec{k_1} + m_2\vec{k_2} + m_3\hat{z} \tag{59}$$

where m_3 is an arbitrary number and $\hat{z}$ is a unit vector normal to the surface. The solution is a set of $\Delta\vec{k}$ which form a set of delta functions normal to the sample surface of infinite extent. Geometrically the conditions for constructive interference can be inferred from Ewald's construction, which is a simple construction permitting the visualization of elastic scattering in RHEED. The Ewald sphere in reciprocal space has a radius equal to the wavevector of the incident beam $\vec{k_i}$. The end point $\vec{k_i}$ on the perimeter of the sphere intersects a lattice point. All other wavevectors, $\vec{k_f}$, originating at the center of the sphere and the reciprocal lattice determine the directions of all possible diffracted beams. The intersection of the infinitely thin reciprocal lattice rods with the Ewald sphere will form a series of sharp spots as shown in figure 34[76].

The reflection for which the reflected angle is equal to the angle of incidence is called the specular reflection or the specular spot. For a cubic array the specular spot, the straight through beam and other diffracted spots will lie on a circle, the Ewald circle (figure 35).

Crystals are usually not perfect. Due to the finite extent of the crystal the reciprocal lattice rods have a finite thickness.The crystal planes from one crystallite to the next may be slightly misoriented relative to each other, this

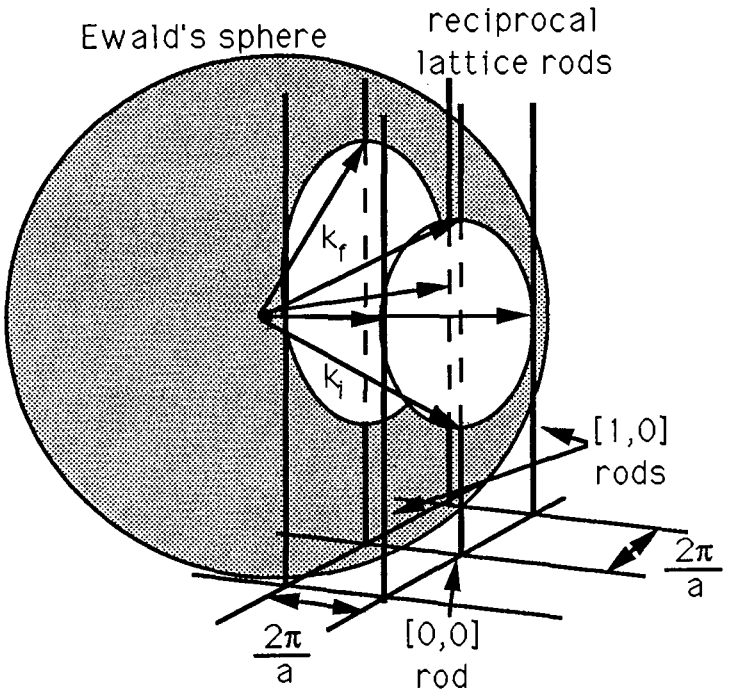

Figure 34: Ewald's construction

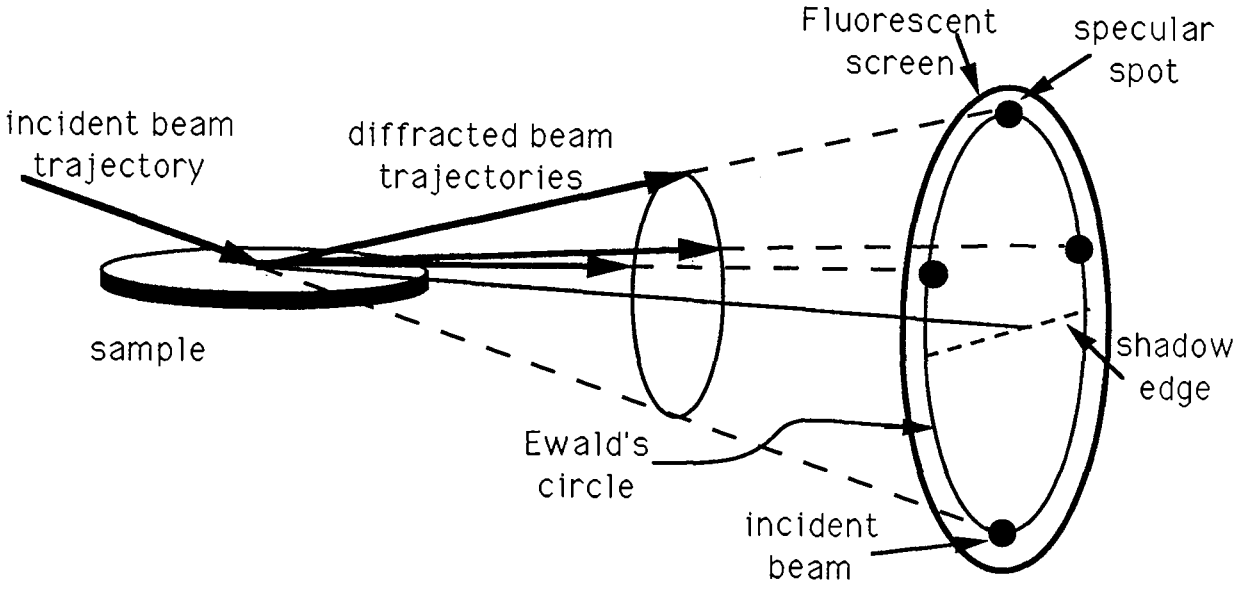

Figure 35: The RHEED geometry in real space

is described as mosaic spread. The reciprocal lattice rods from a crystal with mosaic spread will be thickened and the intersection with the Ewald sphere will cause the ideal spots to be lengthened in a direction perpendicular to the surface (streaks). The width of a streak is roughly a measure of the size of the islands on the surface[74].

During the growth the surface will cycle through a rough phase and a smooth phase corresponding to a partially filled layer and a completely filled layer respectively. Ideally the growth of a layer does not start until the full completion of the previous layer. If the intensity of the specular spot is monitored during the growth it will change with time because of the interference between the beams reflected from the underlying layer and the partially filled layer (see figure 36). As a function of coverage, C, the intensity is

$$I = C^2 + (1 - C)^2 + 2C(1 - C)\cos\gamma \tag{60}$$

For full coverage C is unity and for no coverage C equals zero. The phase angle between scattered beams from adjacent planes is $\gamma = 2dsin\phi$. When $\gamma = 2n\pi$, the condition for constructive interference between the two reflected waves, the intensity will be constant in time. At the anti-Bragg condition (or for destructive interference) $\gamma = (2n-1)\pi$ and the oscillations are periodic in time. The maximum is reached when a monolayer is completed and the minimum occurs when 50% of a monolayer covers the surface. This model based on the

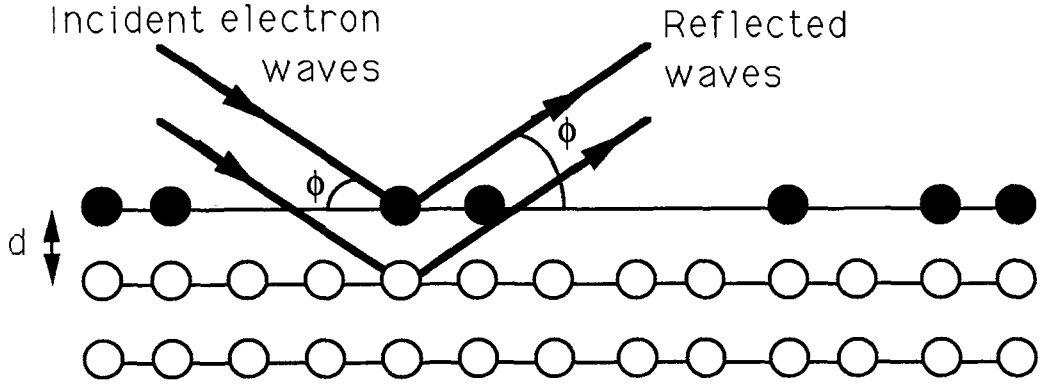

Figure 36: Schematic diagram of the top two layers participating in the intensity oscillations of the specular beam

kinematic theory was proposed by Van Hove[77].

5.4 Sample Growth

The trilayers were grown on single crystal silver substrates. The silver boule was provided by Monocrystals Co., Ohio. Laue diffraction was used to determine the [001] direction and slices 8 to 10mm thick were cut along the (001) plane with a spark cutter. The diameter was 19mm. Two slits approximately 1mm deep were cut on the sides of the disks. These provided a means of holding the sample in the MBE system without obscuring the surface of the crystal. Each slice was bonded to an aluminium holder with Crystalbond^{TM}. This holder was mounted on a polishing jig and the crystal realigned to better than $.15^0$ from

the [001] direction. The Ag substrate then underwent several stages of manual mechanical polishing on Nylon pads (B1031 Micro Metallurgical Ltd., Ontario) with a slurry of aluminium oxide (Al_2O_3; also from Micro Metallurgical Ltd., Ontario) mixed with water. The sizes of Al_2O_3 particles used were 9μm, 5μm and 1μm. Polishing times were 30 minutes for the two larger particle sizes and 20 minutes for 1μm. Between each step the jig and sample were cleaned with alcohol in order to eliminate any remaining particles from the previous step. Polishing by successively using a slurry with a smaller particle size removed the damages from the previous step. The surface also became progressively shinier. The alignment and polishing procedure were done for both surfaces of the disk to ensure parallel surfaces. The final step involved electropolishing in a cyanide free electropolish solution[78] for 5 minutes. This last treatment removes the surface damage caused by the mechanical polishing and provides a smooth mirror-like finish. The substrate was then cleaned with acetone and dried with a flow of nitrogen gas to remove any traces of the electropolish solution and the Crystalbond^{TM} which held the sample to the aluminum base. Then the Ag substrate was clamped on a molybdenum holder by using tantalum clips inserted in the slits cut on the side of the crystal, and was placed in the introductory chamber where it remained for a couple of hours to outgas.

The substrate was then moved into the analysis chamber where AES was

used as a diagnostic tool to verify the cleanliness of the surface. AES revealed the presence of contaminants which were mostly sulfur and carbon. Therefore, room temperature sputtering was performed for approximately one hour. During this process the analysis chamber is filled with argon to a pressure of about 5×10^{-5} Torr. The argon ion beam had an energy of 2keV and was rastered over an area $10mm^2$. Sputtering can cause some surface damage, so the substrate was annealed at 550^0C for two hours. The annealing restores the quality of the surface but contaminants from within the bulk of the substrate start to surface. Therefore sputtering at the elevated temperature(550^0C) was done for 30 minutes at an argon pressure of 2×10^{-5} Torr. The temperature was lowered in steps of 50^0C and some sputtering performed for 30 minutes. At 350^0C the substrate was not sputtered any more, but remained at this temperature for approximately 10 minutes before the heating element was turned off. The Ag substrate was then allowed to cool to room temperature. AES confirmed the complete removal of the contaminants. Finally the substrate was moved to the growth chamber.

The RHEED patterns of the surface showed well defined streaks and the specular spot was readily distinguishable. Hence, the surface preparation as described above created good quality surfaces.

The growths of all layers were done in an environment where the pressure

was in the low 10^{-10} Torr region. The only exception was for the Au which was grown at higher pressures of about 4×10^{-10} Torr. Deposition rates were approximately 1 to 2ML per minute. The substrate temperature was kept at about 300^0K for the growth of the first 5ML of Fe. The substrate was then heated to approximately 150^0C for the growth of the next 3ML of Fe. The growth at elevated temperature causes larger terraces to be formed, hence a smoother surface for subsequent growth. The substrate is then cooled to the original temperature for the growth of the Cu layers, 5 more Fe layers and finally the Au layers. The quartz crystal thickness monitor was calibrated for each metal. It was used in conjunction with the RHEED system to monitor the growth. The electron beam for RHEED was at an incident angle of $\approx 1^0$. The intensity of the specular spot was measured with a photomultiplier tube and plotted on an x-y recorder. Cross-checking with the thickness monitor it was found that one oscillation corresponded to the deposition of a mass equivalent of approximately 1ML.

The three samples grown for this study are 10ML Au/5ML Fe/8ML Cu/3+5ML Fe/Ag(001), 10ML Au/5ML Fe/14ML Cu/3+5ML Fe/Ag(001), 10ML Au/5ML Fe/20 ML Cu/3+5ML Fe/Ag(001). A silver substrate was prepared for each sample. The graphs in figure 37 from bottom to top, are the RHEED oscillations recorded during the growth of Fe on Ag(001) and 8ML Cu on Fe respectively.

A cross-section of the sample is also illustrated. Similarly figure 38 shows the graphs for the growth of Fe on Ag(001), 20ML Cu on Fe and 5ML Fe on 20ML Cu.

The Ag template is ideal for the growth of Fe overlayers. Silver forms in a face-centered cubic(fcc) lattice whose lattice constant is 4.09Å[46]. At a 45^0 angle, the surface atoms form a square array with a length $b = 2.892$Å (see figure 39). This is very close, less than 1%, from the lattice constant of bcc Fe which is 2.87Å.[46]. For a perfectly smooth substrate (no steps) the growth of Fe should proceed smoothly. If there are steps or terraces on the surface of the Ag, then the growth is anticipated to be rough for several layers because of the large vertical mismatch($\approx 43\%$) between the Ag and Fe lattices. This is in fact observed in the RHEED oscillations. It takes approximately 5ML of Fe deposited at room temperature to obtain a constant period of oscillation.

A study using Mössbauer spectroscopy finds that the initial stages of the growth are quite rough[79]. In this study 1ML of Fe^{57} deposited on 3ML of Fe at room temperature reveals that 20% of the Fe^{57} are in contact with the Ag substrate. Repeating this procedure but with 1ML of Fe^{57} on 4ML of Fe shows that all of the Fe^{57} is occupying sites in the 4^{th} layer or 5^{th} layer. This confirms the observation from RHEED that 5ML of Fe on Ag(001) are required to form a smooth layer for which any subsequent growth will be in a layer-by-layer fashion.

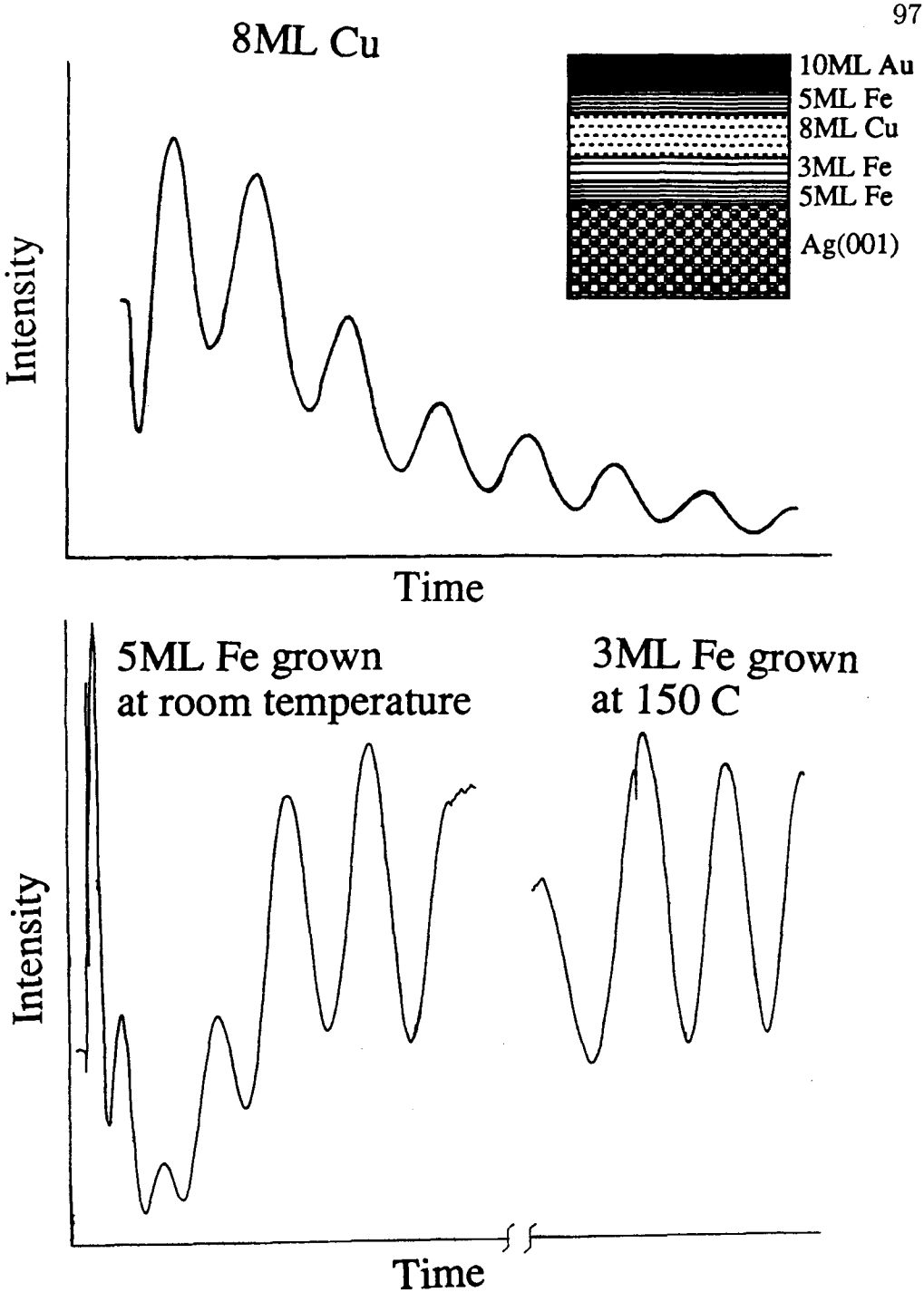

Figure 37: RHEED oscillations of the growth of 10ML Au/5ML Fe/8ML Cu/3+5ML Fe/Ag(001)

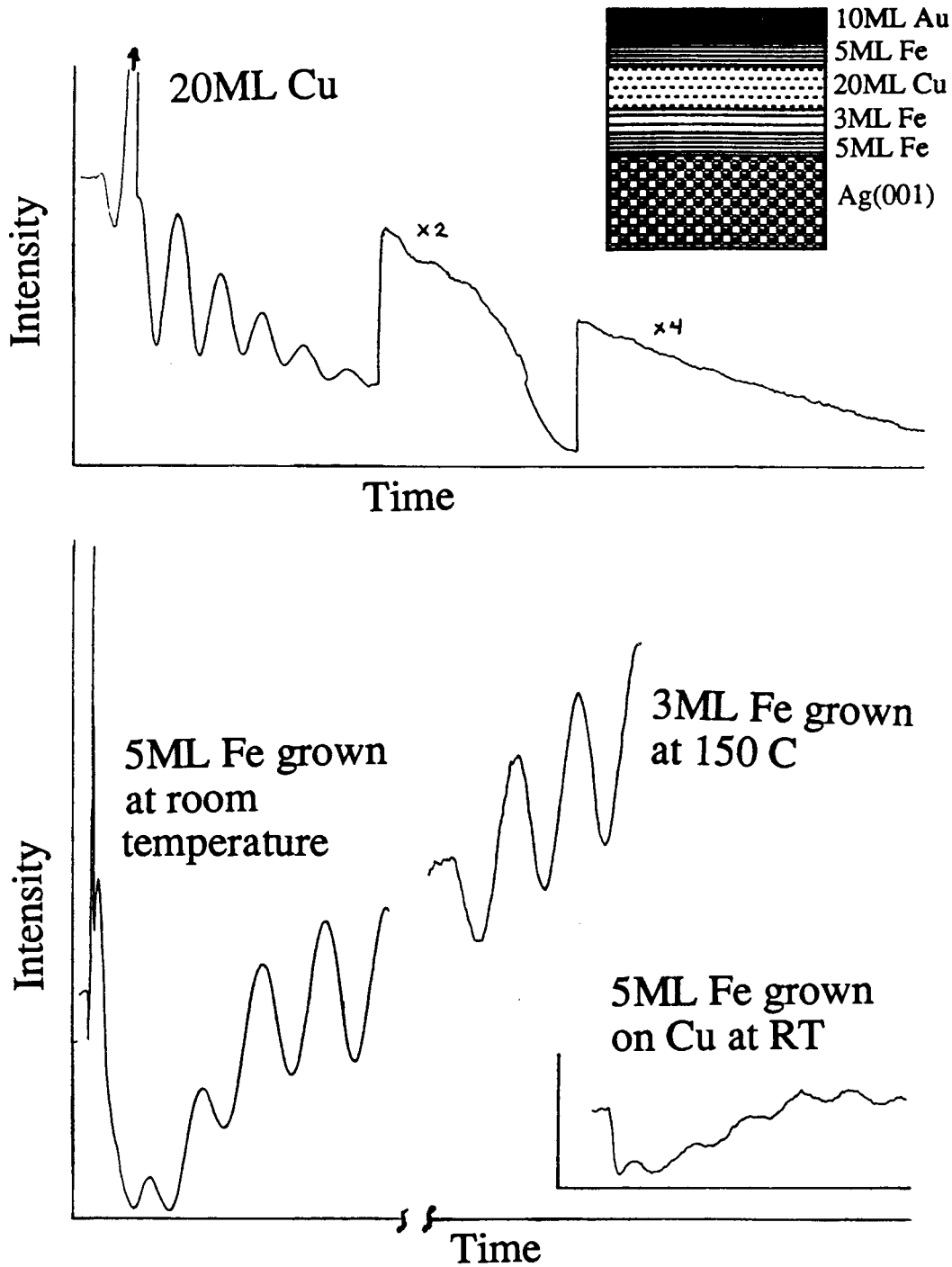

Figure 38: RHEED oscillations of the growth of 10ML Au/5ML Fe/20ML Cu/3+5ML Fe/Ag(001)

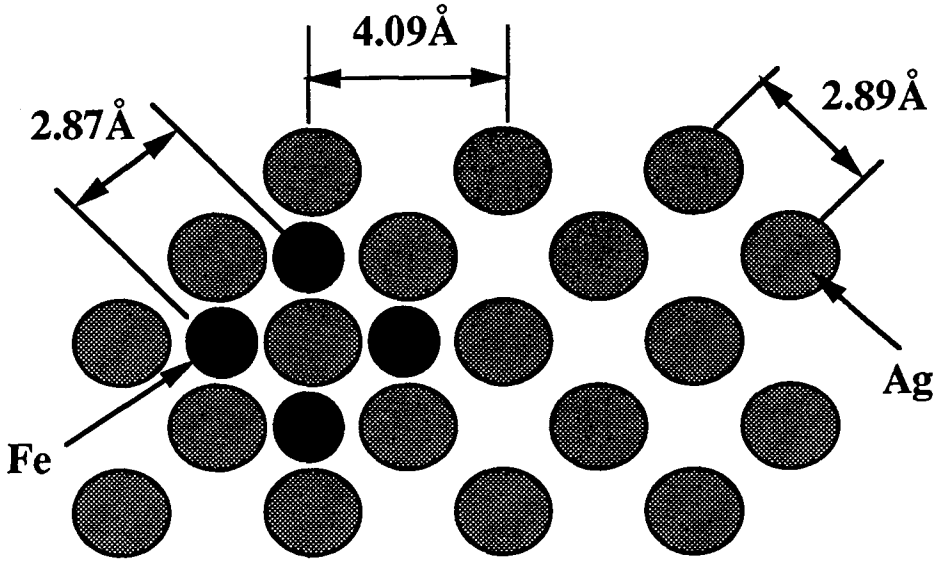

Figure 39: Lattice matching Fe with the Ag template

Three additional layers of Fe grown at 150^0C show strong periodic oscillations. The Fe layers form a smooth substrate for the subsequent deposition of Cu.

The lattice constant of Cu is 3.61Å[46] and it is 2.87Å for Fe[46]. The mismatch is large. Bulk Cu is found to have a fcc structure, like Ag. A 45^0 rotation of the Cu fcc structure with respect to the bcc Fe lattice still gives a mismatch of about 11%. The Cu lattice is not as well lattice matched to the Fe lattice as Ag. Regular RHEED oscillations are still observed during the growth of Cu on Fe. The amplitude of the oscillation decreases until a critical thickness of 12ML is reached. This is evidence that the size of clusters within a layer decreases as the thickness of the Cu increases toward the critical thickness. At this thickness additional superlattice streaks(see figure 40c and d) become visible

on the RHEED pattern suggesting perhaps a lattice transformation. During the initial stages of the growth of Cu the RHEED pattern observed is essentially the same as in Fe. (see figure 40a and figure 33) In summary, RHEED reveals that for thicknesses less than approximately 12ML the in-plane structure is a bcc structure expanded by $\approx 1\%$ relative to bcc Fe. Beyond the critical thickness of 12ML additional streaks in the RHEED pattern indicate that the growth of Cu is not following a bcc stacking anymore.

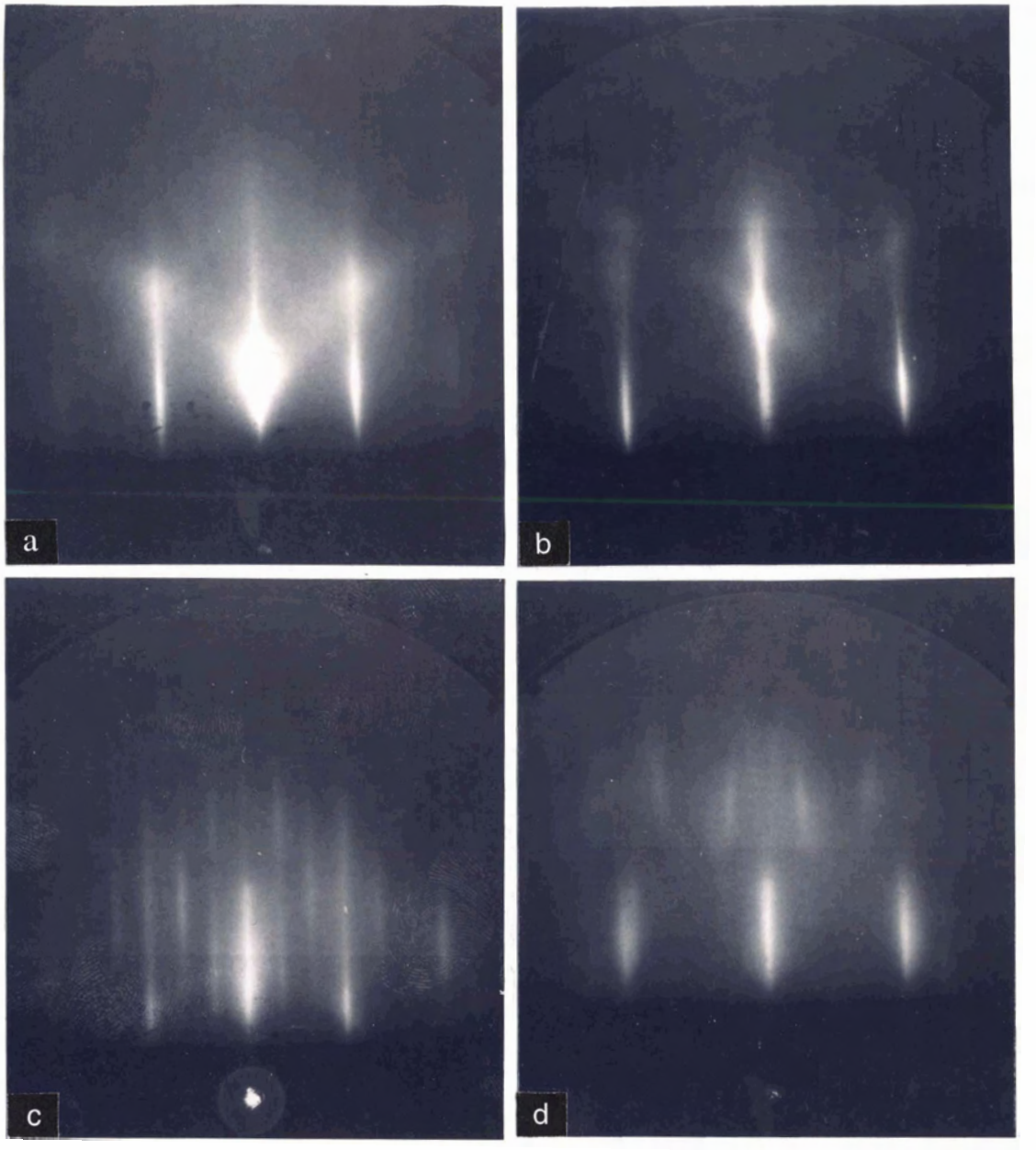

Figure 40: RHEED patterns for growth of Cu on Fe. a)8ML azimuth [100]; b) 8ML azimuth [110]; c)20ML azimuth [100]; d)20ML azimuth [110] From the separation distance between streaks at two azimuths the d spacing of Cu is $\approx 1\%$ larger than for Fe.

6 Glancing-Incidence EXAFS of Fe/Cu/Fe

6.1 Theory

When a monochromatic electromagnetic wave of angular frequency ω interacts with a conducting medium with a dielectric constant ϵ, permeability μ and conductivity σ, solving Maxwell's equation leads to the wave equation,

$$\nabla^2\vec{\mathbf{E}} + k^2\vec{\mathbf{E}} = 0 \tag{61}$$

The wave number k depends on σ, ϵ and μ. The propagation velocity of the wave is $v = c/\sqrt{\epsilon\mu}$. In the x-ray regime to a good approximation μ can be taken as unity. The other parameters of the material are complex quantities. The dielectric constant is[80]

$$\epsilon(\omega) = 1 + \frac{4\pi Ne^2}{m_e}\sum_{j,n}\frac{f_{jn}}{(\omega_{jn}^2 - \omega^2) - i\omega\gamma_{jn}} \tag{62}$$

where $f_{jn} = 2\omega_{jn}| < n|z|j > |^2$ is the oscillator strength, $\omega_{jn} = E_j - E_n$ is the excitation energy and $< n|z|j >$ is the dipole matrix element coupling the initial state n and the excited state j. Rewriting in terms of the atomic scattering factor $f = f_0 + f' + if''$,

$$\epsilon(\omega) = 1 - \frac{4\pi Ne^2}{m_e\omega^2}(f_0 + f' + if'') \tag{63}$$

In the coherent forward scattering case f_0 equals the atomic number. The f' and f'' terms are the anomalous scattering corrections.

If the two media through which the electromagnetic wave is travelling are homogeneous the sine of the angle θ_1 between the normal to the incident wave and the normal to the surface bears a constant ratio to the sine of the angle θ_2 between the normal of the refracted wave and the surface normal, this constant ratio is equal to the ratios of the velocities of propagation in medium 1, v_1 and in medium 2, v_2. This is Snell's Law,

$$\frac{\sin\theta_1}{\sin\theta_2} = \frac{v_1}{v_2} \tag{64}$$

The refractive index is defined as the ratio of $\frac{v_1}{v_2} = n_{12}$. If medium 1 is vacuum or air then the absolute refractive index is $n = \frac{c}{v}$. Since the refractive index $n = \sqrt{\epsilon(\omega)}$ and the second term of equation 63 is of the order 10^{-5} or less, upon neglecting the higher order terms the index of refraction is

$$n = 1 - \delta - i\beta \tag{65}$$

where,

$$\delta = \frac{N_0 e^2}{2\pi m_e c^2}\frac{\rho\lambda^2}{M}(f_0 + f') \tag{66}$$

$$\beta = \frac{N_0 e^2}{2\pi m_e c^2}\frac{\rho\lambda^2}{M}f''. \tag{67}$$

The density is ρ, the atomic weight is M, the wavelength is λ, m_e is the mass of the electron with a charge e, c is the speed of light and N_0 is Avogadro's number. The critical angle is the incident angle when the wave is totally reflected. This occurs when the refracted angle is 90^0. The glancing angle ϕ is the complement

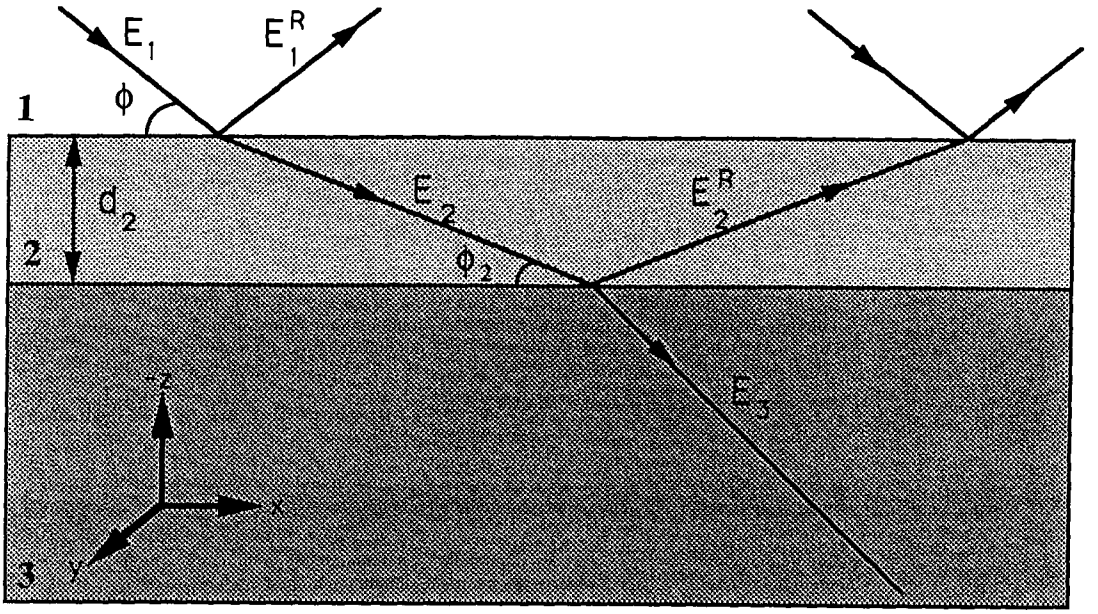

Figure 41: Reflection and refraction for a stratified homogeneous system with two interfaces. The electric vector is parallel to the surface of the sample.

of the incident angle θ_1. In the x-ray region $\delta \sim 10^{-6}$. Expressing Snell's law in terms of the critical glancing angle, ϕ_c, gives $\cos\phi_c = n$ from which $\phi_c = \sqrt{2\delta}$ ~milliradians.

Theoretical calculations of the reflectivity from a stratified homogeneous system in an x-ray glancing incidence case were first reported by Parratt[81]. The main results are outlined in the following paragraphs.

Consider a simple homogeneous system with two interfaces as illustrated in figure 41. The electric vector of the incident beam $\mathbf{E}_1(z_1)$, the reflected beam $\mathbf{E}_1^R(z_1)$ and the refracted beam $\mathbf{E}_2(z_2)$ at a distance z perpendicular to the

surface are,

$$\begin{aligned} \mathbf{E}_1(z_1) &= \mathbf{E}_1(0)\exp i[\omega t - (k_{1,x}x_1 + k_{1,z}z_1)] \\ \mathbf{E}_1^R(z_1) &= \mathbf{E}_1^R(0)\exp i[\omega t - (k_{1,x}x_1 - k_{1,z}z_1)] \\ \mathbf{E}_2(z_2) &= \mathbf{E}_1(0)\exp i[\omega t - (k_{2,x}x_2 + k_{2,z}z_2)] \end{aligned} \tag{68}$$

(69)

The propagation vector in medium 1 is k_1 and in medium 2 it is k_2. The x-y plane is parallel to the surface and the z direction is normal to it. Since the glancing angle for x-rays is of the order of milliradians,

$$\begin{aligned} k_{2,x}^2 + k_{2,z}^2 &= k_2^2 \\ k_2^2 &= n_2^2 k_1^2 \\ &= n_2^2\left(\frac{k_{1,x}^2}{\cos^2(\phi)}\right) \\ &= n_2^2 k_{1,x}^2 \sec^2(\phi) \end{aligned} \tag{70}$$

Keeping terms of order ϕ^2 or less and first order terms in δ_2 and β_2 then

$$k_2^2 = k_{1,x}^2(1 - 2\delta_2 - 2i\beta_2 + \phi^2) \tag{71}$$

From tangential boundary conditions, $k_{1,x} = k_{2,x}$. Since ϕ is small, $k_{1,x} \sim k_1$, therefore, $k_1 = k_{2,x}$. Equation 71 can then be rewritten as,

$$k_{2,z} \approx k_1(\phi^2 - 2\delta_2 - 2i\beta_2)^{\frac{1}{2}} \tag{72}$$

$$= k_1 f_2 \tag{73}$$

The expression for the refracted beam becomes,

$$\mathbf{E}_2(z_2) = \mathbf{E}_2(0) \exp[i(\omega t - k_{2,x} x_2)] \exp[-i k_1 f_2 z_2] \tag{74}$$

The ratio of reflected to incident intensity is obtained by using Fresnel's coefficient for reflection[82] which is

$$F_{1,2} = \frac{E_1^R}{E_1} = \frac{\sin\phi - n_2 \sin\phi_2}{\sin\phi + n_2 \sin\phi_2} \tag{75}$$

This is written for the σ component of the polarization. For glancing incidence $F_{1,2}$ can be approximated by

$$F_{1,2} \approx \frac{\phi - f_2}{\phi + f_2} = \frac{f_1 - f_2}{f_1 + f_2}. \tag{76}$$

where $f_1 = \phi$. Within this approximation there is no distinction between the σ and the π components of the polarization[81]. Then the intensity ratio is,

$$\frac{I_r}{I_0} = \left| \frac{\mathbf{E}_1^R}{\mathbf{E}_1} \right|^2 = \frac{(\phi - A)^2 + B^2}{(\phi + A)^2 + B^2} \tag{77}$$

where,

$$A = \frac{1}{\sqrt{2}} \{ [(\phi^2 - \phi_c^2)^2 + 4\beta_2^2]^{\frac{1}{2}} + (\phi^2 - \phi_c^2) \}^{\frac{1}{2}} \tag{78}$$

$$B = \frac{1}{\sqrt{2}} \{ [(\phi^2 - \phi_c^2)^2 + 4\beta_2^2]^{\frac{1}{2}} - (\phi^2 - \phi_c^2) \}^{\frac{1}{2}} \tag{79}$$

$$\tag{80}$$

and ϕ_c is the critical glancing angle.

The depth $z_{1/e}$ at which the intensity is reduced to $1/e$ is obtained from the expression for the refracted beam (equation 74). The penetration depth is

$$z_{1/e} = \frac{\lambda}{4\pi B} \tag{81}$$

Calculations performed for Cu by Parratt[81] indicate that the penetration depth is of the order 20 to 50Å for glancing angles up to the critical angle depending upon the energy. For an air-Au interface with a glancing angle of incidence equal to 5mrad, $z_{1/e} = 16$Å. The values for δ and β were computed for $\lambda = 1.319$Å (9400eV) using the program by Cromer and Liberman[83]. They have calculated Dirac-Fock-Slater continuum oscillator strength distributions and anomalous atomic scattering factors within a relativistic formulation but neglected damping effects.

The analysis can be generalized for N stratified homogeneous media having smooth surfaces. If the amplitude factor for half the perpendicular depth is defined as

$$a_n = \exp\left(-ik_1 f_n \frac{d_n}{2}\right) \tag{82}$$

and the electric vectors at the half way point through medium $n-1$ and n are $\mathbf{E}_{n-1}$, $\mathbf{E}^R_{n-1}$ and $\mathbf{E}_n$, $\mathbf{E}^R_n$ respectively then from the continuity of the tangential components of the electric vectors the following expressions are obtained

$$a_{n-1}\mathbf{E}_{n-1} + a^{-1}_{n-1}\mathbf{E}^R_{n-1} \;=\; a^{-1}_n\mathbf{E}_n + a_n\mathbf{E}^R_n \tag{83}$$

$$(a_{n-1}\mathbf{E}_{n-1} - a_{n-1}^{-1}\mathbf{E}_{n-1}^{R})f_{n-1} = (a_n^{-1}\mathbf{E}_n - a_n\mathbf{E}_n^{R})f_n \quad (84)$$

The solution of these two equation can be written in the form of a recursion formula

$$R_{n-1,n} = a_{n-1}^4 \left[\frac{R_{n,n+1} + F_{n-1,n}}{R_{n,n+1}F_{n-1,n} + 1}\right] \quad (85)$$

where

$$R_{n,n+1} = a_n^2\left(\frac{\mathbf{E}_n^R}{\mathbf{E}_n}\right) \quad (86)$$

$$F_{n-1,n} = \frac{f_{n-1} - f_n}{f_{n-1} + f_n} \quad (87)$$

$$f_n = (\phi^2 - 2\delta_n - 2i\beta_n)^{\frac{1}{2}} \quad (88)$$

Note that for the bottom medium, the substrate, the thickness is infinite. For the first medium the thickness is taken as zero, thus making $a_1 = 1$. Starting from the bottom interface the recursion relation can be used to compute the reflectivity at each interface.

6.2 Experimental Aspects

The experimental arrangement is shown schematically in figure 42. The experiments were done at the Stanford Synchrotron Radiation Laboratory (SSRL) on a wiggler side station, beamline IV-1. The x-ray beam from the synchrotron source was collimated by an entrance slit with vertical aperture of 2mm. Then the beam passed through the same double Si(111) crystal monochromator as used in the Terfenol-D experiments. After the monochromator, the beam passed

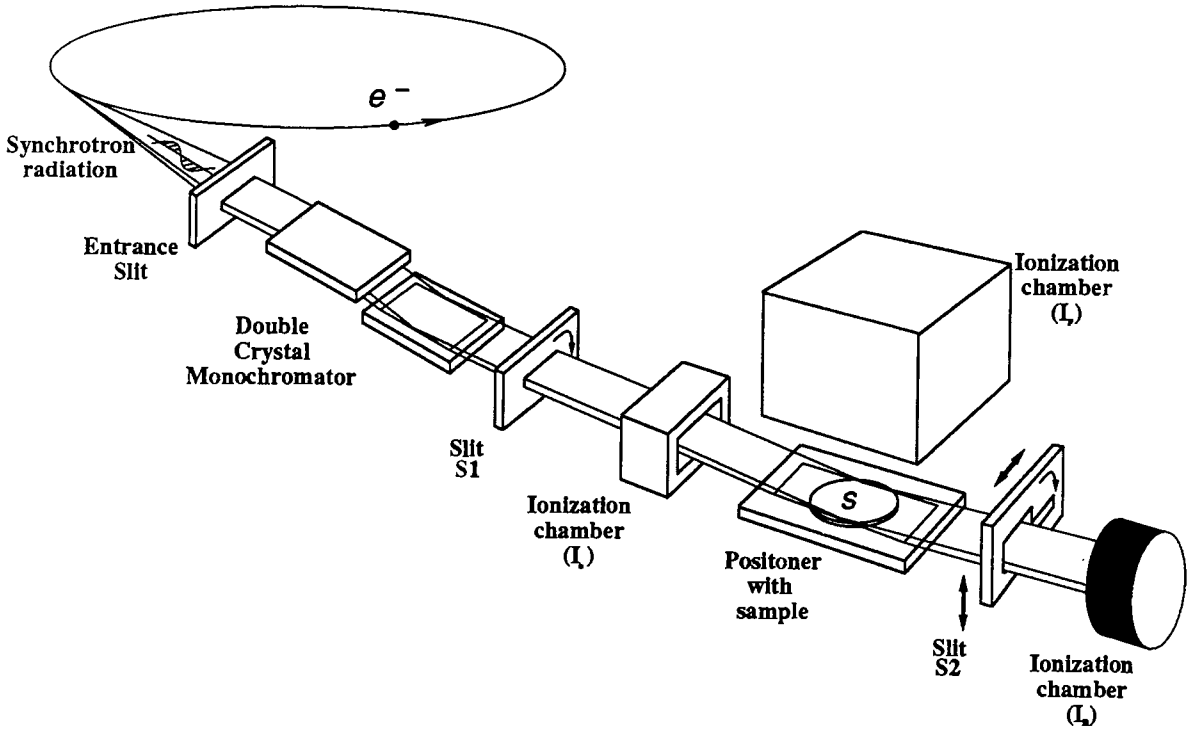

Figure 42: Experimental setup for glancing incidence XAFS. (Note the sample and fluorescence chamber are reversed by 180° (i.e. the sample should be facing down and the fluorescence chamber should be below the sample). It was drawn this way for clarity.

though a Huber slit whose aperture could be varied vertically and horizontally. The slit was mounted on a stage which could be rotated to adjust the tilt angle of the slit with respect to the x-ray beam. The mount was driven by a motor micrometer capable of 4μrad steps. This way the x-ray beam could be made parallel to the sample surface. Just beyond this slit the incident beam intensity was measured with a standard SSRL 6″ ionization chamber. At the exit of the ionization chamber the beam impinged on the surface of the crystal at an angle of a few mrad.

The sample was mounted on a brass plate attached to a 40Hz rotation stage, e (see figure 43). This stage was mounted on a positioner constructed especially for XAFS measurements in the glancing angle geometry, with synchrotron radiation in the hard x-ray region [84], [64]. The platform, a, is an aluminium plate 30cm in length and 10cm in width and the sample mount is located at its center. The platform sits on two micrometers, b, (40 turns/inch), one at each end. These micrometers are each attached to an aluminium disc, c, whose diameter is 3.5cm. The discs are in turn linked to another disc of identical dimension through three posts. The bottom disc is attached to a stepping motor, d, (200 steps/turn). The double disc assembly was designed to minimize the backlash. The stepping motors are electronically controlled by a NEC PC 8201A computer. The micrometer/stepping motor control the translational motion of the

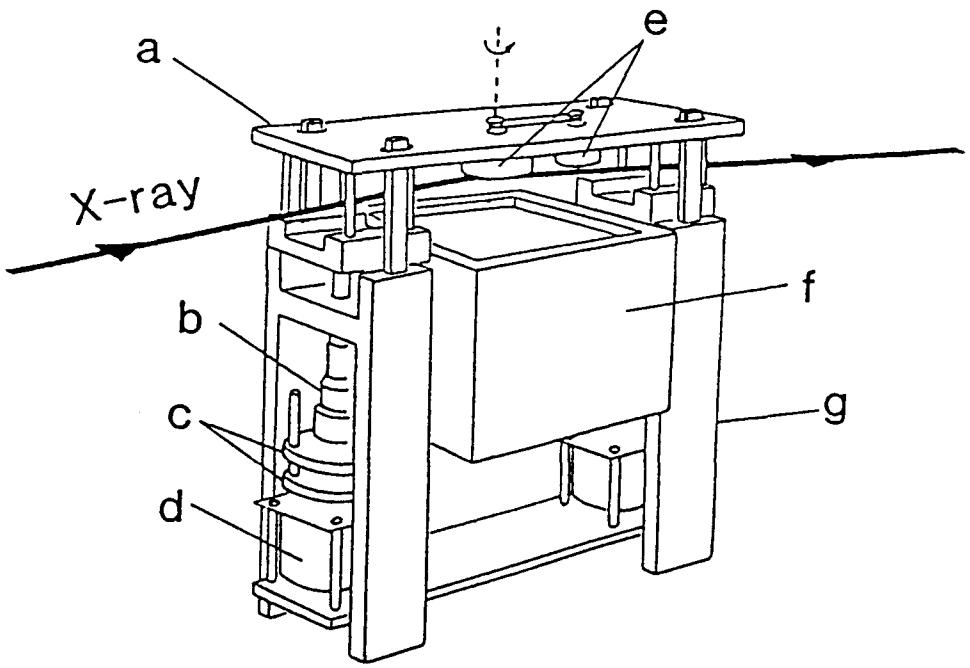

Figure 43: Sample positioner for glancing incidence XAFS: a-platform; b- micrometer; c-transmission discs; d-stepping motors; e-rotation stage and its driving motor; f-ion chamber for fluorescence; g-the stand. [84],[64]

platform in the up-down direction. The platform can be tilted relative to the incident beam in angular steps of 13.5μrad. Four rectangular brass posts located on the corners of the platform are guides to prevent the platform from tipping. All these parts are mounted on an aluminium frame. Four springs at each corner of the platform provide the restoring force to keep the platform in contact with the micrometer tips at all times. The positioner can also be turned 90^0 to permit the perpendicular geometry where the electric vector of the x-ray beam from the monochromator is at right angles to the surface of the sample.

An ionization chamber for fluorescence with a large aperture was used for these experiments. It is shown schematically in figure 44[64]. This chamber,

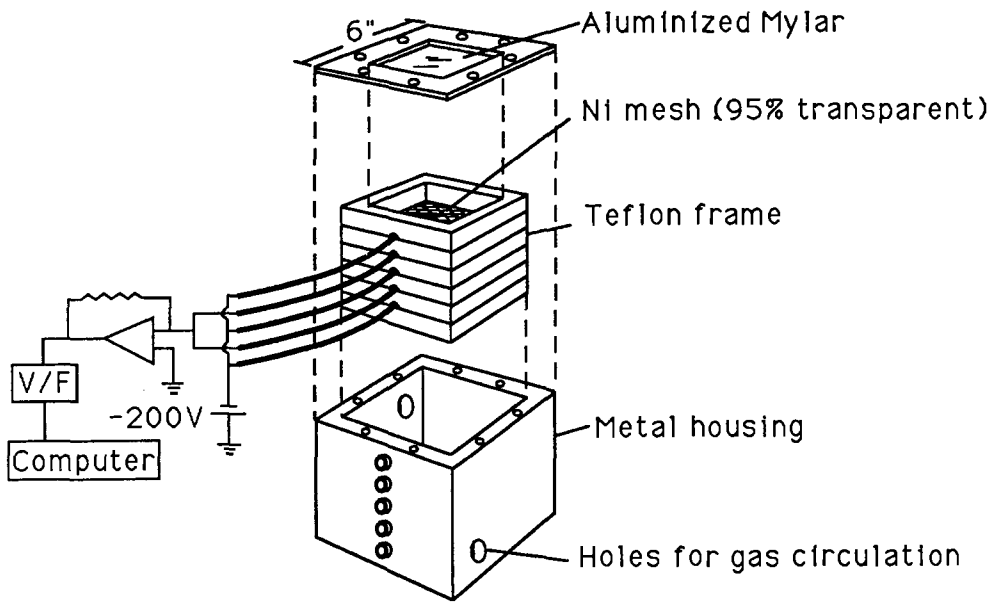

Figure 44: Schematic view of fluorescence chamber.

mounted on a computer controlled positioner with vertical and horizontal translational motion, fitted between the two posts of the positioner. The top surface of the chamber was approximately 5cm from the sample surface.

Another chamber whose construction is the same as the fluorescence chamber except for the cylindrical shape was used for reflectivity measurements. It too was mounted on a computer-controlled positioner with vertical and horizontal translational motion. It was placed approximately 60cm from the central axis of the sample. A second slit was positioned immediately in front of the reflectivity chamber on the same positioner. As for the first slit, it was mounted on a transverse rotation stage. The purpose of the two slits was to define the beam path.

6.2.1 Alignment Procedures

The first task was to ensure that the normal to the sample surface was parallel with the axis of rotation of the rotation stage on the sample positioner. This was done by mounting the sample, shining a He-Ne laser on the surface at an angle of approximately 20^0 from the surface and looking at the reflection at a distance of 6m. The sample was rotated twice by about 120^0 and the position of the reflected spot marked. If the normal to the sample and positioner were collinear then the reflected spot from the three orientations would appear at the same position. If it is not, three screws on the sample mount were adjusted until parallelism was achieved to within .4mrad. The positioner was then placed on the beamline.

The aperture of the first slit was set at 100μm high and 6mm wide, when the sample normal was parallel to the electric field vector. In the perpendicular orientation the aperture was set to 100μm wide and 1.5mm high. The wedge angle between the sample and slit S1 must be reduced to zero. To accomplish this the sample positioned in the path of the beam was tilted by some angle, ϕ, such that both the reflected and the straight through beam were seen on the ZnS fluorescent screen located in front of the second slit S2. S1 was rotated until the wedge angle was minimized.

To define the beam path, the sample was moved out of the beam in order to

permit the adjustment of S2. The parallelism of the two slits was obtained by maximizing the signal recorded by the reflectivity chamber. To achieve this the slit could be moved vertically and rotated if necessary. With the beam stop side of slit S2 put in the beam path, S2 was lowered in the beam until the reflectivity signal was composed of only 1% of the direct beam.

To set the sample at the $\phi = 0$ position the sample was lowered (moved towards the fluorescence detector (see fig. 43)) into the path of the beam. If $\phi \leq 0$ then the sample would block the direct beam and I_R would decrease. Conversely if $\phi > 0$ then I_R would increase. The sample was lowered and tilted in an iterative manner until the minimum angle producing a reflected beam was found and this was defined as the $\phi = 0$ position.

A plot of the reflectivity and the fluorescent signals as a function of glancing incident angle was measured to aid in the determination of the glancing critical angle. Figure 45 shows the plot obtained at 9400eV for the MBE sample with 8ML of Cu. It has been previously reported[64] that the effects on the amplitude and phase of an EXAFS spectra due to anomalous dispersion effects are negligible if the scans are taken at $\phi < \phi_c$ for thin (< 50Å) samples. In these experiments the EXAFS scans were all collected at approximately $.75\phi_c$.

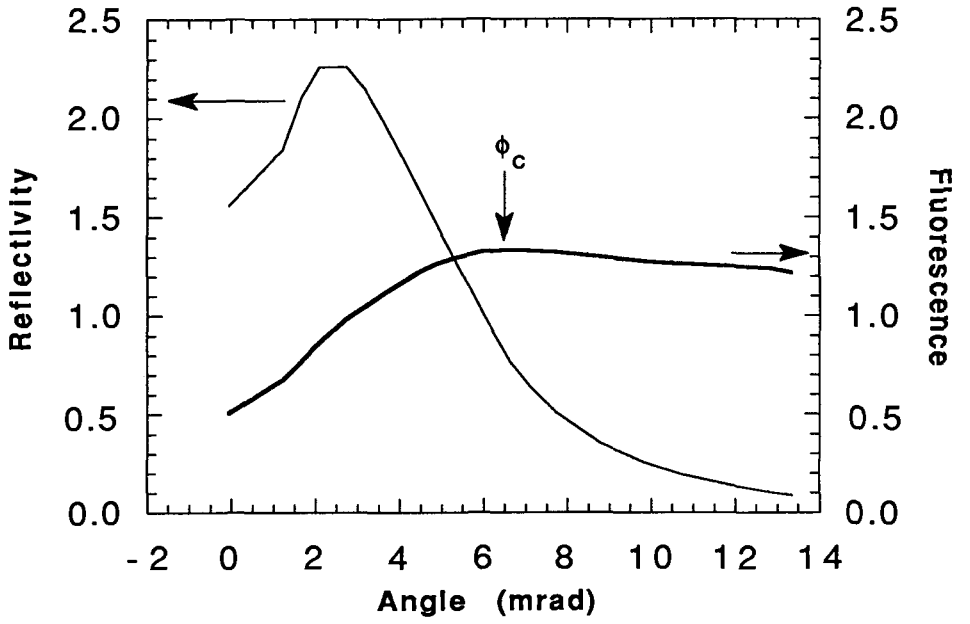

Figure 45: Plot of reflectivity and fluorescence as a function of incident angle.

6.2.2 Bragg Peaks Problem

In these experiments the absorption as a function of energy was measured. It is inevitable when working with single crystals for Bragg peaks to appear at various energies whenever Bragg's law is satisfied. These are detrimental to the collection of good EXAFS data. Some of the methods utilized to circumvent this problem include rotating the sample about the normal to the surface[85],[86], using a multi-channel fluorescence chamber to discriminate spatially diffraction peaks[87], using a high resolution detector to distinguish the fluorescent line and the higher energy diffraction line[88] and using total electron yield detection[89],[59]. A comparison[64] of the three detection modes, fluorescence, electron yield and reflectivity suggested that fluorescence was superior in the

sense that the XANES had less distortion, the signal-to-background (ratio between the edge jump height and the pre-edge background signal strength) was very good, the signal-to-noise was good and the signal was relatively insensitive to harmonics and glitches in I_0. Crystal glitches arise when the Bragg condition is fulfilled for more than one set of lattice planes simultaneously, which can only occur at discrete energies[91]. The one major drawback of the fluorescence technique was its sensitivity to Bragg peaks.

Figure 46 is a dramatic example of the severity of the problem in some cases. This is an EXAFS scan at the Au L_{III} edge (11919eV). The Bragg peaks even obscure the presence of the edge. Since the Bragg peaks appear only at specific energies governed by Bragg's law, these will enter the detector at a specific angle. Rotating the sample at 40Hz changed the Bragg angle so less diffracted energy entered the fluorescence detector. Although the Bragg signal became less than the amplitude of the EXAFS oscillations the residuals caused spurious contributions evident as shoulders in the magnitude of the Fourier transform. The solution was to leave the sample stationary but to mask the detector so that the photons associated with the Bragg peaks do not enter the detector. An aluminium frame to fit securely over the face of the fluorescence chamber was built. It was covered with a thin sheet of Mylar. A guide on each side of the frame permitted Polaroid film (type 57) to be inserted reproducibly. From

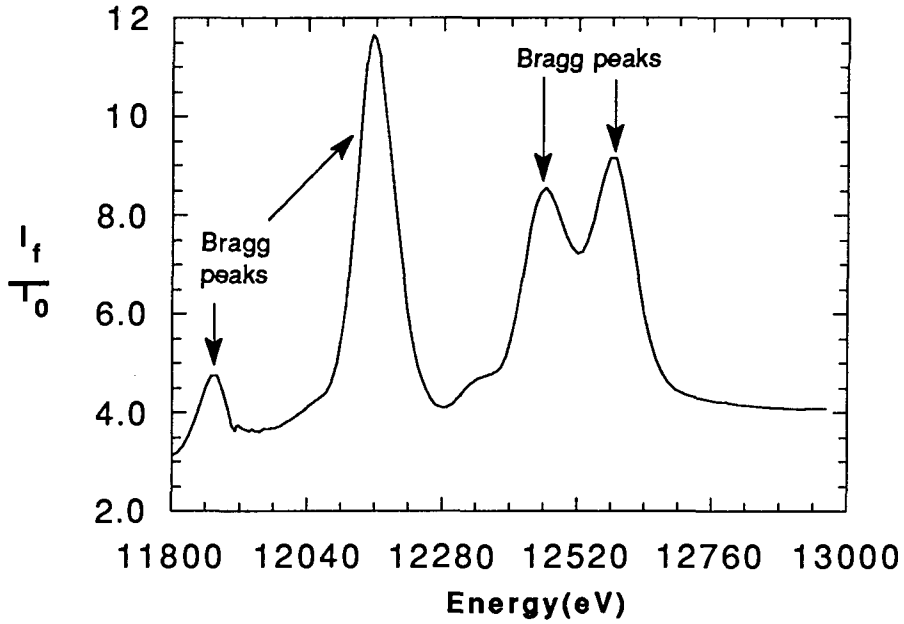

Figure 46: EXAFS scan at the Au L_{III} edge. The data is contaminated with Bragg peaks.

the scan in figure 46 the energies where Bragg peaks are located are easily identified. The monochromator was moved to one of these energies and the Polaroid film was exposed for times in the range 3 to 10min. All Bragg peak energies were done in succession and a photograph as shown in figure 47 was obtained. The Bragg peaks show up quite clearly. Lead tape was placed on the Mylar over the bright areas which marked the position of the Bragg peaks. Another photograph and the corresponding scan obtained after the masking of the Bragg peaks are shown in figures 48 and 49. The quality of the EXAFS data is poor here because the integration time was purposely reduced to speed up the collection time since the scan was simply used to check for the presence or absence of Bragg peaks. A quick scan up to 16.5Å^{-1} would take less than

Figure 47: Polaroid photograph of the Bragg peaks. The peaks are at 11874eV, 12156eV, 12462eV and 12585eV.

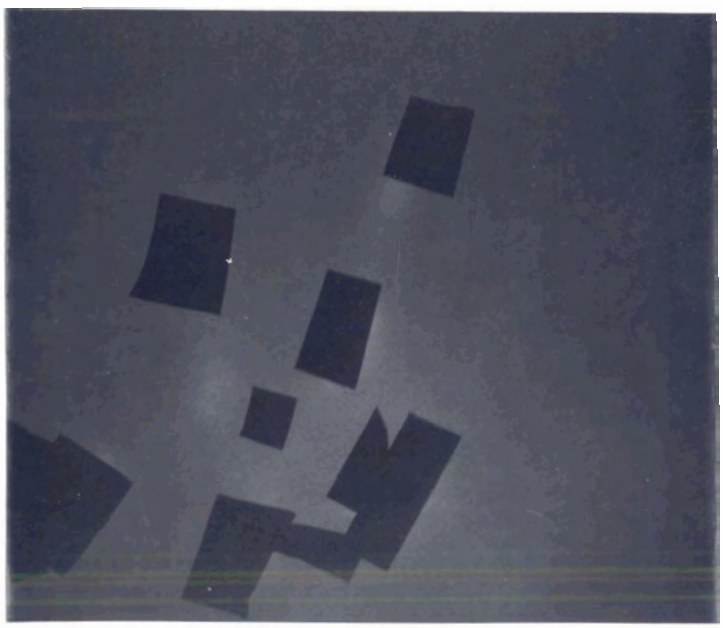

Figure 48: Polaroid photograph with the Bragg peaks masked.

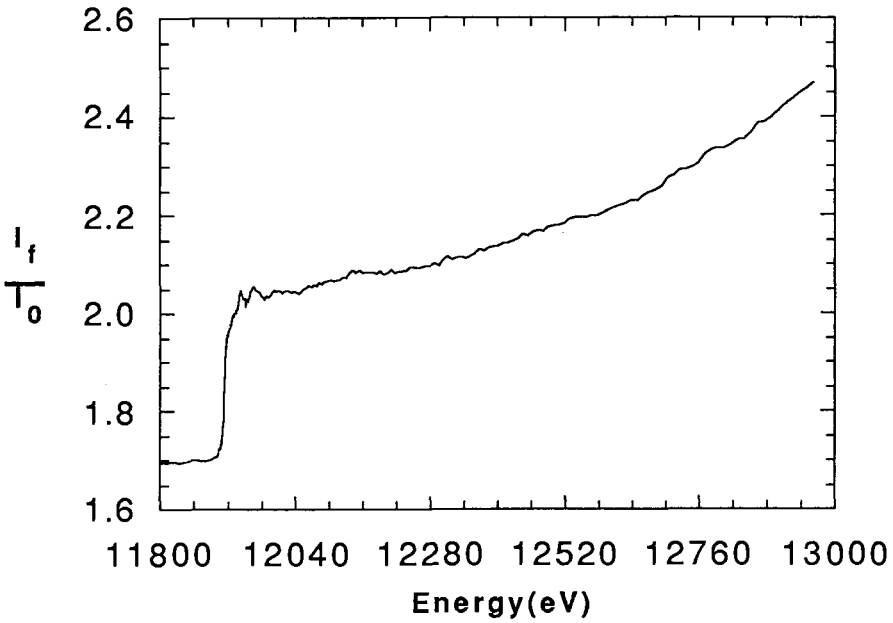

Figure 49: EXAFS scan at the Au L_{III} edge. Bragg peaks have been masked.

3 minutes to complete. Normally, for good quality data a scan of that length would take of the order of 15 to 20 minutes.

This technique of creating a mask for the detector is the inexpensive version of a multichannel fluorescence detector.

6.3 XAFS Analysis: Qualitative Discussion

For each sample the measurements were repeated several times to obtain better statistics. The measurements were averaged and Chauvenet's criterion[92] was used to eliminate the more deviant data sets. Chauvenet's criterion states that a a reading may be rejected if the probability of obtaining that particular deviation from the mean is less than $1/2n$, where n is the number of readings. For the 8ML data the average consists of 15 data sets. The standard deviation

	no. of averaged data sets	standard deviation ($\times 10^{-3}$)		
		8909.3eV	9100.5eV	9502.2eV
8ML $\mathbf{E}_{\parallel}$	15	5.23	5.65	5.57
8ML $\mathbf{E}_{\perp}$	14	1.31	2.04	0.70
14ML $\mathbf{E}_{\parallel}$	13	1.33	4.11	5.29
14ML $\mathbf{E}_{\perp}$	15	1.49	3.69	4.06
20ML $\mathbf{E}_{\parallel}$	8	2.27	13.7	18.5
20ML $\mathbf{E}_{\perp}$	10	2.31	9.67	9.61

Table 9: The number of data sets averaged and the associated average standard deviation of each data point for each sample in the two orientations, $\mathbf{E}_{\parallel}$ to the surface of the substrate and $\mathbf{E}_{\perp}$ to the surface of the substrate.

at each data point was calculated. Table 9 gives the number of data sets that were averaged and the standard deviation at three energies corresponding to a point before the edge, one just above the edge and the last one close to the end of a typical scan. The designation of $\mathbf{E}_{\parallel}$ and $\mathbf{E}_{\perp}$ indicates the orientation of the electric field vector with respect to the surface of the substrate.

The background removal was done as described previously for Terfenol-D. To find the edge energy the derivative of the data between 8974eV and 8982eV (the region between the onset of the absorption jump and the characteristic Cu dip) was taken. The maximum in the derivative corresponds to the first inflection point. The two points at half the maximum value were determined and the edge energy was set at the value midway between these two points. Error bars of the edge energy can be estimated from half the smallest energy step. In the edge region data were collected in steps of .52eV. Therefore the error associated with

the edge energy was .26eV in all cases except the 14ML $\mathbf{E}_{\|}$ where it was .48eV because the data were collected at larger energy intervals. The point where the edge jump starts needs to be determined to get the height of the jump. This was evaluated using the construction of figure 5. A straight line was fit between 25eV and 200eV above the edge and this line was extrapolated to the edge energy to give the height of the jump. The background was estimated by a polynomial of 10^{th} order and in some cases 11^{th} order, which was subtracted from the data.

The EXAFS interference function obtained is shown in figure 50 along with the EXAFS of bulk Cu and bulk Fe measured in transmission mode. For bcc Fe there are two peaks between 4.25Å^{-1} and 5.75Å^{-1} whereas for fcc Cu only one broad peak occurs in this region. The 8ML data in both orientations has two clearly distinguishable peaks in this region, hence a more bcc-like signature than fcc. The same is true of the 14ML data. The 8ML data has weak oscillations on a broader background in the 2.5 to 4.25Å^{-1} range. In this region Fe has a broad hump-like feature and fcc Cu has one sharp peak. Overall, the features of the 8ML appear more closely related to the bcc Fe than the fcc Cu. The features of the 14ML in the parallel configuration are very similar to the 8ML data sets. The 14ML data taken in the perpendicular mode is different. In this case, as for the 8ML, the bcc-like features between 4.25Å^{-1} and 5.65Å^{-1} are still

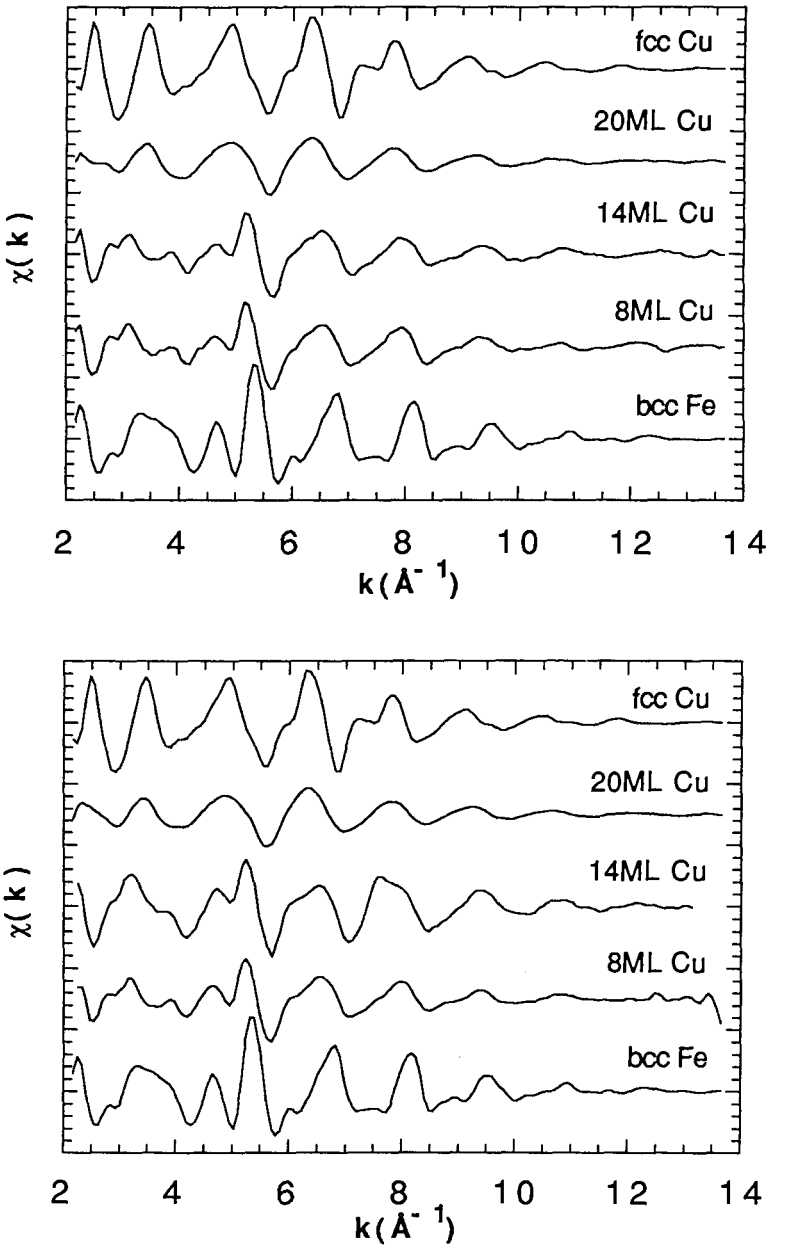

Figure 50: XAFS $\chi(k)$ for MBE grown Cu with thicknesses 8ML, 14ML and 20ML. The range of the data is 2.2-13.7Å^{-1} in all cases except the 14ML $\mathbf{E}_{\perp}$ case where the range is 2.2-13.1Å^{-1}. The upper graph is for the data collected with $\mathbf{E}$ parallel to the surface of the substrate and lower graph is for data collected with $\mathbf{E}$ perpendicular to the surface of the substrate.

visible but the region between 2.75 and 4.25Å^{-1} clearly differs from the parallel configuration. In the 20 ML data features in $\chi(k)$ seem to be predominantly fcc in origin.

The differences or similarities are more marked in the Fourier transform of the $\chi(k)$. Figure 51 shows the Fourier transform of the data of figure 50. Before the Fourier transform is taken $\chi(k)$ is multiplied by k. This enhances the high k region of the data and diminishes the low k region resulting in the treatment of the full range of the data being on approximately the same footing. The Fourier transform of the 8ML Cu compared with the Fourier transform of bcc Fe clearly demonstrates the bcc nature of the 8ML of Cu. The presence of the higher peaks also indicates an ordered structure but the reduction in amplitude suggests a larger local disorder than found in bcc Fe. Cu thicknesses of 14ML show large differences between the in-plane and out-of-plane directions. The data parallel to the surface still retain bcc–like features but the degree of disorder has increased markedly. In the perpendicular direction the features are more a mixture of the two phases, fcc and bcc. The thin films of Cu 20ML thick have essentially one main peak, the higher peaks being practically non-existent. This marks a highly disordered state relative to both bcc and fcc structures beyond the first peak. The main peak is shifted towards the fcc position suggesting a local structure closer to fcc than bcc.

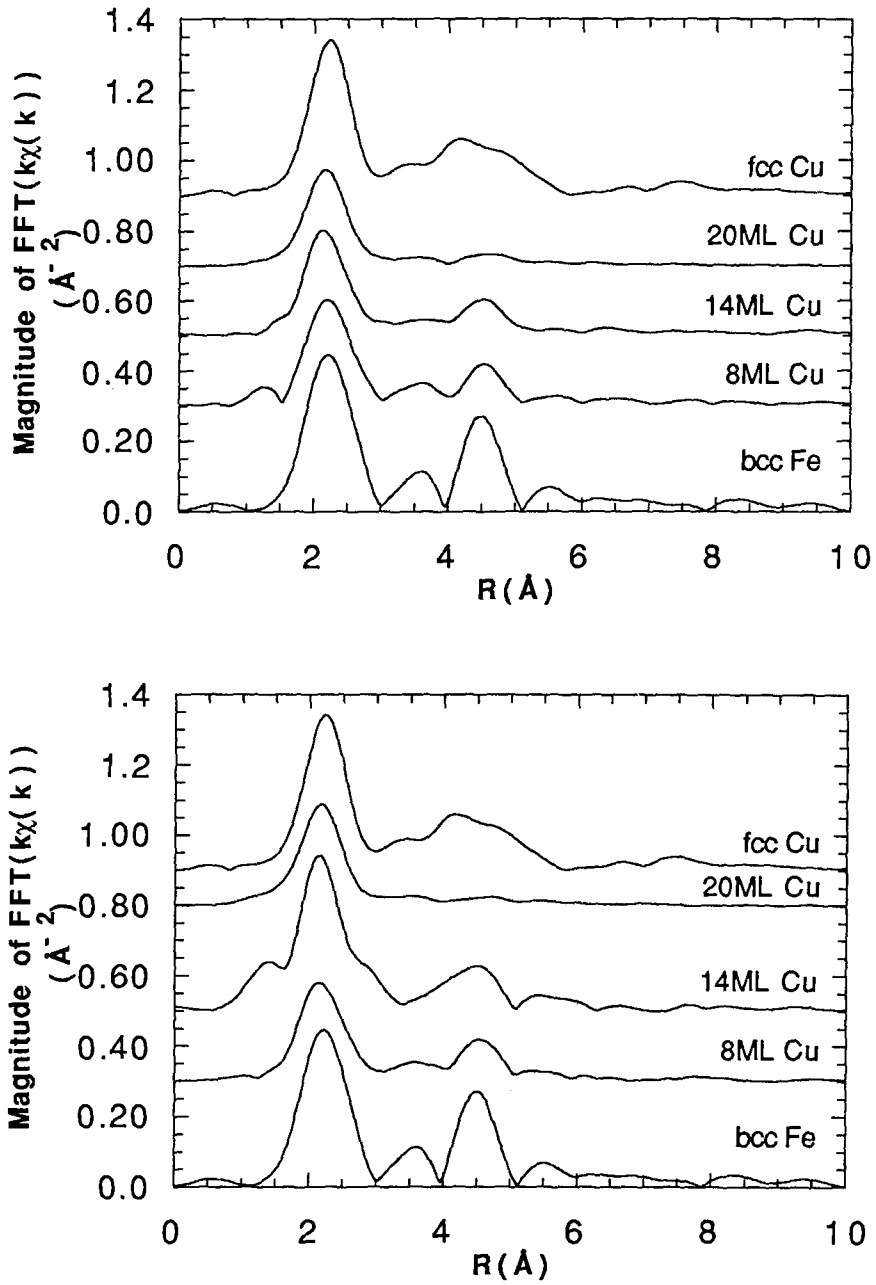

Figure 51: Fourier transform of $k\chi(k)$ for MBE grown Cu with thicknesses 8ML, 14ML and 20ML. The range of the data used for the transform is 2.33-13.13Å^{-1} in all cases. A Hamming window was applied. The top graph is for the data collected parallel to the surface of the substrate and on the bottom graph is for data collected perpendicular to the surface of the substrate.

6.3.1 X-ray Near Edge Structure

Only qualitative information based on the X-ray near edge structure (XANES) features will be discussed. Figure 52 shows the XANES of the Cu data. The graph at the top is for the electric vector of the radiation parallel to the substrate and the bottom one is for the perpendicular orientation. The XANES of fcc Cu and bcc Fe are also displayed on these graphs for ease of comparison. The data were prepared by subtracting a linear fit to the pre-edge background and then normalizing to the linear fit above the edge. In all the data taken in the $\mathbf{E}_{\|}$ mode the dip which occurs at approximately 5eV above the edge is more pronounced. This is a characteristic of fcc Cu. In the perpendicular mode it is more like Fe. In terms of the peak positions, all MBE Cu have a first maximum at approximately 20eV above the edge. This corresponds to the first maximum of bcc Fe and the first minimum of fcc Cu. Fe also has a shoulder at $\sim$10eV which is present in the 8ML and 14ML data sets. For the 20ML data, the shoulder and the first peak seem to have merged together. The 20ML data also differs from the other two regarding a peak at approximately 47eV which corresponds to a fcc Cu peak. In this region bcc Fe has a broad hump that peaks at about 41eV. The 8ML and the 14ML do not have a hump but have a couple of small oscillations in the 35 to 50eV range. At 47eV where fcc Cu and the 20ML MBE Cu peak the 8ML and the 14ML have a minimum. The data

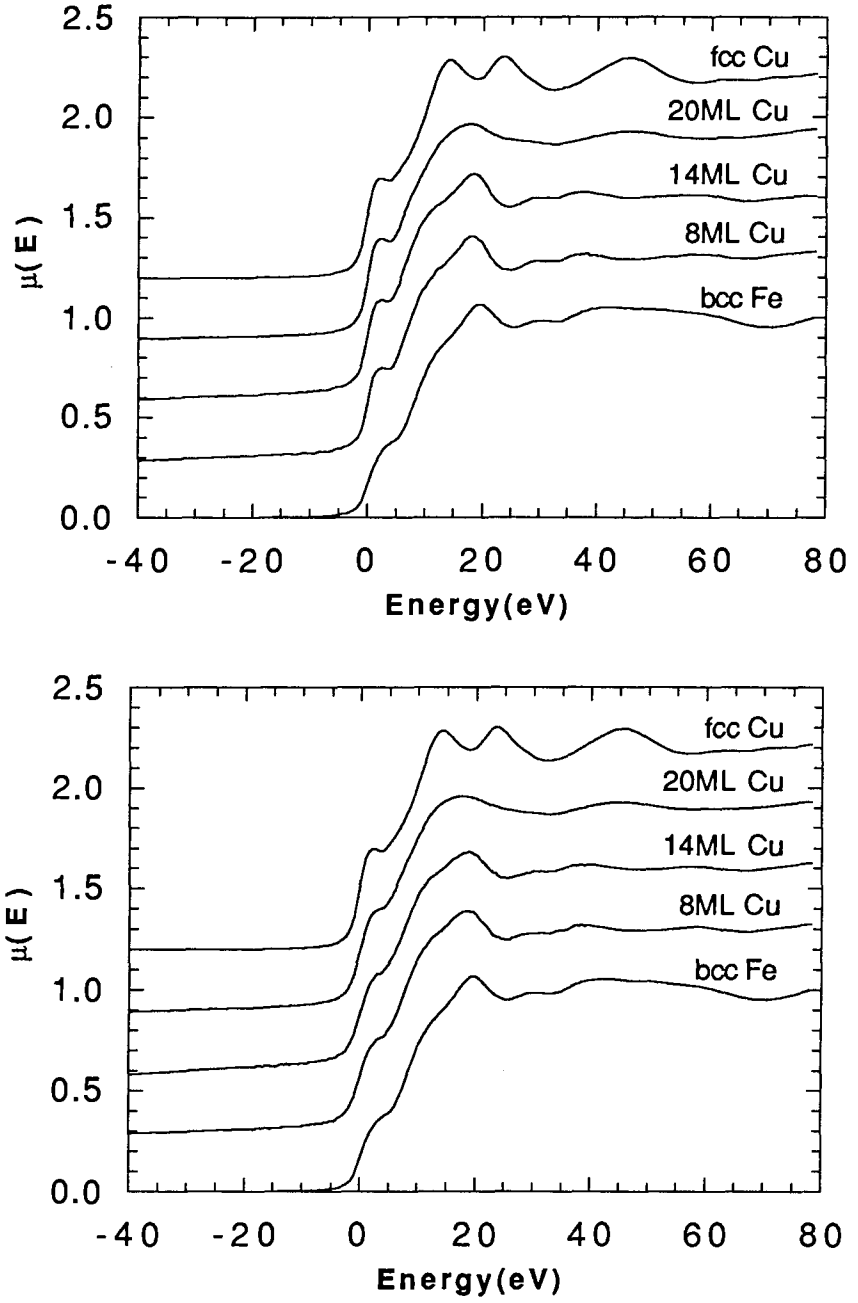

Figure 52: XANES of MBE Cu. XANES of bcc Fe, 8ML Cu, 14ML Cu, 20 ML Cu and fcc Cu. Data for the MBE films in the top graph were taken with $\mathbf{E}_{\parallel}$ to the surface of the substrate and in the bottom graph with $\mathbf{E}_{\perp}$.

using **E** perpendicular to the surface are similar to the corresponding data with **E** parallel to the surface except perhaps in the 14ML data where the shoulder at around 10eV is shifted closer to the first peak. The XANES of 8ML Cu grown by MBE on Ag(001) showed a large hump[25] similar to what is found at 20ML in this work but did not show the peak at 47eV. The 8ML Cu on Ag(001) were found to be body-centered with a 7.6% vertical expansion[25].

The XANES clearly demonstrate the close similarity of the MBE grown Cu with bcc Fe. It is only in the 20ML that evidence of an fcc phase appears.

6.3.2 EXAFS Results for 10 Au/5 Fe/8 Cu/8 Fe/Ag(001)

The 8ML data taken with **E** parallel and perpendicular to the surface of the substrate have a very similar signature. The closeness of this resemblance will determine if the structure is cubic or distorted. An overlay of the Fourier transform for the two orientations is shown in figure 53. A very small difference, $\approx$ .06Å in the main peak position can be detected and the height is clearly different. Note how closely the peaks at $\approx$4.5Å are matched compared to the main peak.

If the structure is bcc-like the main peak has two closely spaced shells under it. For example the first two shells of bcc Fe are at 2.485 and 2.87Å, a difference in R of .385Å which is not resolvable with the FFT. On the other hand fcc Cu's first two shells occur at 2.55Å and 3.61Å and are easily resolvable.

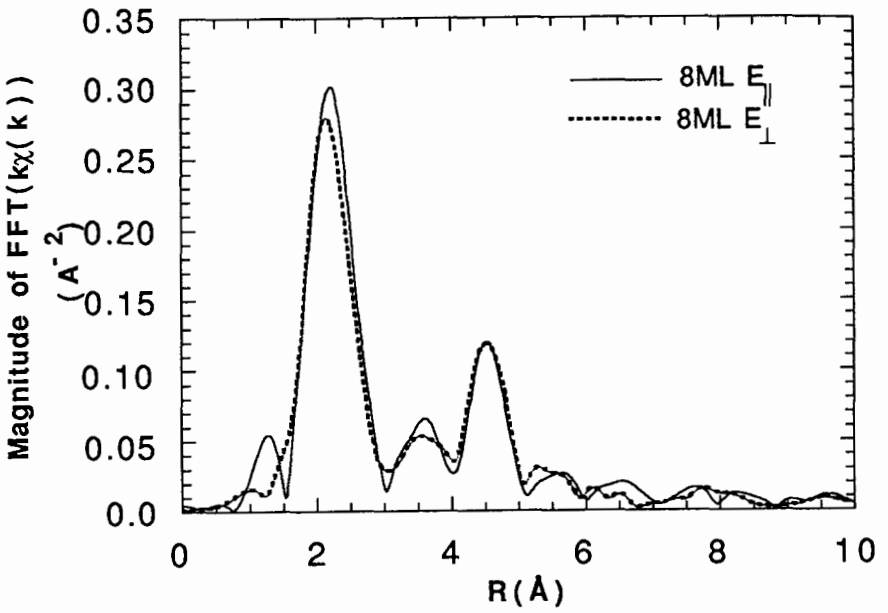

Figure 53: Fourier transform of $k\chi(k)$ for MBE films of Cu 8ML thick. Transform taken with a Hamming window over the range 2.33–13.13Å^{-1}.

Beating analysis of the 8ML $\mathbf{E}_{\|}$ and 8ML $\mathbf{E}_{\perp}$ was performed by Fourier filtering the main peak and taking the derivative of the phase extracted from the inverse Fourier transform. The derivative of the phase for both cases is plotted in figure 54. Various windows can be used for the Fourier transform. Each curve represents the derivative of the phase for the data that has been Fourier transformed with a 10% Gaussian, a Hamming, a Hanning and a rectangular window as indicated in the figure. The rectangular window is imposed by the finite range of the data and is inherent to it. The computational application of a window function should not significantly affect the position of a real beat node. To verify this statement beating analysis on a known system, bcc Fe, was performed (see figure 8). The range of the data for this test was the same

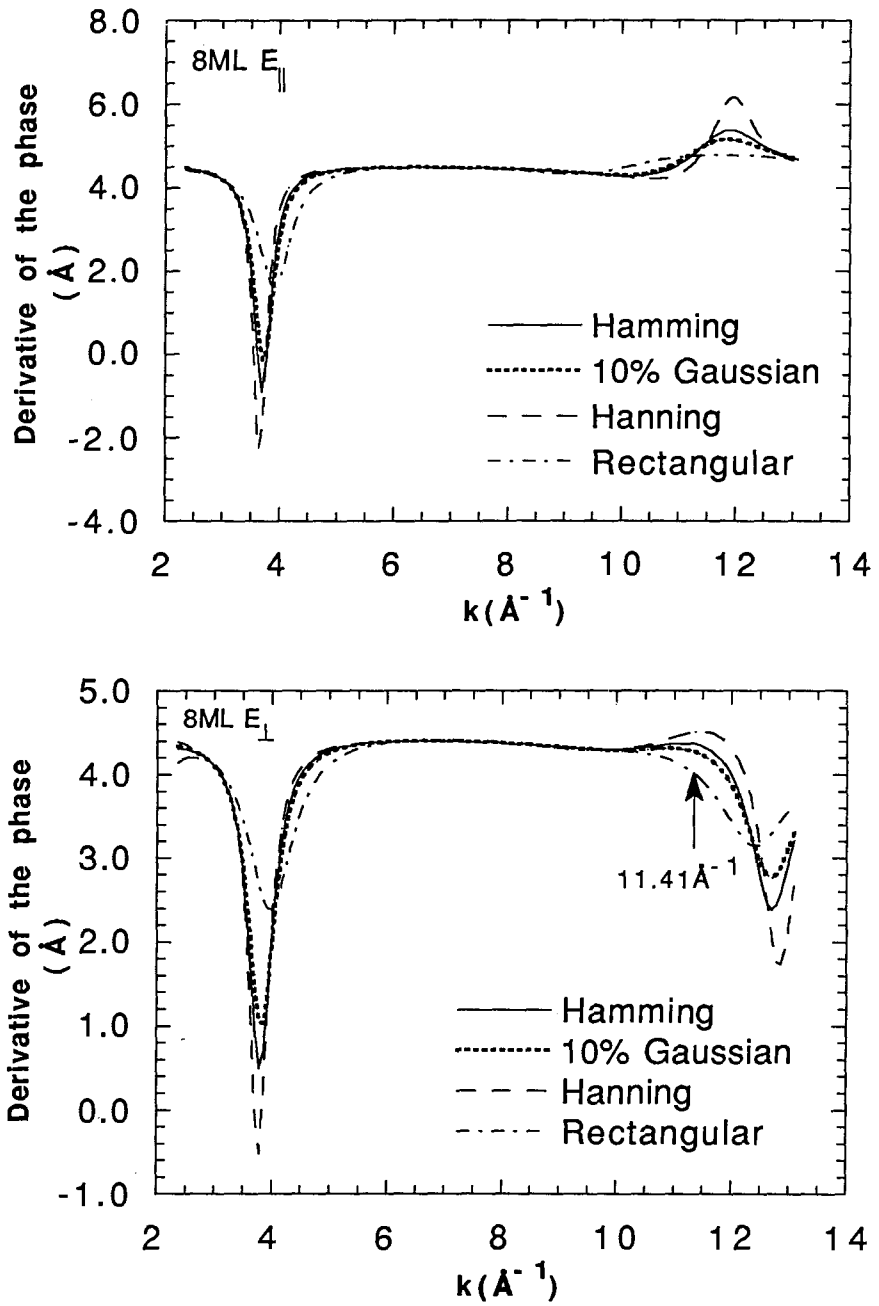

Figure 54: Derivative of the phase of main peak for 8ML data. The top graph is the $\mathbf{E}_{\|}$ data and the bottom graph is the $\mathbf{E}_{\perp}$ data. In both cases the Fourier transform was taken over the range 2.33–13.13Å^{-1}. Each curve is for the application of a different window, as indicated in the figure, for the Fourier transform. The window was removed from the inverse transform which was taken over the range 1.53-2.97Å.

as used for the thin films, 2.33 to 13.13Å^{-1} and the various windows as used in the 8ML cases were used. The beat frequency, ΔR for the first node can be extracted in each case (excluding the rectangular window) and the average gives $\Delta R = .393 \pm .004$ which differs from the actual value of .385 by $\sim$2%. The same result is obtained for the second node. Applying the same technique of averaging the ΔR for the first node to the 8ML $\mathbf{E}_{\|}$ data in top portion of figure 54 gives $\Delta R = .425 \pm .003$Å. The second node should occur at 11.09Å^{-1} which is not clearly evident in this figure. One must keep in mind that the Fourier filtering procedure by throwing away data outside the range of the main peak, is in fact not using all the components associated with the main peak which are in the form of excluded sidelobes and produces additional artifacts in k-space. The transform artifacts affect more severely the ends of the data.

The derivative of the phase for the 8ML data taken with $\mathbf{E}$ perpendicular to the surface is shown in the bottom half of figure 54. From the first dip the average ΔR is .413±.002Å. The next beat is expected at 11.41Å^{-1}. A small peak is present at this location. The presence of these two extrema associated with the beat frequency $\Delta R = .413$Å confirms the existence of 2 shells under the main peak. The noteworthy point here is that $\Delta R = R_2 - R_1$ in both orientations is larger than for bcc Fe suggesting an expansion of the Cu with respect to the Fe bcc lattice.

Non-linear least square fitting as described in section 2.2.4 was applied to the data for both cases individually. Amplitudes and phases extracted from Cu data taken in transmission were used. This permits the assumption that E_0 and the mean free path terms are identical for the reference and the unknown since they were both analysed by the same method. The amplitude has the term $\frac{kR^2}{N}$ removed and the $2kR$ term was subtracted from the phase. The crystallographic values $R = 2.5527$Å and $N = 12$ were employed for this purpose. Note that the Debye–Waller term is still present in the amplitude term, hence all Debye–Waller terms obtained from the fits are relative to the fcc Cu Debye–Waller term,

$$\Delta\sigma_1^2 = \sigma^2_{MBE\ Cu} - \sigma^2_{fcc\ Cu} \tag{89}$$

For the fits the data and the reference were processed in the same way. The Fourier transform was done over the range of 2.33–13.13Å^{-1} with a Hamming window.

The fits were done in R-space to avoid the additional artifacts incorporated in the data by Fourier filtering. The fits extended from 1.53 to 2.97Å, the range of the main peak. The results are compiled in table 10. The quality of the fit is judged from χ^2 as given in equation 35. This fit gave a $\chi^2 = .59 \times 10^{-4}$. The error bars are determined from plotting the variable for which the error bars are sought as a function of χ^2 while keeping all other variables constant. The

R_1	$\Delta\sigma_1^2$	N_1	ΔR	$\Delta\sigma_2^2$	$\frac{N_2}{N_1}$
2.503	-.0018	6.3	.406	.013	.9
$\pm$.004	$\pm$.0005	$\pm$.3	$\pm$.025	$^{-.003}_{+.005}$	$\pm$.3

Table 10: Curve fitting result for 8ML with $\mathbf{E}_{\|}$ to surface of the substrate. Fixed parameters were $a_1 = a_2 = 0$, $\Delta E_1 = \Delta E_2 = 0$.

points at $2\chi^2_{min}$ are defined as the errors. The nearest neighbor distance and the second nearest neighbor distance are both larger than the corresponding values for Fe. R_1 is larger by $\approx$ .7% and R_2 is larger by $\approx$ 1.4%. R_2 is the lattice constant a. From R_1 and a the vertical height in the c direction is calculated to be 2.85Å, a quantity that is .7% smaller than the lattice parameter of Fe, 2.87Å.

It was found that the correlations between coordination numbers and Debye-Waller factors within a given shell are quite large, typically 98% or higher. The correlations of these quantities are also of the same order of magnitude between the shells. These high correlations forbid any firm conclusion on the absolute value of either the coordination numbers or the Debye-Waller factors. To break the correlation another condition must be imposed on one of these variables. In a previous EXAFS study on sputtered Fe/Cu/Fe multilayers[65], the authors imposed the condition that $N_1 + N_2 = 14$. This is only true for the body centred structure. Therefore, such a condition assumes a model a priori. The assumption is consistent with the evidence presented in the previous chapters on

R_1	$\Delta\sigma_1^2$	N_1	ΔR	$\Delta\sigma_2^2$	$\frac{N_2}{N_1}$
2.490	-.0013	6.3	.385	.022	.9
$\pm$.007	$\pm$.0006		$^{+.061}_{-.058}$	$^{+.017}_{-.007}$	

Table 11: Curve fitting result for 8ML with $\mathbf{E}_\perp$ to the surface of the substrate. Fixed parameters were $a_1 = a_2 = 0$, $\Delta E_1 = \Delta E_2 = 0$, $N_1 = 6.3$ and $\frac{N_2}{N_1} = .9$

RHEED, XANES and the Fourier transform for the 8ML sample in this work. Fitting by imposing the bcc structure by fixing the coordination numbers $N_1 = 8$ and N_2=6 gives about the same values for R_1 as before when the N's are allowed to vary. The Debye-Waller factors and N's are strongly correlated so fixing one will cause a change in the other, which is observed. ΔR is decreased to .372 from .406. This suggest that the correlation between ΔR and one or both of the coordination numbers must be quite high. It is found for the conditions of table 10, that ΔR and N_1 are 96% correlated. The large error bar associated with ΔR is mostly a reflection of this correlation since this is included when the error bars are computed using the $2\chi^2_{min}$ method.

For the 8ML data with $\mathbf{E}_\perp$ it was assumed that the coordination numbers would not vary by more than the estimates of the errors obtained in the $\mathbf{E}_\parallel$ case. Therefore these were fixed to the same values obtained in the $\mathbf{E}_\parallel$ case. The solution obtained in this case is tabulated in table 11. The χ^2 was $.62\times10^{-4}$. The first nearest neighbor distance is only .2% larger than for bcc Fe. The ΔR is identical to what is found in Fe. The Debye-Waller factor of the second shell

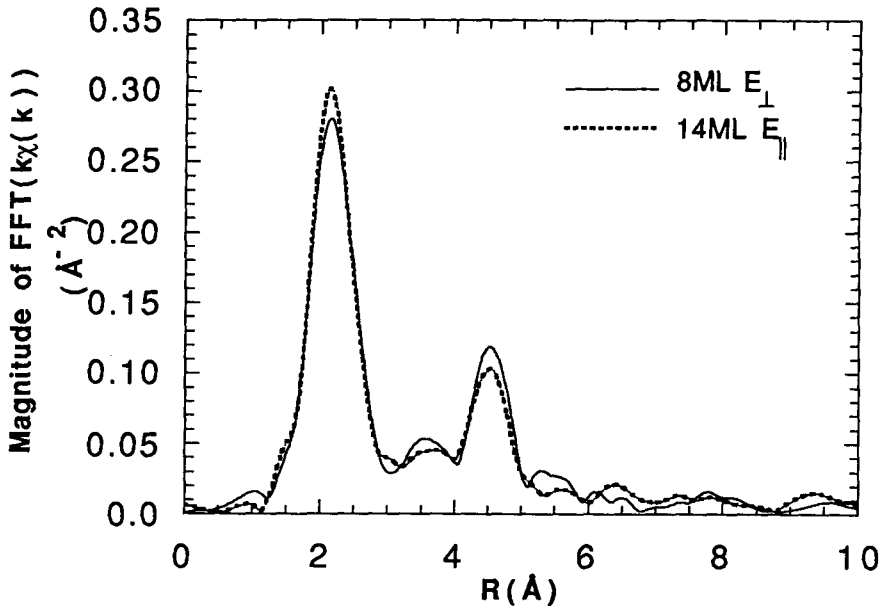

Figure 55: Overlay of Fourier transform of 8ML $\mathbf{E}_\perp$ and 14ML $\mathbf{E}_\parallel$. Range used for the $k\chi(k)$ transform was 2.33–13.13Å^{-1} with a Hamming window. The solid line is 8ML with $\mathbf{E}_\perp$ and the dashed line is 14ML with $\mathbf{E}_\parallel$.

is unusually large. If the fit is redone by letting the coordination numbers vary, R_1 does not change but N_1 becomes closer to the coordination number expected for a bcc structure. The values of the second shell suggest either this shell is not present or is extremely disordered.

6.3.3 EXAFS Results for 10 Au/5 Fe/14 Cu/8 Fe/Ag(001)

It is quite clear from the Fourier transforms (figure 51) that the data in the parallel and the perpendicular orientations are markedly different. The data in the parallel case is very similar to the data in the 8ML $\mathbf{E}_\perp$ orientation. The transforms of these two is overlayed in figure 55.

R_1	$\Delta\sigma_1^2$	N_1	ΔR	$\Delta\sigma_2^2$	$\frac{N_2}{N_1}$
2.493 $\pm$.006	-.0018 $\pm$.0007	6.3	.456	.0354	.9

Table 12: Curve fitting result for 14ML with $\mathbf{E}_{\|}$ to the surface of the substrate. Fixed parameters were $a_1 = a_2 = 0$, $\Delta E_1 = \Delta E_2 = 0$, $N_1 = 6.3$, $\frac{N_2}{N_1} = .9$

As for the 8ML data, non-linear least square fitting was performed in R-space over the range 1.53 to 2.97Å. Since the 14ML $\mathbf{E}_{\|}$ is so similar to the 8ML data the coordination numbers were fixed to the same values as for the 8ML data sets. The results of this fit are summarized in table 12 ($\chi^2 = .11 \times 10^{-3}$). R_1 is only .3% larger than the nearest neighbor distance in bcc Fe. The error bars for the second shell could not be determined because these parameters were not in "deep" enough minima to compute the $2\chi^2_{min}$. The second shell is either absent or highly disordered. In fact the solutions obtained for R_1, $\Delta\sigma_1^2$ and N_1 with a one shell fit are within the error bars obtained in a 2 shell fit.

The Fourier transform of the data taken in the perpendicular orientation has a rather large peak below 1.5Å (see figure 51). The origin of this peak is unknown. A shoulder is clearly evident on the high R side of the main peak suggesting perhaps the presence of a second shell. Beating analysis was done over the range 1.53 to 2.97Å (see figure 56) and the first dip in the derivative at $k = 3.6\text{Å}^{-1}$ reveals $\Delta R = .44 \pm .01$Å. The next beat should occur at 10.64Å^{-1} but it does not appear there. If the problem is reversed and the large peaks at

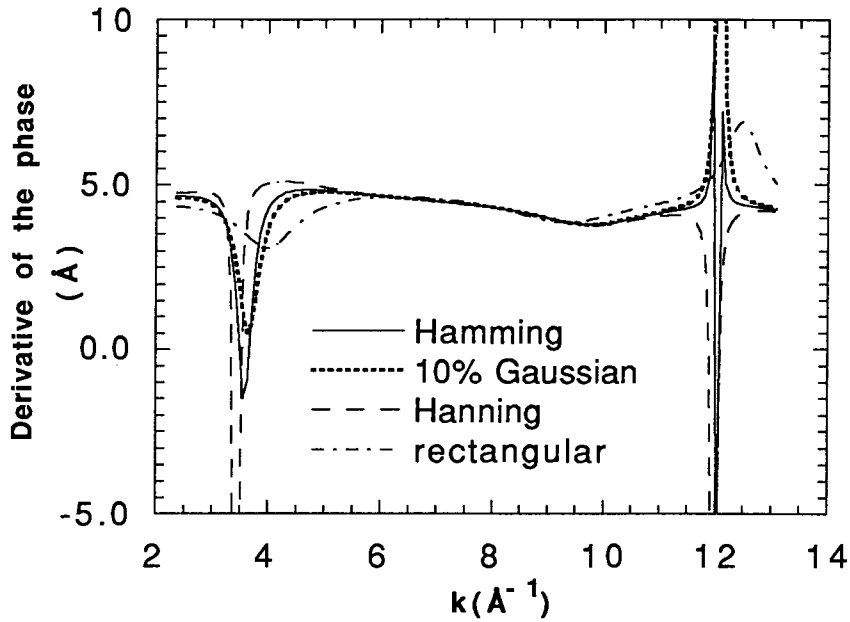

Figure 56: Derivative of the phase for 14ML $\mathbf{E}_\perp$. Fourier transform was done with a Hamming window over the range 2.33–13.13Å. Fourier filtering is from 1.53 to 2.97Å.

$\approx 12\text{Å}^{-1}$ are considered as the second beat then $\Delta R = .389 \pm .006$Å. From this the first node should occur at 4.03Å^{-1} which is not the case. This suggests that the peaks and dips observed in the derivative of the phase are not associated with a beat frequency and that the peak contains only one shell.

The result of a one shell fit over the same range as used in the 8ML and the 14ML $\mathbf{E}_\parallel$ cases is shown in table 13 for the 14ML $\mathbf{E}_\perp$. The measure of goodness of fit, χ^2 was $.22\times10^{-2}$, which is not very good. Any attempts at fitting the data with two shells gave extremely large values of $\Delta\sigma_2^2$ (and a large value of N_2/N_1 with which $\Delta\sigma_2^2$ is correlated) indicating a highly disordered shell or the absence of a second shell within the fitting range as indicated by the beating

R_1	$\Delta\sigma_1^2$	N_1
2.511	-.0057	6.05
$\pm$.018	$^{+.0027}_{-.0019}$	$\pm$1.65

Table 13: Curve fitting result for 14ML with $\mathbf{E}_\perp$ to the surface of the substrate. Fixed parameters were $a_1 = a_2 = 0$, $\Delta E_1 = \Delta E_2 = 0$.

analysis.

6.3.4 EXAFS Results for 10 Au/5 Fe/20 Cu/8 Fe/Ag(001)

The first thing to note is that there is apparently only one main peak in the 20ML data sets. Evidence of higher order shells is greatly suppressed. Even the magnitude of the main peak is reduced compared to both bcc Fe and fcc Cu. This indicates a lower coordination number or greater disorder in the system. A closer look at the higher order shells is shown in figure 57 where the data from 2.8Å to 10Å has been multiplied by a factor of 5 and then overlayed on the bcc Fe transform. The higher shells still have some bcc-like characteristics.

The first test is to determine how many shells are under the main peak. This is done with a beating analysis as described previously. The main peak is extracted by the Fourier filtering technique. The inverse transform was done over the range 1.53Å to 2.97Å. Figure 58 shows the derivative of the phase with different windows applied. If the dips shown in the range 3.14 to 3.41Å^{-1} were real the next order at about 9.8Å^{-1} would appear. It does not, and this is a

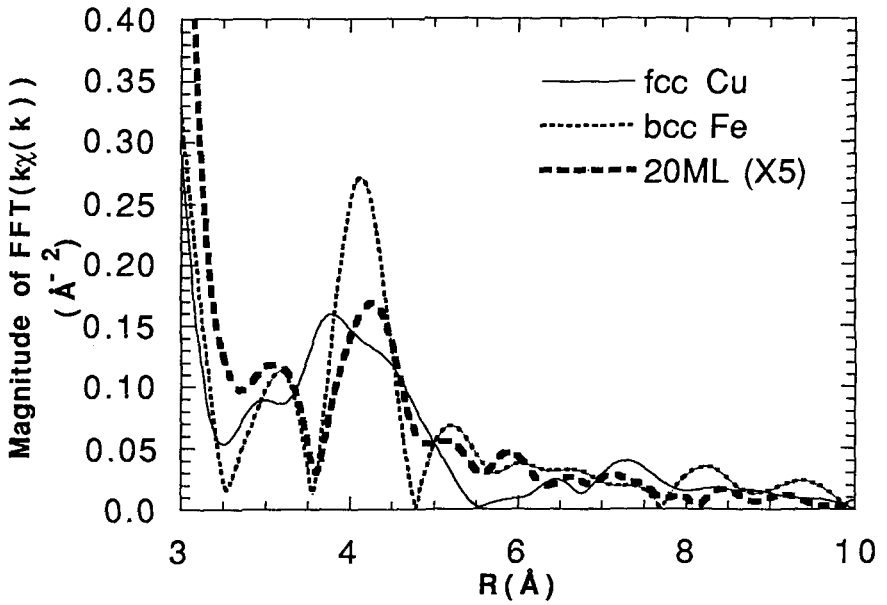

Figure 57: Comparing the structure of the higher shells. Fourier transform of $k\chi(k)$ for 20ML $\mathbf{E}_{\|}$, bcc Fe with a Hamming window applied over the range 2.4 to 13.13Å^{-1}. Here the 20ML data has been multiplied by a factor of 5.

position far enough away from the ends of the data which are known to contain artifacts that it can be concluded that the main peak is a single shell. The fact that this first peak is only one shell indicates a more fcc-like structure.

Since the outcome of the beating analysis is a single shell under the main peak the log-ratio method can be used to compare the 20ML data with the main peak of fcc Cu. The intercept is

$$\frac{N_1}{N_2}\frac{R_2^2}{R_1^2} = 1.58 \tag{90}$$

where the subscript 1 and 2 refer to fcc Cu and 20ML Cu respectively. Knowing that the nearest neighbor distance for fcc Cu is 2.5527Å and the number of nearest neighbor is 12 then $R_2^2/N_2 = .858$. From the slope $\Delta\sigma^2$ is .0004. These

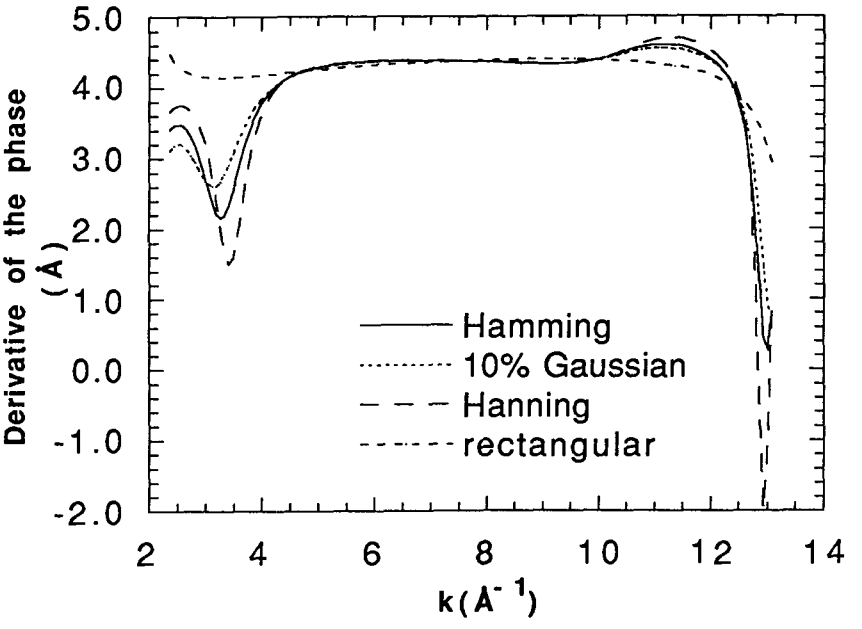

Figure 58: Beating Analysis on the 20ML Cu $\mathbf{E}_{\|}$ case.

R_1	$\Delta\sigma_1^2$	N_1
2.536	.00041	7.3
$\pm$.006	$^{+.0009}_{-.0008}$	$^{+.7}_{-.6}$

Table 14: Curve fitting result for 20ML with $\mathbf{E}_{\|}$ to the surface of the substrate. Fixed parameters were $a_1 = a_2 = 0$, $\Delta E_1 = \Delta E_2 = 0$.

results can be used to cross check the curve fitting results.

A multi parameter non linear least square fit was used to extract the structural parameters of the main peak. A one shell fit was done in R-space over the range 1.53–2.97Å. The tabulated results can be found in table 14. For this case, $\chi^2 = .91 \times 10^{-4}$. $\Delta\sigma^2$ is in excellent agreement with the log-ratio method and R^2/N ratio is .876 also in agreement with the previous result from the log-ratio method.

R_1	$\Delta\sigma_1^2$	N_1
2.533	-.00088	7.6
$\pm$.007	$^{+.0011}_{-.0009}$	$\pm$.8

Table 15: Curve fitting result for 20ML with $\mathbf{E}_\perp$ to the surface of the substrate. Fixed parameters were $a_1 = a_2 = 0$, $\Delta E_1 = \Delta E_2 = 0$.

The nearest neighbor distance is much closer to the nearest neighbor distance of fcc Cu (.7%) than to the nearest neighbor distance of bcc Fe (2%). Note that the coordination number is still approximately the value of a bcc structure which is also observed from the log-ratio method. In a fcc structure the coordination number is expected to be 12.

The Fourier transform of the data taken in the perpendicular configuration is very similar showing essentially a single peak with a reduced amplitude relative to the bcc Fe and the fcc Cu. Amplifying the higher orders gives a rather different picture. This is shown in figure 59 where both the fcc and bcc are overlayed on the data. The bcc-like nature is still evident but it is clear that some of the fcc-like features are gaining importance. For example the peaks at about 3.7Å^{-1} and 4.7Å^{-1} are not as well defined as in the parallel case.

Beating analysis showed the presence of only one shell under the main peak. The solution for a one shell non-linear least squares fit in R-space over the range 1.53-2.97Å is in table 15. The goodness of fit parameter, χ^2, was $.15\times10^{-3}$. The parameters are almost the same as in the parallel case. This fact suggests a cubic

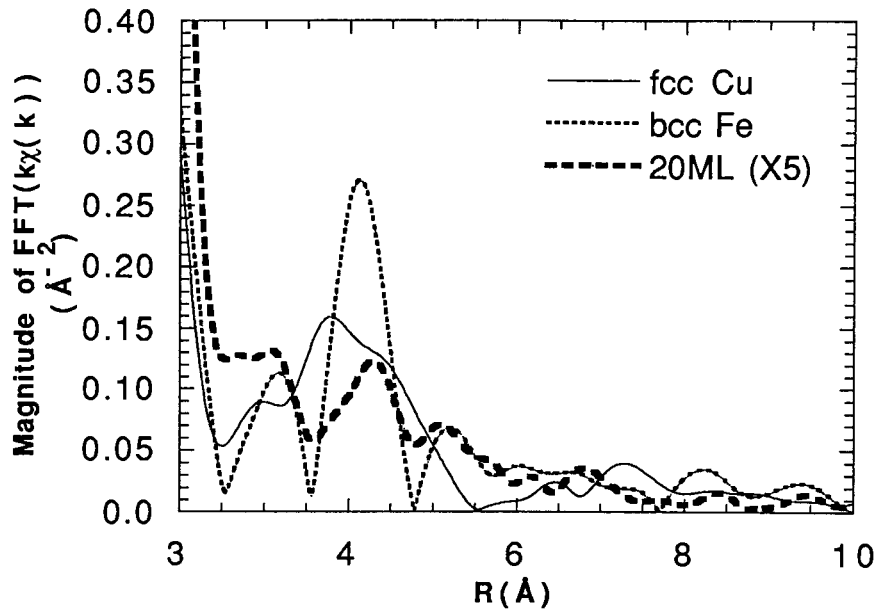

Figure 59: Comparing the structure of the higher shells. Fourier transform of $k\chi(k)$ for 20ML $\mathbf{E}_\perp$, fcc Cu and bcc Fe with a 10% Hamming window applied. Transform taken over the range 2.4 to 13.13Å^{-1}. Here the 20ML data has been multiplied by a factor of 5.

structure. Since the nearest neighbor distance is only .8% shorter than fcc Cu and 2% larger than bcc Fe then the local structure is more fcc-like in character. The coordination number and the Fourier transform of the higher shells may indicate the bcc-like structure imposed by the Fe underlayer still prevails even at 20ML. However, the detailed shape of the Fourier transform at large R depends sensitively on the multiple-scattering paths involved, so it is possible that the similarities with the bcc transform in the range 4Åto 5Å are misleading.

6.4 Conclusion

The sample with 8ML of Cu is bcc-like with a high disorder in the higher order shells. Taking the average of the $\mathbf{E}_{\|}$ and the $\mathbf{E}_{\perp}$ results, the in-plane lattice constant is 2.892±.02Å an increase of .8% from the lattice constant for Fe which is in good agreement with the RHEED results. The out-of-plane component is 2.864±.04Å a decrease of only .2% from the Fe value. The structure has a very slight distortion from a perfect cube. At a thickness of 20ML of Cu the lattice is cubic with an average nearest neighbor distance $R_1 = 2.535 \pm .005$Å. This is .7% smaller than the bulk Cu value. The coordination number is the same as for a bcc structure. The higher shells are almost non-existent indicating a large disorder beyond the nearest neighbor distance. 20ML is not sufficient for the Cu to regain its bulk features.

7 Concluding Remarks

The main goal for the work in this thesis was to use XAFS to determine the structure of two magnetic systems, $Tb_{.3}Dy_{.7}Fe_2$ and Fe/Cu/Fe trilayers.

The results of preliminary EXAFS experiments on Terfenol-D indicated that there was no change in the Fe-Fe distance but there was a trend in the Fe-Dy data suggesting a contraction of the Fe-Dy distance[93]. This prompted an extensive set of experiments whose results are presented in this thesis. As in the preliminary experiments the Fe-Fe distance does not change upon the application of a magnetic field. The contraction of the Fe-Dy distance is not observed in the later experiments. Therefore the Fe-Dy contraction previously observed may have been due to oxidation since covering the surface with a silicon nitride coating diminished the effect. In EXAFS investigations of single shell systems relative changes of distances have been determined to $\approx$ .003Å. In this work even using a conservative estimate such as $2\chi^2_{min}$ the errors obtained in a two shell fit are less than .009Å. The results obtained do not provide any insight into the double-tetrahedron model.

EXAFS analysis of the Fe/Cu/Fe trilayers shows a bcc structure with a slight expansion (.8%) of the in-plane lattice constant and only .2% contraction in the vertical direction with respect to the bcc Fe structure. It is also shown that as the growth proceeds the nearest neighbor distance increases until at a thickness

of 20ML it is only .7% smaller than the bulk fcc Cu value. This shows that as the thickness of the Cu layer increases the local Cu environment transforms from an initially bcc state towards the more natural fcc state for Cu. LEED studies on these trilayers grown on Fe whiskers claim the Cu remains in a bcc phase up to 20ML[62]. For thin samples, less than 10ML, LEED and RHEED confirm the almost unaltered bcc structure of the Cu[62]. For thicker films however, the RHEED patterns were the same as is observed in this thesis for the trilayers on Ag(001). The conclusion that the structure remains up to 20ML was reached by ignoring the RHEED evidence and emphasizing the observation that the LEED patterns showed no obvious change.

Another study[65] using EXAFS on Fe/Cu/Fe multilayers produced by sputtering, says that the Cu is in a bcc phase 1% larger than the Fe body centered cube up to about 13Å which is equivalent to ~9ML. For Cu thicknesses 24Å(~ 17ML) and higher the structure is characteristic of fcc Cu. In this last study the Cu is grown by sputtering where the growth is not as well controlled as in a MBE system. Therefore it is more disordered and the bcc metastable phase is lost at a smaller thickness than for the MBE grown samples.

Glancing-incidence EXAFS is a surface sensitive tool. In this work, excellent EXAFS data were obtained to probe both the in-plane and the perpendicular orientation for a buried interface. This is the state the Cu has during the mag-

netic studies. In situ techniques such as RHEED and LEED can only probe an uncovered surface. Glancing-incidence EXAFS provides additional information about the effect of the covering layers. Since all three techniques agree that the very thin films, less than 8ML, are bcc then the Fe covering layer does not have an effect for these thicknesses. This is not surprising since the Fe substrate, the thin film of Cu and the Fe covering layer all have the same bcc structure. For thicker films the final location of the Cu atoms after the top Fe layer is deposited may be different than the instantaneous picture of the layer during the process of the growth. The results in this thesis are then a description of the final structure of the system, on which magnetic properties are measured ex situ and from which subsequently devices can be made.

It was found in this work that locally the Cu is structurally disordered. This is an apparent contradiction to the RHEED results which show clear diffraction lines indicative of a crystalline structure with long range order. Any diffraction technique measures the average lattice constant over many unit cells. Any disorder would be observed in a reduction in the intensity of a diffraction line. In RHEED this is not monitored. EXAFS being a short range order probe is sensitive to the local disorder and the mean square relative displacement σ^2 which appears in the EXAFS Debye-Waller factor is a measure of this. The larger the σ^2 term the more disordered the structure which is what is observed

for these samples. The films have long range order but locally are structurally disordered. First principal calculations of the exchange coupling should take this into account.

At approximately 8ML thick these trilayers have been shown to change from a ferromagnetic coupling to an antiferromagnetic coupling. Considering the results of the present structural study just beyond the 8ML thickness corresponds to the start of the transition region from a bcc to an fcc structure. This is a similar situation as in Ni/Fe bilayers where the appearance of large in plane anisotropies with fourfold symmetry coincided with misfit dislocations created during the Ni lattice transformation[19],[64].

Appendix A: Magnetostriction equations

The one dimensional development of magnetostriction is generalized for the three dimensional case following the treatment given by Lee[54].

Magnetic anisotropy describes the circumstances that the energy of a system changes with a rotation of the magnetization. The anisotropy energy density in an unstrained crystal is (equation 2.1 in [54])

$$F_0 = K_0 + K_1(\alpha_1^2\alpha_2^2 + \alpha_2^2\alpha_3^2 + \alpha_3^2\alpha_1^2) + K_2\alpha_1^2\alpha_2^2\alpha_3^2 + ... \qquad \text{(A1)}$$

where K_1 and K_2 are the anisotropy constants at zero strain. The α's are the direction cosine of the magnetization with respect to the crystal axis.

As in magnetic anisotropy, magnetostriction originates in the interaction between the atomic magnetic moments. When the distance between atomic magnetic moments is variable the interaction energy is[93]

$$w(r, cos\phi) = g(r) + l(r)[\cos^2\phi - \frac{1}{3}] + q(r)[\cos^4\phi - \frac{6}{7}\cos^2\phi + \frac{3}{35}] + \cdots \qquad \text{(A2)}$$

where r is the interatomic distance, ϕ is the angle between the direction of magnetic moment and the bond direction, $g(r)$ is the exchange interaction term which is independent of the direction of magnetization. The second term is the dipole-dipole interaction term. It depends on the direction of magnetization and can be the main origin of the usual magnetostriction. The third term is a quadrupole term. $l(r)$ and $q(r)$ depend only on the interatomic distance. The

contribution of the higher order terms is usually small compared to those of this dipole-dipole interaction term.

Let $(\alpha_1, \alpha_2, \alpha_3)$ denote the direction cosines of domain magnetization and $(\gamma_1, \gamma_2, \gamma_3)$ those of the bond direction. Substituting in A2 and ignoring the exchange term

$$\begin{aligned} w &= l(r)[(\alpha_1\gamma_1 + \alpha_2\gamma_2 + \alpha_3\gamma_3)^2 - \frac{1}{3}] \\ &+ q(r)[(\alpha_1\gamma_1 + \alpha_2\gamma_2 + \alpha_3\gamma_3)^4 \\ &- \frac{6}{7}(\alpha_1\gamma_1 + \alpha_2\gamma_2 + \alpha_3\gamma_3)^2 + \frac{3}{35}] + \cdots \end{aligned} \tag{A3}$$

Now, consider a deformed simple cubic lattice whose strain tensor components are[94]

$$\begin{aligned} e_{xx} &= \frac{\partial u}{\partial x} \\ e_{yy} &= \frac{\partial v}{\partial y} \\ e_{zz} &= \frac{\partial w}{\partial z} \\ e_{xy} &= \frac{\partial v}{\partial x} + \frac{\partial u}{\partial y} \\ e_{zx} &= \frac{\partial u}{\partial z} + \frac{\partial w}{\partial x} \\ e_{yz} &= \frac{\partial w}{\partial y} + \frac{\partial v}{\partial z} \end{aligned} \tag{A4}$$

where u, v, w are the displacements in the x, y, z directions.

When the crystal is strained each pair of atoms changes its bond direction as well as its bond length and the free energy (equation A3) will depend on the strain. As was done in the one dimensional case, the magnetic part of the free energy is expanded in a Taylor series. In one dimension (see equation 36) the first term of this expansion is $\frac{F_1}{V_0} = Be$. In three dimensions the B's will be of the form

$$B_{11} = b_0 + b_1(\alpha_1^2 - \frac{1}{3}) + b_3 s + b_4(\alpha_1^4 + \frac{2}{3}s - \frac{1}{3}) + \cdots \quad \text{(A5)}$$

$$B_{12} = b_2\alpha_1\alpha_2 + b_5\alpha_1\alpha_2\alpha_3^2 + \cdots \quad \text{(A6)}$$

where

$$s = \alpha_1^2\alpha_2^2 + \alpha_2^2\alpha_3^2 + \alpha_3^2\alpha_1^2 \quad \text{(A7)}$$

The b_i's are measurable quantities called the magnetoelastic coupling constants.

Therefore the contribution made to the energy density by the strain, (sometimes called the strain energy) is given by (equation 2.3 in [54])

$$\begin{aligned} F_1 &= b_0[e_{11} + e_{22} + e_{33}] \quad \text{(A8)} \\ &+ b_1[(\alpha_1^2 - \tfrac{1}{3})e_{11} + (\alpha_2^2 - \tfrac{1}{3})e_{22} + (\alpha_3^2 - \tfrac{1}{3})e_{33}] \\ &+ b_2[\alpha_1\alpha_2(e_{12} + e_{21}) + \alpha_1\alpha_3(e_{13} + e_{31}) + \alpha_2\alpha_3(e_{23} + e_{32})] \\ &+ b_3 s[e_{11} + e_{22} + e_{33}] \\ &+ b_4[(\alpha_1^4 + \tfrac{2}{3}s - \tfrac{1}{3})e_{11} + (\alpha_2^4 + \tfrac{2}{3}s - \tfrac{1}{3})e_{22} + (\alpha_3^4 + \tfrac{2}{3}s - \tfrac{1}{3})e_{33}] \\ &+ b_5[\alpha_1\alpha_2\alpha_3^2(e_{12} + e_{21}) + \alpha_1\alpha_3\alpha_2^2(e_{13} + e_{31}) + \alpha_2\alpha_3\alpha_1^2(e_{23} + e_{32})] + \cdots \end{aligned}$$

Since the strain energy is a linear function with respect to the strain components the crystal will be deformed without limit unless it is counterbalanced by the elastic energy density which is for a cubic crystal (equation 2.3b in [54])

$$\begin{aligned} F_2 &= \frac{1}{2}c_{11}(e_{11}^2+e_{22}^2+e_{33}^2)+c_{12}(e_{11}e_{22}+e_{11}e_{33}+e_{22}e_{33}) \\ &+ \frac{c_{44}}{2}[(e_{12}+e_{21})^2+(e_{13}+e_{31})^2+(e_{23}+e_{32})^2] \end{aligned} \tag{A9}$$

where c_{ij}'s are the elastic stiffness constants. In one dimension F_2 was labelled as F_e (equation 37). Combining the above equations will give the energy which depends on the strain and on the crystallographic direction of the saturation magnetization vector.

$$F = F_0 + F_1 + F_2 \tag{A10}$$

For many purposes it is adequate to set $b_3 = b_4 = b_5 = 0$ and $K_2 = 0$ since these are small. With these approximations the free energy will be

$$\begin{aligned} F &= K_0 + K_1(\alpha_1^2\alpha_2^2+\alpha_2^2\alpha_3^2+\alpha_3^2\alpha_1^2) \\ &+ b_0(e_{11}+e_{22}+e_{33}) \\ &+ b_1[(\alpha_1^2-\frac{1}{3})e_{11}+(\alpha_2^2-\frac{1}{3})e_{22}+(\alpha_3^2-\frac{1}{3})e_{33}] \\ &+ b_2[\alpha_1\alpha_2(e_{12}+e_{21})+\alpha_1\alpha_3(e_{13}+e_{31})+\alpha_2\alpha_3(e_{23}+e_{32})] \\ &+ \frac{1}{2}c_{11}(e_{11}^2+e_{22}^2+e_{33}^2)+c_{12}(e_{11}e_{22}+e_{11}e_{33}+e_{22}e_{33}) \\ &+ \frac{c_{44}}{2}[(e_{12}+e_{21})^2+(e_{13}+e_{31})^2+(e_{23}+e_{32})^2] \end{aligned} \tag{A11}$$

The equivalent equation in one dimension is equation 38.

In a similar fashion when a stress is applied to the system, the total free energy density is $G = G_0 + G_1$. The zero stress term is (equation 2.4 in [54])

$$G_0 = K_0' + K_1'(\alpha_1^2\alpha_2^2 + \alpha_2^2\alpha_3^2 + \alpha_3^2\alpha_1^2) + K_2'\alpha_1^2\alpha_2^2\alpha_3^2 + ... \qquad \text{(A12)}$$

where K_1' and K_2' are the anisotropy constants at zero stress. The stress dependent term is (p.233 in [54])

$$\begin{aligned} G_1 &= -h_0[\sigma_{11} + \sigma_{22} + \sigma_{33}] \qquad \text{(A13)} \\ &- h_1[(\alpha_1^2 - \frac{1}{3})\sigma_{11} + (\alpha_2^2 - \frac{1}{3})\sigma_{22} + (\alpha_3^2 - \frac{1}{3})\sigma_{33}] \\ &- 2h_2[\alpha_1\alpha_2\sigma_{12} + \alpha_1\alpha_3\sigma_{13} + \alpha_2\alpha_3\sigma_{23}...] \end{aligned}$$

where σ_{ij}'s are the stresses. G_1 is written in terms of measurable quantities, h_i which are related to the A's and the B's as given through the equilibrium conditions.

The equilibrium condition when the external stress is zero is found from minimizing the total energy which is achieved by setting $\partial F/\partial e_{ij} = 0$. The result gives $e_{ik} = -B_{ij}s_{jk}$. This is the 3-d analog of equation 41 in the 1-d case. With an external stress present $\partial G/\partial\sigma_{ij} = 0$ will give $e_{ik} = A_{ik} + s_{ij}\sigma_{jk}$ (equation 43 in 1-d) and if $\sigma_{jk} = 0$ then $e_{ik} = A_{ik} = -B_{ij}s_{jk}$. Therefore, the spontaneous strains at zero stress in terms of B_{ij} are (equation 2.5 and 2.6 in

[54])

$$A_{ii} = -s_{11}B_{ii} - s_{12}(B_{ii} + B_{kk}), \quad i = j = k \tag{A14}$$

$$= h_0 + h_1(\alpha_i^2 - \frac{1}{3}) + h_3 s + h_4(\alpha_i^4 + \frac{2}{3}s - \frac{1}{3}) + ...$$

$$A_{ij} = -\frac{1}{2}s_{44}B_{ij}, \quad i \neq j \neq k \tag{A15}$$

$$= h_2\alpha_i\alpha_j + h_5\alpha_i\alpha_j\alpha_k^2 + ...$$

Therefore

$$h_0 = -b_0(s_{11} + 2s_{12}) \tag{A16}$$

$$h_1 = -b_1(s_{11} - s_{12}) \tag{A17}$$

$$h_2 = -\frac{1}{2}b_2 s_{44} \tag{A18}$$

$$h_3 = -b_3(s_{11} - s_{12}) \tag{A19}$$

$$h_4 = -b_4(s_{11} - s_{12}) \tag{A20}$$

$$h_5 = -\frac{1}{2}b_5 s_{44} \tag{A21}$$

Again, it is often an adequate approximation to set $h_3 = h_4 = h_5 = 0$ and $K_2' = 0$.

In terms of the measured quantities, if the direction in which the strain is observed is specified by the direction cosines β_1, β_2 and β_3 then in this direction the magnetostriction constants are defined as

$$\frac{\Delta l}{l} = \lambda_{\beta_j} = e(\alpha_i, \beta_j) = \sum_{i,j} A_{ij}\beta_i\beta_j \tag{A22}$$

Subtituting the A_{ij}'s in this equation gives

$$\begin{aligned} e(\alpha_i,\beta_j) &= h_0 + h_1(\alpha_1^2\beta_1^2 + \alpha_2^2\beta_2^2 + \alpha_3^2\beta_3^2 - \frac{1}{3}) \\ &+ 2h_2(\alpha_1\alpha_2\beta_1\beta_2 + \alpha_2\alpha_3\beta_2\beta_3 + \alpha_3\alpha_1\beta_3\beta_1) \\ &+ h_3 s \ldots\ldots\ldots\ldots\ldots\ldots\ldots\ldots\ldots\ldots (K_1 > 0) \\ &+ h_3(s - \frac{1}{3}) \ldots\ldots\ldots\ldots\ldots\ldots\ldots\ldots (K_1 < 0) \\ &+ h_4(\alpha_1^4\beta_1^2 + \alpha_2^4\beta_2^2 + \alpha_3^4\beta_3^2 + \frac{2}{3}s - \frac{1}{3}) \\ &+ 2h_5(\alpha_1\alpha_2\alpha_3^2\beta_1\beta_2 + \alpha_2\alpha_3\alpha_1^2\beta_2\beta_3 + \alpha_3\alpha_1\alpha_2^2\beta_3\beta_1) \end{aligned} \tag{A23}$$

Note that this is for cubic crystals only.

If the elongation is observed in the [100] direction and the magnetization is in the [100] direction then,

$$e(100,100) = \lambda_{100} = -\frac{2}{3}\frac{b_1}{(c_{11} - c_{12})} \tag{A24}$$

where the residual terms constant with respect to α and β are ignored. Similarly for the [111] direction,

$$e(111,111) = \lambda_{111} = -\frac{1}{3}\frac{b_2}{c_{44}} \tag{A25}$$

For polycrystalline materials the magnetostriction is calculated by averaging equation A22 over different crystal orientations by assuming $\alpha_i = \beta_i \quad (i = 1,2,3)$. This then gives

$$\lambda = \frac{2}{5}\lambda_{100} + \frac{3}{5}\lambda_{111} \tag{A26}$$

References

[1] S.A. Nikitin. Magnetostriction of Tb and Ho. *Soviet Physics-JETP*, 16(1):21–23, 1963.

[2] K.P. Belov, R.Z. Levitin, S.A. Nikitin, and A.V. Ped'ko. Magnetic and magnetoelastic properties of dysprosium and gadolinium. *Soviet Physics-JETP*, 13(6):1096–1101, 1961.

[3] F. Trombe. *Compt. Rend.*, 236:591, 1953.

[4] A.E. Clark and H.S. Belson. Giant room–temperature magnetostrictions in $TbFe_2$ and $DyFe_2$. *Phys. Rev. B*, 5(9):3642–3644, 1972.

[5] A.E. Clark. Magnetostrictive rare earth-Fe_2 compounds. In E.P. Wolfarth, editor, *Ferromagnetic Materials*, volume 1, pages 531–589. North Holland, 1980.

[6] K.B. Hathaway and A.E. Clark. Magnetostrictive materials. *MRS Bulletin*, XVIII(4):34–41, 1993.

[7] H.T. Savage, A.E. Clark, and J.M Powers. Magnetomechanical coupling and δE effect in highly magnetostrictive rare earth–Fe_2 compounds. *IEEE Trans. on Magnetics*, Mag–11(5):1355–1357, 1975.

[8] A.E. Clark, J.R. Cullen, and K. Sato. Magnetostriction of single crystal and polycrystal rare earth–Fe_2 compounds. *AIP Conference Proceedings*, 24:670–671, 1974.

[9] A.E. Clark. Magnetic and magnetoelastic properties of highly magnetostrictive rare earth–iron Laves phase compounds. *AIP Conf. Proc.*, 18:1015–1029, 1973.

[10] A.E. Clark and D.N. Crowder. High temperature magnetostriction of $TbFe_2$ and $Tb_{.27}Dy_{.73}Fe_2$. *IEEE Trans. on Magnetics*, 21(5):1945–1947, 1985.

[11] A.E. Clark, J.R. Cullen, O.D. McMasters, and E.R. Callen. Rhombohedral distortion in highly magnetostrictive Laves phase compounds. *AIP Conf. Proc.*, 29:192–193, 1975.

[12] J.R. Cullen and A.E. Clark. Magnetostriction and structural distortion in rare–earth intermetallics. *Phys. Rev. B*, 15(9):4510–4515, 1977.

[13] K.B. Hathaway and J.R. Cullen. Magnetoelastic waves in rare–earth intermetallics. *J. Appl. Phys.*, 49(3):1975–1977, 1978.

[14] M. Al-Jiboury and D.G. Lord. Study of the magnetostrictive distortion in single crystal Terfenol–D by x–ray diffraction. *IEEE Trans. Magn.*, 26(5):2583–2585, 1990.

[15] A.E. Dwight and C.W. Kimball. $TbFe_2$, a rhombohedral Laves phase. *Acta Cryst.*, B30:2791–2793, 1974.

[16] G.C. Hadjipanayis and G.A. Prinz, editors. *Science and Technology of Nanostructured Magnetic Materials.* Plenum Press, 1991.

[17] P. Grünberg, R. Schreiber, Y. Pang, M.B. Brodsky, and H. Sowers. Layered magnetic structures: Evidence for antiferromagnetic coupling of Fe layers across Cr interlayers. *Phys. Rev. Lett.*, 57(19):2442–2445, 1986.

[18] B. Heinrich, K.B. Urquhart, A.S. Arrott, J.F. Cochran, K. Myrtle, and S.T. Purcell. Ferromagnetic-resonance study of ultrathin bcc Fe(100) films grown epitaxially on fcc Ag(100) substrates. *Phys. Rev. Lett.*, 59(15):1756–1759, 1987.

[19] B. Heinrich, S.T. Purcell, J.R. Dutcher, K.B. Urquhart, J.F. Cochran, and A.S. Arrott. Structural and magnetic properties of ultrathin Ni/Fe bilayers grown epitaxially on Ag(001). *Phys. Rev. B*, 38(18):12879–12896, 1988.

[20] M.N. Baibich, J.M. Broto, A. Fert, F. Nguyen Van Dau, F. Petroff, P. Eitenne, G. Creuzet, A. Friederich, and J. Chazelas. Giant magnetoresistance of (001)Fe/(001)Cr magnetic superlattices. *Phys. Rev. Lett.*, 61(21):2472–2475, 1988.

[21] B. Heinrich, Z. Celinski, J.F. Cochran, W.B. Muir, J. Rudd, Q.M. Zhong, A.S. Arrott, K. Myrtle, and J. Kirschner. Ferromagnetic and antiferromagnetic exchange coupling in bcc epitaxial ultrathin Fe(001)/Cu(001)/Fe(001) trilayers. *Phys. Rev. Lett.*, 64(6):673–676, 1990.

[22] B. Heinrich, Z. Celinski, K. Myrtle, J.F. Cochran, M. Kowalewski, A.S. Arrott, and J. Kirschner. Magnetic properties of MBE structures using fcc Co/Cu(001) and bcc Fe/Cu(001). *J. Appl. Phys.*, 69(8):5217, 1991.

[23] Z. Celinski and B. Heinrich. Exchange coupling in Fe/Cu, Pd, Ag, Au/Fe trilayers. *J. Magn. Magn. Mater.*, 99(1–3):L25–L30, 1991.

[24] Y.U. Idzerda, B.T. Jonker, W.T. Elam, and G.A. Prinz. Structure determination of metastable cobalt films deposited on GaAs. *J. Vac. Sci. Technol. A*, 8(3):1572–1576, 1990.

[25] D.T. Jiang, E.D. Crozier, and B. Heinrich. Structure determination of metastable epitaxial Cu layers on Ag(001) by glancing–incidence x–ray–absorption fine structure. *Phys. Rev. B*, 44(12):6401–6409, 1991.

[26] S.T. Purcell, A.S. Arrott, and B. Heinrich. Reflection high-energy electron diffraction oscillations during growth of metallic overlayers on ideal and nonideal metallic substrates. *J. Vac. Sci. Technol. B*, 6(2):794–798, 1988.

[27] E. Bauer. Reflection electron diffraction (RED). In R.F. Bunshach, editor, *Techniques of Metals Research*, volume 2, pages 501–558. John Wiley & Sons, 1969.

[28] P.A. Montano, Y.C. Lee, J. Marcano, and H. Min. Electronic and crystallographic structure of iron films epitaxially grown on Cu single crystals. *MRS Symposia Proc.*, 56:183–188, 1986.

[29] Z.Q. Wang, Y.S. Li, F. Jona, and P.M. Marcus. Epitaxial growth of body-centered-cubic nickel on iron. *Solid State Commun.*, 61(10):623–626, 1987.

[30] M. Nielsen. Single crystal surface structure by Bragg scattering. *Z. Phys. B*, 61:415–420, 1985.

[31] I.K. Robinson. Direct determination of the Au(110) reconstructed surface by x-ray diffraction. *Phys. Rev. Lett.*, 50(15):1145–1148, 1983.

[32] I.K. Robinson. Surface structure by x-ray diffraction. In M.A. Van Hove and S.Y. Tong, editors, *The structure of surfaces*, pages 60–65. Springer-Verlag, 1984.

[33] J. Bohr, R. Feidenhans, M. Nielsen, M. Toney, R.L. Johnson, and I.K. Robinson. Model-independent structure determination of the InSb(111)2×2 surface with use of synchrotron x-ray diffraction. *Phys. Rev. Lett.*, 54(12):1275–1278, 1985.

[34] P.H. Fuoss, D.W. Kisker, G. Renaud, K.L. Tokuda, S. Brennan, and J.L. Kahn. Atomic nature of organometallic-vapor-phase-epitaxial growth. *Phys. Rev. Lett.*, 63(21):2389–2392, 1989.

[35] M. Sauvage-Simkin, R. Pinchaux, J. Massies, P. Claverie, J. Bonnet, and N. Jedrecy. Structure of in-situ grown GaAs(001) reconstructed surfaces by grazing incidence x-ray diffraction. *Surf. Sci.*, 211/212:39–47, 1989.

[36] S.M. Heald. Design of an EXAFS experiment. In D.C. Koningsberger and R. Prins, editors, *X-ray absorption: Principles, applications, techniques of EXAFS, SEXAFS and XANES*, chapter 3, pages 87–118. John Wiley & Sons, 1988.

[37] J. Stöhr. SEXAFS: Everything you always wanted to know about SEXAFS but were afraid to ask. In D.C. Koningsberger and R. Prins, editors, *X-ray absorption: Principles, applications, techniques of EXAFS, SEXAFS and XANES*, chapter 10, pages 443–571. John Wiley & Sons, 1988.

[38] E.A. Stern. Theory of EXAFS. In D.C. Koningsberger and R. Prins, editors, *X-ray absorption: Principles, applications, techniques of EXAFS, SEXAFS and XANES*, chapter 1, pages 3–51. John Wiley & Sons, 1988.

[39] G. Bunker, S. Hasnain, and D. Sayers. Report on the international workshops on standards and criteria in XAFS, 1990.

[40] J.J. Rehr and R.C. Albers. Scattering-matrix formulation of curved-wave multiple-scattering theory: Application to x-ray-absorption fine structure. *Phys. Rev. B*, 41(12):8139–8149, 1990.

[41] G. Bunker. Application of the ratio method of EXAFS analysis to disordered systems. *Nucl. Inst. and Met.*, 207:437–444, 1983.

[42] P.A. Lee and G. Beni. New method for the calculation of atomic phase shifts: application to extended x-ray absorption fine structure (EXAFS) in molecules and crystals. *Phys Rev. B*, 15(6):2862–2883, 1977.

[43] D.E. Sayers, E.A. Stern, and F.W. Lytle. New technique for investigating noncrystalline structures: Fourier analysis of the extended x-ray absorption fine structure. *Phys. Rev. Letters*, 27(18):1204–1207, 1971.

[44] F.J. Harris. On the use of windows for harmonic analysis with the discrete Fourier transform. *Proceedings of the IEEE*, 66(1):51, 1978.

[45] G. Martens, P. Rabe, N. Schwentner, and A. Werner. Extended x-ray-absorption fine-structure beats: A new method to determine differences in bond lengths. *Phys. Rev. Letters*, 39(22):1411–1414, 1977.

[46] N.W. Ashcroft and N.D. Mermin. *Solid State Physics.* W.B. Saunders Company, 1976.

[47] D.W. Marquardt. *J. Soc. Indust. Appl. Math.*, 11:431, 1963.

[48] K.R. Bauchspieβ. *A study of the pressure-induced Mixed-Valence transition in SmSe by X-ray absorption spectroscopy.* PhD thesis, Simon Fraser University, 1990.

[49] B. Lengeler and P. Eisenberger. Extended x-ray absorption fine structure analysis of interatomic distances, coordination numbers, and mean relative displacements in disordered alloys. *Phys. Rev. B*, 21(10):4507–4520, 1980.

[50] J.J. Rehr, J. Mustre de Leon, S.I. Zabinsky, and R.C. Albers. Theoretical x–ray absorption fine structure standards. *J. Am. Chem. Soc.*, 113(14):5135–5140, 1991.

[51] A.E. Clark, R. Abbundi, and W.R. Gilmor. Magnetization and magnetic anisotropy of $TbFe_2$, $DyFe_2$, $Tb_{0.27}Dy_{0.73}Fe_2$ and $TmFe_2$. *IEEE Transactions on Magnetics*, 14(5):542–544, 1978.

[52] B. Barbara, J.P. Giraud, J. Laforest, R. Lemaire, E. Siaud, and J. Schweizer. Spontaneous magnetoelastic distortion in some rare earth–iron Laves phases. *Physica B*, 86–88:155–157, 1977.

[53] R. Abbundi and A.E. Clark. Anomalous thermal expansion and magnetostriction of single crystal $Tb_{.27}Dy_{.73}Fe_2$. *IEEE Trans. on Magnetics*, 13(5):1519–1520, 1977.

[54] E.W. Lee. Magnetostriction. In G.M. Kalvius and R.S. Tebble, editors, *Experimental Magnetism*, pages 225–266. John Wiley & Sons, 1979.

[55] W.F. Brown Jr. *Magnetoelastic Interactions.* Springer, 1966.

[56] J.D. Verhoeven, E.D. Gibson, O.D. McMasters, and H.H. Baker. The growth of single crystal Terfenol–D crystals. *Metall. Trans. A*, 18:223–231, 1987.

[57] A. Erbil, G.S. Cargill III, R. Frahm, and R.F. Boehme. Total–electron–yield current measurements for near–surface extended x–ray absorption fine structure. *Phys. Rev. B*, 37(5):2450–2464, 1988.

[58] W.T. Elam, J.P. Kirkland, R.A. Neiser, and P.D. Wolf. Electron detection EXAFS in He and vacuum. *Physica B*, 158:295–298, 1989.

[59] D.T. Jiang and E.D. Crozier. A gas–flow electron yield detector for glancing–incidence EXAFS. *Nuclear Instr. and Methods in Phys. Res.*, A294:666–668, 1990.

[60] E. Sevillano, H. Meuth, and J.J. Rehr. Extended x–ray absorption fine structure Debye–Waller factors. I. Monotomic crystals. *Phys. Rev. B*, 20(12):4908–4911, 1979.

[61] C.E. Bouldin, E.A. Stern, B. von Roedern, and J. Azoulay. Structural study of hydrogenated a-Ge using extended x-ray absorption fine structure. *Phys. Rev. B*, 30(8):4462–4469, 1984.

[62] M.T. Johnson, S.T. Purcell, N.W.E. McGee, R. Coehoorn, J. ann de Stegge, and W. Hoving. Structural dependence of the oscillatory exchange interaction across Cu layers. *Phys. Rev. Lett.*, 68(17):2688–2691, 1992.

[63] B. Heinrich. Ferromagnetic resonance in ultrathin film structures. to appear in Ultrathin Magnetic Structures (Springer-Verlag), 1993.

[64] D.T. Jiang. *Structural investigations of metastable epitaxial metallic layers by glancing-incidence x-ray absorption fine structure.* PhD thesis, Simon Fraser University, 1991.

[65] S. Pizzini, F. Baudelet, D. Chandesris, A. Fontaine, H. Magnan, J.M. George, F. Petroff, A. Barthélemy, A. Fert, R. Loloee, and P.A. Schroeder. Structural characterization of Fe/Cu multilayers by x-ray absorption spectroscopy. *Phys. Rev. B*, 46(2):1253–1256, 1992.

[66] A.P. Payne, B.M. Lairson, S. Brennan, B.J. Daniels, N.M. Rensing, and B.M. Clemens. Epitaxial strain and the growth of Cu(001) on Fe(001). *Phys. Rev. B*, 47(23):16064–16067, 1993.

[67] F. Herman, M. van Schilfgaarde, and J. Sticht. Theories of long range oscillatory exchange coupling in magnetic multilayers. *Int. J. of Modern Physics B*, 7(1-3):425–433, 1993.

[68] J.J. Gilman. *The Art and Science of Crystal Growing.* John Wiley and Sons, 1963.

[69] E. Bauer. Phenomenological theory of crystal precipitation on surfaces. I. *Z. Krist.*, 110:372–394, 1958.

[70] I.F. Ferguson. *Auger Microprobe Analysis.* A. Hilger, 1989.

[71] L.E. Davis, N.C. McDonald, P.W. Palmberg, G.E. Riach, and R.E. Weber. Handbook of auger electron spectroscopy. Technical report, Physical Electronics, 1978.

[72] M.P. Seah and W.A. Dench. Quantitative electron spectroscopy of surfaces: a standard data base for electron inelastic mean free paths in solids. *Surf. Interface Anal.*, 1(1):2–11, 1979.

[73] P. Pukite. *Reflection high energy electron diffraction studies of interface formation.* PhD thesis, University of Minnesota, 1988.

[74] S.T. Purcell. *Structural and magnetic properties of ultrathin epitaxial nickel films grown on iron (001) surfaces.* PhD thesis, Simon Fraser University, 1989.

[75] C. Kittel. *Introduction to Solid State Physics.* John Wiley & Sons, 5^{th} edition, 1976.

[76] B.D. Cullity. *Elements of x-ray diffraction.* Addison-Wesley Publishing Company, Inc., 1978.

[77] J.M. Van Hove, P.R. Pukite, and P.I. Cohen. The dependence of RHEED oscillations on MBE growth parameters. *J. Vac. Sci. Technol.*, B3(2):563–567, 1985.

[78] R.L. Lyles, S.J. Rothman, and W. Jager. A cyanide-free solution for electropolishing silver. *Metallography*, 11(3):361–363, 1978.

[79] P.J. Schurer, Z. Celinski, and B. Heinrich. Mössbauer-effect investigation of the Fe(00)/Ag(001) interface. *Phys. Rev. B*, 48(4):2577–2581, 1993.

[80] J.D. Jackson. *Classical Electrodynamics.* John Wiley & Sons, 1975.

[81] L.G. Parratt. Surface studies of solids by total reflection of x-rays. *Physical Review*, 95(2):359–369, 1954.

[82] A.H. Compton. *X-rays in theory and experiment.* D.Van Nostrand Company, Inc., 1935.

[83] D.T. Cromer and D. Liberman. Relativistic calculation of anomalous scattering factors for x-rays. *The J. of Chem. Phys.*, 53(5):1891–1898, 1970.

[84] D.T. Jiang, N. Alberding, A.J. Seary, and E.D. Crozier. Angular scanning stage for glancing–incidence surface EXAFS. *Rev. Sci. Instrum.*, 59(1):60–63, 1988.

[85] B.A. Bunker, S.M. Heald, and J. Tranquada. EXAFS investigations of ion-implanted Si using fluorescence detection and a grazing-incidence x-ray beam. In K.O. Hodgson, B. Hedman, and J.E. Penner-Hahn, editors, *EXAFS and Near edge structure III*, pages 482–483. Springer-Verlag, 1984.

[86] D. Jiang, N. Alberding, A.J. Seary, and E.D. Crozier. A reflectivity and EXAFS study of layered structures. *Journal de Physique*, 47(12):C8–861–C8–864, 1986.

[87] P. Banddyopadhyay and B.A. Bunker. Reflection EXAFS studies of metal-semiconductor interfaces. *Physica B*, 158:653–654, 1989.

[88] H. Oyanagi, T. Fukui, T. Matsushita, T. Yao, T. Ishiguro, H. Saito, and K. Sugii. (InAs)1(GaAs)1 monolayers on InP(001) studied by x-ray absorption fine structure. *Physica B*, 158:694–695, 1989.

[89] C.E. Bouldin, R.A. Forman, and M.I. Bell. Conversion-electron extended x-ray-absorption fine-structure measurements of ion-damaged GaAs. *Phys. Rev. B*, 35(3):1429–1432, 1987.

[90] G. Brown and Z. Rek. Ssrl x-ray beamline documentation, 1981.

[91] J.P. Holman. *Experimental Methods for Engineers.* McGraw-Hill Book Company, 1971.

[92] Y.R. Bonin and E.D. Crozier. XAFS of $Tb_{.27}Dy_{.73}Fe_2$. *Jpn. J. Appl. Phys.*, Suppl.32-2:305–307, 1993.

[93] S. Chikazumi. *Physics of Magnetism.* John Wiley & Sons, 1964.

[94] C. Kittel. *Introduction to Solid State Physics.* John Wiley & Sons, 2^{nd} edition, 1953.